Chapter 5: Application of Machine Learning and Multi-Disciplinary/Multi-Objective Optimization Techniques for Conceptual Aircraft Design

Chapter details

Chapter DOI:

https://doi.org/10.4322/978-65-86503-71-5.c05

Chapter suggested citation / reference style:

Mattos, Bento S., et al. (2022). "Application of Machine Learning and Multi-Disciplinary/Multi-Objective Optimization Techniques for Conceptual Aircraft Design". *In* Jorge, Ariosto B., et al. (Eds.) *Model-Based and Signal-Based Inverse Methods*, Vol. I, UnB, Brasilia, DF, Brazil, pp. 143–236. Book series in Discrete Models, Inverse Methods, & Uncertainty Modeling in Structural Integrity.

P.S.: DOI may be included at the end of citation, for completeness.

Book details

Book: Model-based and Signal-Based Inverse Methods

Edited by: Jorge, Ariosto B., Anflor, Carla T. M., Gomes, Guilherme F., & Carneiro, Sergio H. S.

Volume I of Book Series in:

Discrete Models, Inverse Methods, & Uncertainty Modeling in Structural Integrity

Published by: UnB City: Brasilia, DF, Brazil Year: 2022

DOI: https://doi.org/10.4322/978-65-86503-71-5

Application of Machine Learning and Multi-Disciplinary/Multi-Objective Optimization Techniques for Conceptual Aircraft Design

Bento S. de Mattos[1 *], Felipe A. Bortolete[2], José A. T. G. Fregnani[3], Ariosto B. Jorge[4], William M. Alves[5], Ronaldo V. Cruz[6]

[1]Associate Professor, Instituto Tecnológico de Aeronáutica, bmattos@ita.br
[2]Ph.D. Candidate, Instituto Tecnológico de Aeronáutica, felipebortolete@gmail.com
[3]Visiting Professor, Instituto Tecnológico de Aeronáutica, fregnani@ita.br
[4]Post-Graduate Program - Integrity of Engineering Materials, University of Brasilia, Brazil. E-mail: ariosto.b.jorge@gmail.com
[5]Ph.D. Candidate, Instituto Tecnológico de Aeronáutica, wma.mecatronica@gmail.com
[6]Adjunct Professor, Instituto Tecnológico de Aeronáutica, ronaldoc@ita.br

*Corresponding author

Abstract

The development of fuel-efficiency airliners is crucial for the survival of aircraft manufacturers and airlines. In this context, multi-disciplinary optimization encompassing multiple objectives has provided great contributions to the aerospace industry. Thanks to the increase of computational power and efficient optimization algorithms, many tasks usually performed in the preliminary design phase are now carried out into the conceptual phase. Aeroelastic analysis and complex finite element models are already part of the conceptual phase. In addition, accurate and efficient surrogate models made faster and more stable computations possible. The content of this Chapter discusses the quest for the incorporation of high aspect wings into aircraft configurations, provides an overview of machine learning algorithms, and presents three engineering applications: two multi-objective optimizations of transport aircraft and a fluid-structure calculation of KC-135. The first optimization task is concerned with an aerodynamic optimization of an airliner wing by using a surrogate model to calculate aerodynamic coefficients based on artificial neural networks. The second optimization application encompasses the incorporation of flutter speed constraint for airliners of metallic construction into a multi-disciplinary optimization platform tailored for transport aircraft design. For this purpose, a package for structural sizing and aeroelastic analysis was integrated into the optimization framework developed at the Institute Technological of Aeronautics. This package is known as the Next-Generation Conceptual Aero-Structural Sizing (NeoCASS) from the University of Milano. NeoCASS is used to estimate the flutter speeds of individuals that arise during an optimization process. Finally, the detailed aircraft wing structure model of the KC-135 aerial refueller was built by using preliminary sizing procedures based on estimated main aerodynamic loadings, flight enveloped, V-n diagram, and detailed structural layout reports. Then a fluid-structure interaction (FSI) computer simulation procedure and compared to available experimental data.

Greek symbols

α	Angle of attack
Γ_{ϕ}	Diffusion coefficient
ϕ	Potential of velocities
Υ	Neuron activation function
κ	Thermal conductivity
μ	Dynamic viscosity
ρ	Fluid density
σ_{ij}	Stress tensor
θ	Neuron bias

Other Symbols and abbreviations

ADS-B	ADS-B stands for Automatic Dependent Surveillance Broadcast. ADS-B is a tracking system based merely on data transmission - in Mode-S (S stands for Select) - by the transponder at the frequency of 1090 MHz Broadcasted are several aircraft parameters
AF2	Approximate factorization (Scheme 2) introduced by Ballhaus and Steger [1]
ANN	Artificial neural network
AR	Aspect ratio
AR_w	Wing aspect ratio
BOW	Basic operating weight
BPR	Engine by-pass ratio
C_{DI}	Induced drag coefficient
CFD	Computational Fluid Dynamics
C_L	Lift coefficient
$C_{L.max}$	Maximum lift coefficient
C_p	Pressure coefficient
CSD	Computational structural dynamics
D	Drag force
DOC	Direct operating cost
DOE	Design of experiment
e	Oswald's factor (Related to induced drag)
e_{lweb}	The thickness of the front spar
e_{tweb}	The thickness of the rear spar
e_{upanel}	The thickness of upper skin
e_{lpanel}	The thickness of lower skin
$S_{Boom,i}$	Area of idealized boom
B_i	Area of real boom
EI and EI_{Liner}	Efficiency index of an aircraft configuration
FAR	Federal aviation regulation
F_d	Fuselage equivalent diameter
FEM	Finite element method

F_{hw}	Fuselage height-to-width ratio
FSI	Fluid-structure interaction
h_{lweb}	Height of front spar
h_{tweb}	Height of rear spar
L	Lift force
L/D	Lift-to-frag ratio
L_f	Fuselage length
LCO	Limit cycle oscillation
LRC	Long-range cruise
M	Number of Mach
M_d	Dive Mach number
M_∞	Freestream Mach number
MAC	Mean aerodynamic chord
MMO	Maximum operating Mach number
MTOW	Maximum takeoff weight
MZFW	Maximum zero-fuel weight
NeoCASS	Next-Generation Conceptual Aero-Structural Sizing
OPR	Engine overall pressure ratio
p	Pressure
PAX	Passenger/Passengers
RANS	Reynolds averaged Navier Stokes
Re	Reynolds number (The ratio between the viscous and inertia forces in a fluid)
R_{nm}	Range in nautical miles
RoC	Rate of climb
SMARTCAD	Simplified Models for Aeroelasticity in Conceptual Aircraft Design
S_w	Wing reference area
tc_root	The maximum relative thickness of the root wing station
TFL	Takeoff field length
TOGW	Take-off gross weight
TW	Thrust-to-weight ratio
V	Speed
VT	Vertical tail
VMO	Maximum operating calibrated speed
wbi	Width of the torsion box

1. The quest for high aspect-ratio wings and new aircraft configurations

1.1 Induced drag

Induced drag is drag linked to the generation of lift, which is a phenomenon that involves the production of vorticity at the trailing edge and wingtip of trapezoidal wings of transport aircraft (Delta wings presents other sources of vorticity). The vortex intensity generated at the trailing edge is directly proportional to the loading distribution (product of the chord in each section by the lift coefficient of the section) along the span. **Eq. 1** shows the basic formula for the calculation of induced drag coefficient:

$$C_{DI} = \frac{C_L^2}{\pi \cdot AR_w \cdot e} \tag{1}$$

Oswald's factor shown in **Eq. 1** is an efficiency parameter that measures how the loading distribution along the wingspan departs from a hypothetical elliptical one. Thus, shock waves, the lift itself and any other things that impact aerodynamics will also exert an influence on Oswald's factor. Niță and Scholz elaborated an empirical and low-fidelity model to calculate Oswald's factor with a satisfactory degree of accuracy [2]. The considerable increase of wing aspect ratio typically represents the pragmatic approach to reduce induced drag. However, this will bring some great disadvantages to the airplane configuration. Flutter is a primary cause of concern for design teams considering the adoption of high aspect-ratio wings. Usually, the design and optimization of an aeroelastic wing structure may be undertaken to minimize a structural mass that satisfies many different types of constraints.

The flutter boundary of an aeroelastic system is defined as the lowest airspeed at which a small perturbation to a static equilibrium leads to self-powered oscillatory motion that does not decay. Thus, it is defined as the lowest airspeed at which the system has a complex-conjugate pair of eigenvalues with zero real part. For linear systems, the dynamics predicted by flutter analysis apply globally and thus any perturbation at flutter speed leads to a divergent oscillation. The structural system is then dynamically unstable, and disturbances may catastrophically grow at an extremely low time [3].

Indeed, flutter ordinarily occurs due to a speed and lift coefficient combination. In this specific issue, there is an analogy with flight dynamics. The stability derivatives may be indicators of how a given aircraft will behave dynamically in a flight condition. However, after merely applying some commands from an initial condition it is then possible to analyze whether the trajectory will be stable or not. Similarly, the modal frequencies of an aircraft structure alone do not indicate dynamic behavior. The aircraft structure must be typically experiencing some loading to proceed cautiously with the comprehensive analysis of its flutter characteristics.

Nonlinear mechanisms within the aeroelastic system may attenuate the disturbance propagation and produce a self-sustained limit cycle oscillation [4]. For nonlinear structures, like that, merely represented by the Timoshenko beam model, the dynamics of the perturbation beyond the local region are unknown. Timoshenko's theory of beams constitutes an improvement over the Euler-Bernoulli theory, in that it incorporates shear and rotational inertia effects

As the deformation in the system becomes significant, changes in structural properties mean the modal interactions necessary for a flutter to inevitably take place may be naturally affected. In this manner, the dynamics are no longer topologically equivalent to that of a linear system [5].

At the flutter boundary itself, there are two distinct possibilities for a nonlinear system. The first comprises a flawless transition to a stable LCO when the critical airspeed is exceeded, the amplitude of which increases from zero for speeds higher than the flutter speed. In this case, the nonlinear flutter point coincides with a so-called supercritical Hopf bifurcation (**Figure 1**). This region is beneficial when compared to the linear case (**Figure 1**), as the unbounded oscillation is replaced by a reversible response via airspeed reduction (see arrows in **Figure 1**). Unfortunately, a harmful case is also part of the space of states: a subcritical Hopf bifurcation may occur, characterized by an unstable LCO region for speeds lower than the flutter one and a path turn featuring periodic oscillations, suddenly leading to a dangerous situation with large stresses and structural deflections [6]. Even decreasing the speed below the flutter point the system dynamics will not return immediately to the origin, resulting in a hysteresis loop [6].

The existence of subcritical behavior as described before leads to new considerations in aircraft optimization concerning posing flutter speed as a constraint for non-linear systems. Even considering the harmful situation that may occur in the subcritical region, below flutter speed, a gust, for example, can bring the system dynamics onto the stable large-amplitude limit cycle branch [6]. Naturally increasing wing aspect ratio leads to increased deflections when loading is present. However, the slenderness and reduced overall stiffness of wings optimized for minimal weight may lead to more complex deflections of more considerable magnitudes, resulting in nonlinear behavior. Such nonlinear effects can undoubtedly significantly influence the aeroelastic behavior of civil aircraft fitted properly with high aspect-ratio wings.

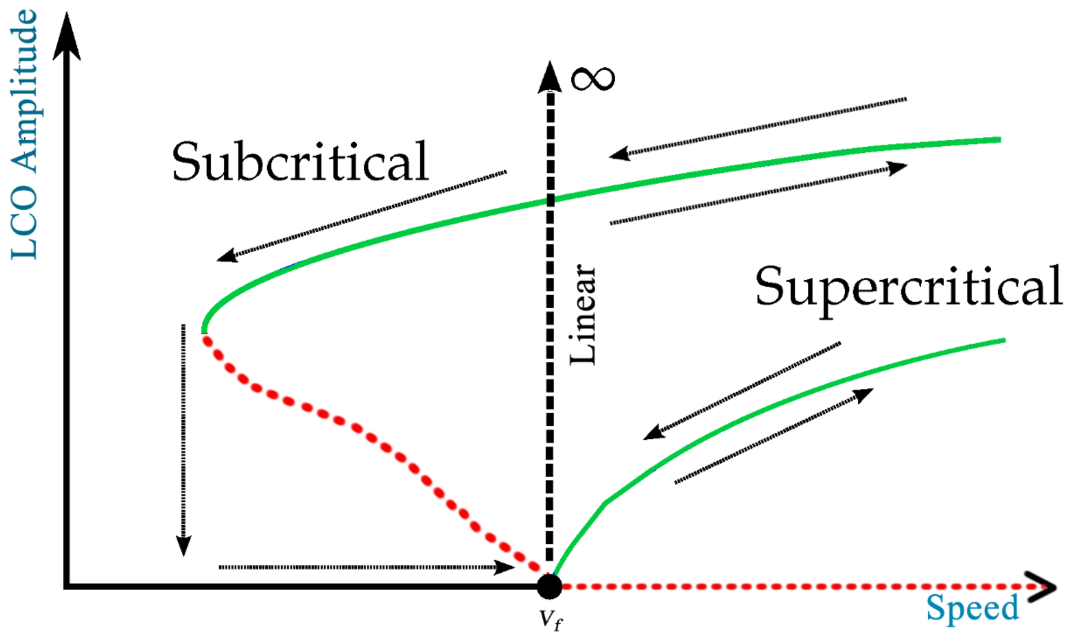

Figure 1: Generic flutter possibilities: linear, supercritical Hopf bifurcation, and subcritical Hopf situation; green color means stable behavior; red, unstable [5] [6]

The aerospace community has intensively been researching the efficient utilization of high aspect-ratio wings for commercial airplanes. Boeing developed its new 787 long-range airliner featuring extremely flexible wings in 2011, with All Nippon Airways as the launch customer [7]. Such highly flexible wings benefit from the stable LCO characteristics of nonlinear systems. Airbus chose a composite wing for the A350XWB airliner after a deep redesign of the initial proposition of an improved A330 [8]. The European Consortium adopted a figure of 9.49 for the A350-900 version [8]. The A350's wing features a quarter-chord sweep of 31.9 degrees, advanced shaped winglets, and spoilers that droop with flap extension to fully seal the gap between the Fowler flaps and wing to reduce drag [9]. Embraer developed a new variant of its E195 airliner and designated it E195E2, which features a considerable increase in wing aspect ratio when compared to previous products of that company. Both E195 and E195E2 feature wings of conventional wing aluminum structure. **Table 1** shows some compared characteristics of the original E195 to its variant E195E2 [10] [11] [12] [13] [14]. According to **Table 1**, a considerable BOW increase for the E2 version can be observed.

Table 1: Comparison of some characteristics of E195E1 and E2

	E-195E1 AR	**E-195E2**
Wing reference area [m^2]	92.50	103
Wing quarter-chord sweepback angle	23.5°	27.5°
Wing aspect ratio	8.1	9.4
Engine by-pass ratio	5.4:1	12:1
Single-engine dry weight [kg]	1,700	2,177
Max. passenger accommodation	124 @ 31" | 30" | 29" pitch	146 @ 28" pitch
Range (Full PAX, LRC)	2,300 nm (typical reserves)	2,655 nm (100 nm alternate)
MTOW/BOW [kg]	52,290/28,700	61,500/35,750
BOW/MTOW	0.55	0.58
Maximum usable fuel [kg]	13,100	13,500

The reduction of induced drag is the main reason behind the incorporation of high aspect ratio wings into transport aircraft configurations. Induced drag is dependent on the square of lift coefficient, aspect ratio, and the loading distribution along the wingspan. Despite its benefit due to the way it affects the induced drag, high-aspect-ratio wings bring with them several drawbacks:

- Flutter speed is reduced.
- Structural weight increases sharply [15].
- In combination with high-sweepback angles, they may lead to pitch-up behavior.
- The average chord is usually smaller, therefore, increasing the parasite drag.
- Potentialize the adverse yaw effect.

Transport airplanes with higher aspect ratio wings of metallic construction may require flutter ballast in front of the wing elastic line. Increasing the stiffness of the outer wing structure may not be enough to increase flutter speed. A concentrated mass of lead is typically used in such cases. The addition of winglets may require additional ballast due to pitch inertia increase at wingtips aggravating critical flutter modes [16]. For the Boeing 737-800 airliner, a reduction in the low altitude operating speed was avoided by adding 41 kg of ballast per wing in the outboard leading edge [16].

The necessity of incorporating a wing with a considerable aspect ratio into an aircraft will depend on the mission and other requirements of the project. Jet airplanes conceived for oceanic crossings will perform the cruising mission at optimal $M \times {}^{L}/_{D}$ value. This translates into a cruise Mach number lower than the MMO, resulting in a lift coefficient where the induced drag will be a considerable part of the overall drag. This may not be the case for regional airplanes, which perform the cruise phase is shorter when compared with long-haul airplanes. This type of airplane should be optimized for the airline network they will operate [17]. **Table 2** shows the average stage length flown in the United States of some major airlines [18].

Table 2: Average stage length in the U.S. flown by small narrow-body fleet [18]

	1995	1997	2000	2010	2016
American	852	898	850	860	762
Continental	731	822	903	1,003	-
Delta	552	569	609	745	665
Northwest	612	614	639	-	-
United	692	721	767	995	977
US Airways	514	521	554	779	-
America West	620	738	854	-	-
--sub Network	**664**	**699**	**727**	**835**	**766**

Due to the structural and aeroelastic reasons pointed out before, the strength and fatigue advantages of carbon fiber encouraged aircraft manufacturers to incorporate higher-aspect-ratio wings into airliner configurations. Besides the utilization of carbon fiber, unusual airplane configurations have been also proposed to mitigate the adverse effects of high-aspect-ratio wings (**Figure 2**). The unusual aircraft configurations being considered to address the induced-drag issue are summarized below:

- Twin-fuselage configuration
- truss-braced and strut-braced airliner
- highly flexible wings
- joined wings

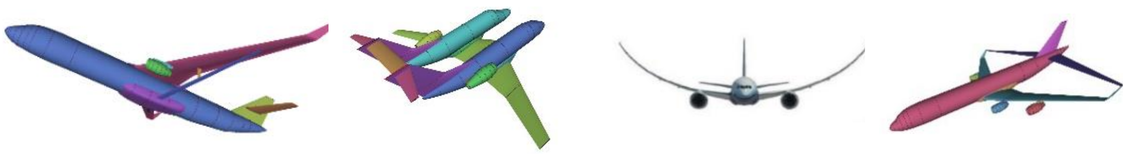

Figure 2: Some configurations usually proposed to mitigate drawbacks related to the adoption of high-aspect-ratio wings

1.2 Bracing

In aircraft design, bracing comprises a peculiar kind of structural component that stiffens the functional airframe to accrescent nominal rigidity and strength under loading. Structural reinforcements are applied both internally and externally and may take the form of the strut, which withstands compression or tension. Exposed wires, which resist tension, only, were commonly used to provide structural strength to vintage airplanes.

Strut-braced wing (SBW) and truss-braced wing (TBW) configurations provide a didactical example of drag reduction benefits that a radical change in wing configuration could bring. Such configurations are commonly seen on high-wing general aviation airplanes like the Cessna Skylane and Skyhawk and almost universal on parasol-winged airplanes such as the Consolidated PBY Catalina (**Figure 3**). Less commonly, some low-winged monoplanes like the Piper Pawnee agricultural airplane are characterized by lift struts mounted on the wing upper surface, acting in compression in flight and tension on the ground (**Figure 4**). For aircraft of moderate engine power and speed, lift struts represent a compromise between the higher drag of a fully cross-braced structure and the higher weight of a cantilevered wing.

Figure 3: PBY Catalina (Photo: B. Mattos)

Figure 4: Piper PA-25 Pawnee (Photo released to the public domain)

On a high-wing aircraft, a strut connects an outboard point on the wing with a point lower on the fuselage to form a rigid triangular structure. While in flight the strut acts in tension to carry wing lift to the fuselage and hold the wing level, while when back on the ground it acts in compression to hold the wing up. This kind of airplane has been studied by universities and aerospace manufacturers as a viable concept for medium-sized airliners. TBW offers potential for performance improvements in terms of fuel efficiency thanks to the higher aspect ratio wings it allows. Gern et al. claim that a strut-braced wing enables lower airfoil thickness, which will lower the transonic wave drag and hence require a lower wing sweepback angle [19]. In turn, they continue affirming that the lower wing sweep and high-aspect ratios will produce natural laminar flow thanks to low Reynolds numbers. Consequently, a significant increase in the overall aircraft performance is achieved. However, a lower airfoil thickness-to-chord ratio will inevitably lead to a heavier wingbox. The trade-off among several factors, lower wing sweepback angle, and the strut itself may bring a lighter airplane. In addition, there are also challenges for structural designers as the mitigation buckling of the strut or truss [20].

In 2000, Grossman et al. perform a comparative study for a 325-passenger class airliner fitted with two GE-90 engines [21]. The truss-braced airplane presents fuselage-mounted engines. Using contemporary multi-disciplinary design optimization techniques available at that time integration of the aerodynamic and structural design requirements was carried out. They considered a hexagonal wingbox and optimized area/thickness ratios for spar webs and caps, stringers, and skins. The results for the truss-braced configuration indicated that the take-off gross weight was reduced by more than 10-percent when compared to an equivalent cantilever wing airplane. According to Ref. [21], significantly larger weight reductions (19% TOGW) are obtained for the wing-mounted engine case.

To illustrate some characteristics of a strut-braced beam and compare it with a cantilever beam, the derivation of shear force and bending moments for beams was carried out and shown in the last part of this Section.

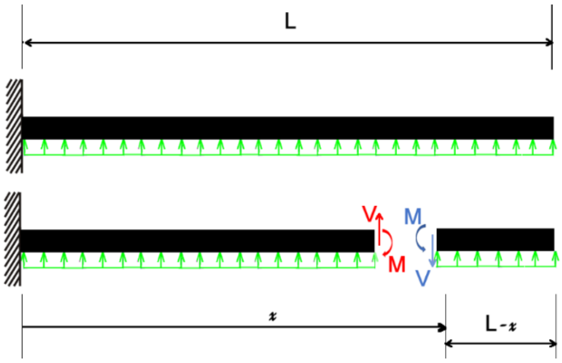

Figure 5: Internal reactions of a cantilever beam

Figure 5 shows a cantilever beam and the internal forces and moments at the boundary of two slices of it. *V* is the shear force; *M* is the bending moment and *w* is a uniform loading expressed in terms of force per unit length. The equilibrium of forces and moments promptly allows the derivation of two equations:

$$\sum F_y = 0 \tag{2}$$

$$\sum M_{x=L} = 0 \tag{3}$$

Inserting the right parameters in **Eqs. 2** and **3**, the following expressions for shear force and bending moment distributions can be derived:

$$w(L-x) - V = 0 \Longrightarrow V = w(L-x) \tag{4}$$

$$M + V * (L-x) - w(L-x)\frac{(L-x)}{2} = 0 \Longrightarrow M = -w\frac{(L-x)^2}{2} \tag{5}$$

Figure 6 shows the shear force and bending moment distributions from **Eqs. 4** and **5** for a 20-m-length beam and w = 5000 N/m. The shear force presents a linear variation with the horizontal distance from the wall and the bending moment a quadratic one.

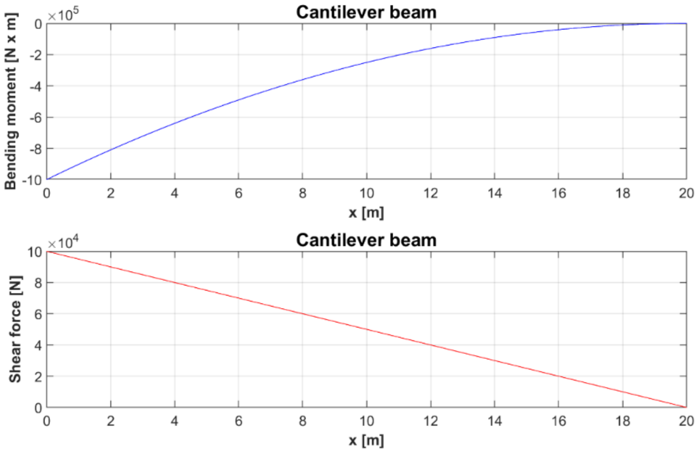

Figure 6: Shear force and bending moment along a cantilever beam

The same calculation procedure is now applied to obtain the distributions regarding a beam with a single strut, also subjected to a uniform lifting load. Assuming that the strut-wing junction is located at one-third of the overall beam length from the wall, the schematics of forces and moments for the whole beam are depicted in **Figure 7**.

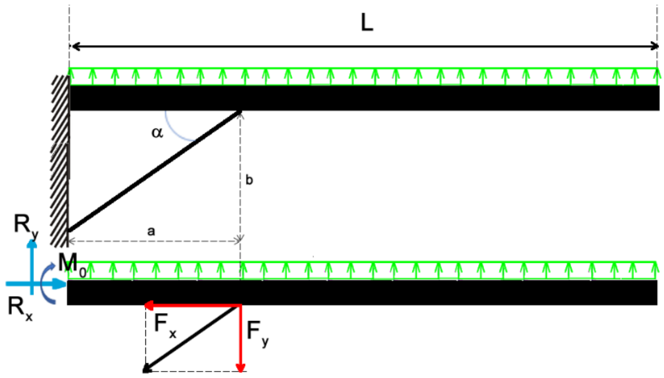

Figure 7: Schematics of reactions of a beam with a single strut

The balance equations for the whole beam for this case are as follows:

$$\sum F_x = 0 \Rightarrow R_x - F_x = 0 \Rightarrow R_x = F_x \tag{6}$$

$$\sum F_y = 0 \Rightarrow R_y - F_y + wL = 0 \tag{7}$$

$$\sum M_{x=0} = 0 \Rightarrow wL\frac{L}{2} - F_y a - M_0 = 0 \tag{8}$$

Considering that the reaction moment M_0 at the wall is zero, we obtain the vertical force acting on strut:

$$F_y = \frac{wL^2}{2a} \tag{9}$$

Now, F_x can be obtained:

$$F_x = \frac{F_y}{tg\alpha} = \frac{a}{b}F_y = \frac{wL^2}{2b} \Rightarrow R_x = \frac{wL^2}{2b} \tag{10}$$

For the obtention of shear force and bending moment distributions, it is necessary to make the force diagram of generic beam elements of the inner and outer beam (**Figure 8**).

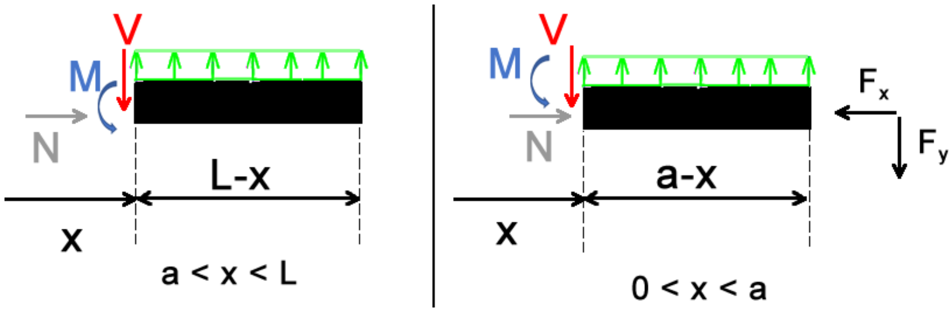

Figure 8: Force and moment schematics for two slices of the beam with strut

Considering the three balance equations for the outer beam, the shear force and bending moment distributions for this part can be easily obtained:

$$\sum F_x = 0 \Rightarrow N = 0 \tag{11}$$

$$\sum F_y = 0 \Rightarrow w(L-x) - V = 0 \Rightarrow V = w(L-x) \tag{12}$$

$$\sum M_{x=a} = 0 \Rightarrow M + w(L-x)\frac{(L-x)}{2} = 0 \Rightarrow M = -\frac{w}{2}(L-x)^2 \tag{13}$$

A straightforward calculation procedure is then carried out for the inner beam:

$$\sum N - F_x = 0 \Rightarrow N = F_x \text{ (compression)} \tag{14}$$

$$\begin{gathered}\sum F_y = 0 \Rightarrow w(L-x) - V - F_y = 0 \Rightarrow V = w(L-x) - F_y \\ \Rightarrow \qquad V = w(L - \frac{L^2}{2a} - x)\end{gathered} \tag{15}$$

$$\begin{gathered}\sum M_{x=0} = 0 \Rightarrow M + w(L-x)\frac{(L-x)}{2} - F_y(a-x) = 0 \\ \Rightarrow \qquad M = \frac{w}{a}\frac{L^2}{2}(a-x) - \frac{w}{2}(L-x)^2\end{gathered} \tag{16}$$

Figure 9 shows the shear force and bending moment distributions

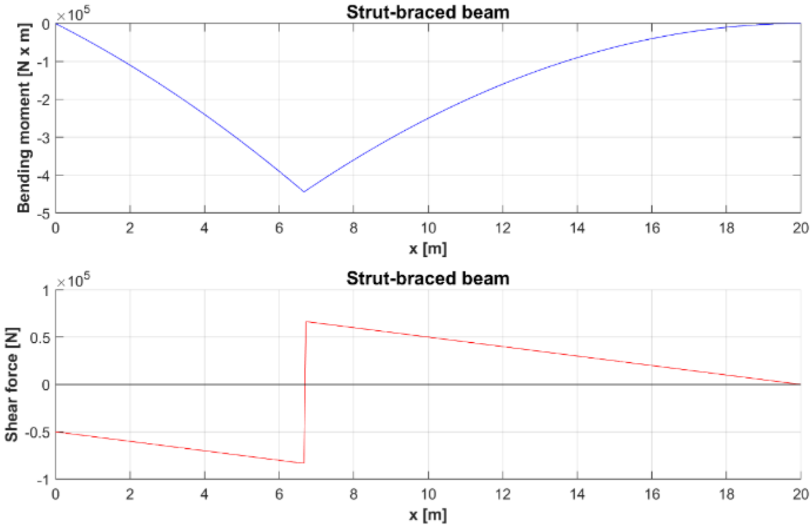

Figure 9: Shear force and bending moment along a strut-braced beam

An advantage of the beam with a strut is a reduction of the bending moment at the root station. However, the inner part of the beam becomes subject to compressive forces and therefore may suffer from buckling more prematurely.

1.3 Dual-fuselage aircraft

The main reason to consider a double-fuselage concept for airliners is the utilization of high aspect-ratio wings without aeroelastic penalties of an equivalent cantilever wing attached to a single fuselage. The stiffness of the resulting set is enough to provide higher flutter speeds.

Figure 10 shows Mach contours and **Figure 11** is a compound image of streamlines and contour surface that resulted from an Euler Simulation of a dual-fuselage configuration able to accommodate 34 passengers. Despite a relatively low freestream Mach number, many supersonic regions can be seen in the calculated flow over the configuration. A strong shock wave affects the wing between the fuselages, probably leading to flow separation at the Mach number of this simulation and higher. Indeed, the flow experiences a high acceleration in the region in between the two fuselages, behaving similarly as flow in a Venturi tube. Thus, the central wing must be carefully designed with additional considerations for a sound and aerodynamically clean design.

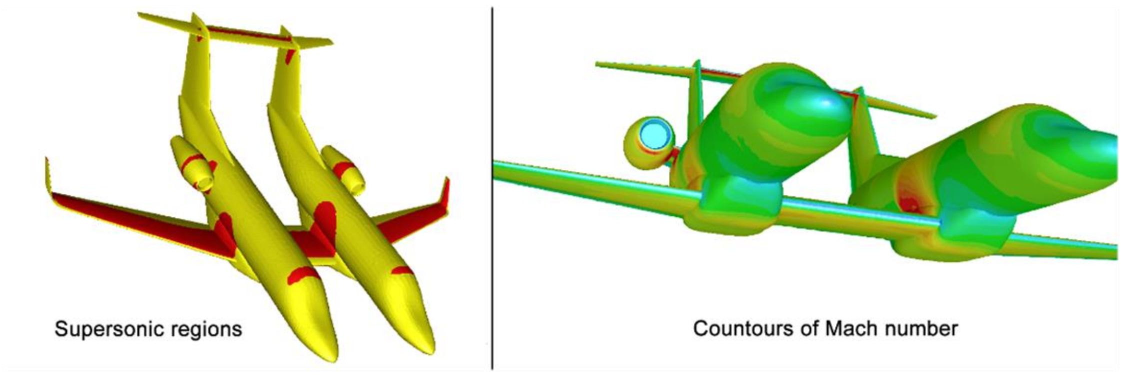

Figure 10: Euler calculation for a double-fuselage configuration (Mach = 0.76, α = 0º). At left: red regions indicate supersonic flow. At right: red color and yellow colors are associated with lower speeds; green color indicates that the local speed is close to the freestream Mach number

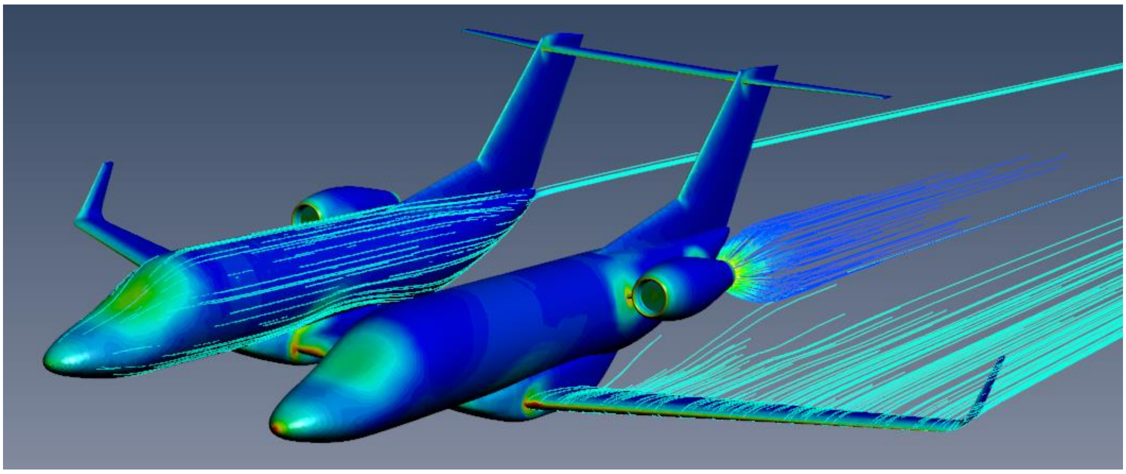

Figure 11: Streamlines over the dual-fuselage configuration (Mach = 0.76, α = 0°). Surface geometry is colored according to the calculated Mach number. Notice the rapid expansion of engine exhaust gases

To illustrate how important, it is in aircraft design to raise relevant topics that influence the manufacture, performance, and operation of the aircraft, here are some of the advantages of a dual fuselage aircraft and its disadvantages.

On the bright side:

- *Wing with a high aspect ratio is feasible*. The central wing will not have any wingtip (i.e., the wing starts and ends in the fuselage spanwise). The absence of a wingtip reduces the induced drag generated by the central wing. The overall wing could be of a higher aspect ratio contributing to the induced drag reduction. However, as shown before, the central wing must be carefully designed to prevent flow separation and high wave drag coefficients.
- Two smaller vertical tails can eventually save weight, depending on the design requirements and the mission of the aircraft. In addition, in a catastrophic event where one VT is damaged, the remained one may continue to be operated.
- A smaller fuselage will not require bigger production facilities and lighter support equipment around. Fuselage skin thickness is strongly dependent on the fuselage diameter; therefore, the fuselage weight grows exponentially to its diameter. However, are the loads in the flight envelope that will determine the structural sizing of the aircraft.
- *Cargo and passenger airplane*. Each fuselage could separately accommodate cargo and passengers facilitating handling and operation for this type of aircraft.
- *A dedicated fuselage for the business class passenger*. One of the fuselages could be configurated to accommodate business and/or first-class passengers only, allowing this way an exclusive service for them.
- It provides some advantages to specialized airplanes such as Scaled Composites VMS Eve (**Figure 12**). This aircraft is an example of a mother ship that carries a parasite aircraft between the two fuselages, releasing it later to perform a high-altitude flight or a sub-orbital spaceflight.

Some disadvantages of dual-fuselage configs are given as follows:

- Disturbances in airflow over the wing caused by the two fuselages may lead to higher interference drag and negatively impact the load distribution, which will contribute to an increase in the induced drag.
- *Larger rolling moments*: A dual-fuselage airplane will need larger rolling moments and hence, more effective ailerons.
- The central wing must keep the two fuselages together. So, the wing must take a bit of tensile/compressive loads. The forces separating the two fuselages are not the dominant forces, but still, something to keep in mind while designing. Also, the middle wing must maintain the two fuselages at the same pitch, so add a bit of twisting moments to the wing design, apart from aerodynamic twisting forces.
- *Roll stability*: In addition to the traditional parameters affecting the roll stability, i.e., the outer wing sweep and the outer wing dihedral, now there is a new parameter in the picture, the position of the two fuselages. I don't know if the twin-fuselage configuration has reduced or better roll stability, but either way, it complicates the things for achieving reasonable roll stability margins.
- A higher number of control surfaces is a challenge to the control system design. The by-wire system is a must for modern double-fuselage airliners.
- Ground operations will become more complex and difficult such as passenger boarding and deplaning, waste servicing, and catering.

In the past, some dual-fuselage configurations were developed **(Figure 13**). The Heinkel He 111Z was a combination of two existing He 111 tactical bombers. It was produced in a few units just to tug the huge transport glider Messerschmitt Me 321. To take advantage of the war surplus of P-51 Mustangs, a dual fuselage variant was developed for aerial reconnaissance missions (**Figure 13**).

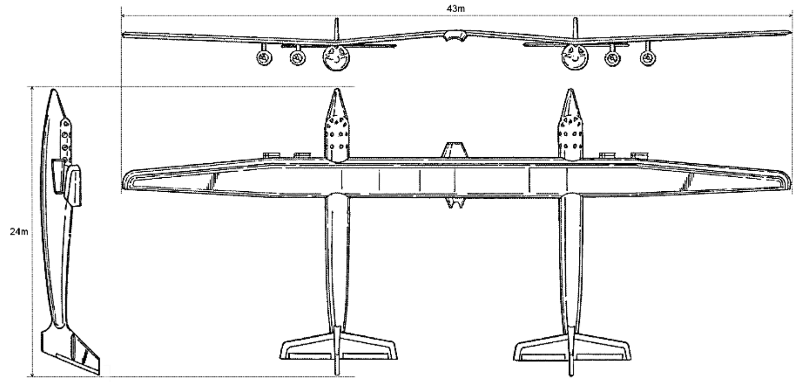

Figure 12: Scaled Composites VMS Eve (Drawing released to the public domain)

Figure 13: Dual-fuselage vintage aircraft. Left: Twin Mustang; Right: Heinkel He 111Z (Public domain photos)

2. A simple method to calculate wing structural weight

The primary structure of wings is represented by the torsion box or wingbox. An example of the structural layout of the torsion box of a wing is given in **Figure 14**. As can be seen in 1, the primary wing structure is something complex, and it is not possible to scale in a simple and fast way, the main objective of this work. For this, a simplified torsion box model is considered. Megson [22] elaborated a simplified wingbox model for its sizing, which was adopted for the calculation of the wing structural weight of some airliners (**Figure 15**). Stringers and spar flanges are replaced by concentrations of area, known as booms, over which the direct stress is constant, and which are located along the lines representing the skin. The content of this Section is an extended work of Videiro [23].

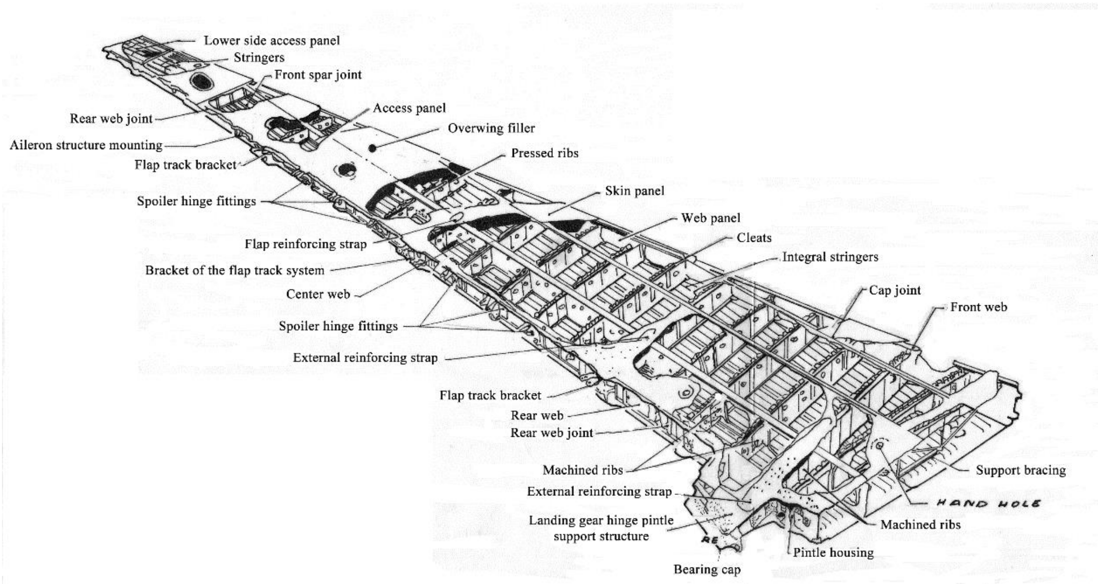

Figure 14: Illustration of a wingbox of a cantilever wing (Drawing from ITA's Aircraft Design Department)

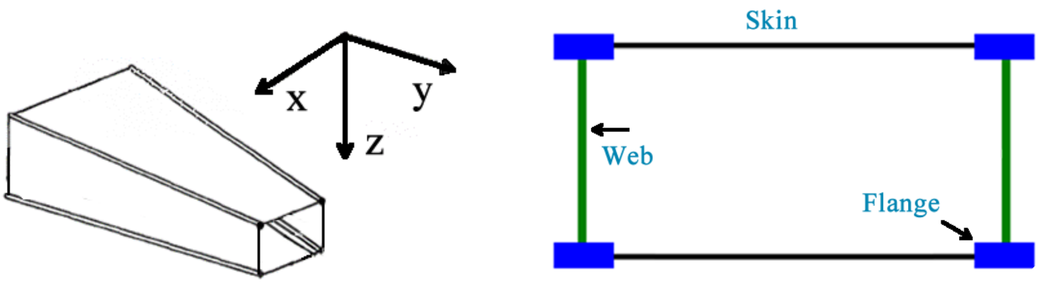

Figure 15: Simplified model of a wingbox

Calculating stations

Here are considered airplanes with a constant leading-edge sweep and a trailing edge with a single inflection, the latter called break station. Due to the wing structure complexity, the structural model is discretized into five distinct sections along the wingspan: wing root station, wing break station, and two sections beyond it (**Figure 16**). It is noteworthy that the number of stations can be changed by the user as well as their location.

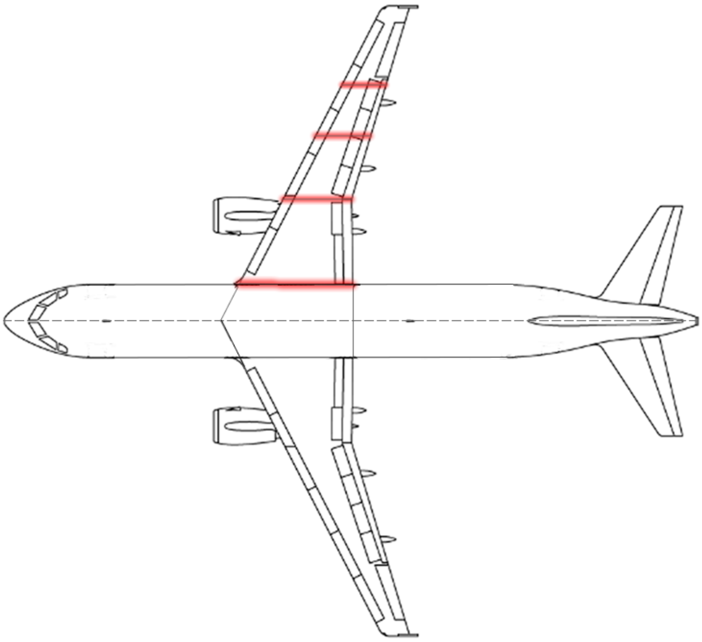

Figure 16: Calculating stations

External loading

Each section is sized individually. The loads are calculated by a wing-body full potential code and properly transferred to the sections. There are cases where the fuel weight is considered, and others are not. As the mission proceeds, some airplanes are continuously pumping fuel stored in the wings to a central tank in the fuselage to increase the fatigue life of the structure.

Another routine built the structural layout according to prescribed rib spacing and spar locations **(Figure 17**). The fuel storage capacities for the internal and external tanks are also calculated as well as the center of gravity of tanks considering them filled with fuel.

Figure 17: Example of wing layout for a 72-passenger airliner fitted with underwing **engines**

Internal stresses

The internal stress in each case is represented by the tensor of forces:

$$\tau = \{Rx, R_y, Rz, Mx, My, Mz\} \tag{17}$$

The reference system is indicated in **Figure 18**, and it has its origin in the geometric center of the section which due to the hypotheses of structural idealization that was adopted will coincide with the center of sharp stresses of the torsion box.

Figure 18: CEC Position (Cutting Stress Center)

Consequently, shear flows arise in the stringers and panel skins that need to be calculated for the very dimensioning of these components. Also, there will be axial forces, due to the actuation of bending moment, which, as already mentioned, are supported exclusively by the boons. Each section is treated as an isosceles trapezium to simplify structural calculations (**Figure 19**).

Figure 19: Approximation of the Wingbox Cross Section as an Isosceles Trapezium

The distance between the position of the geometric center of the trapezium and the front stringer is given by:

$$d_{CG} = \left(\frac{wbi}{3}\right)\frac{2h_{lweb} + h_{tweb}}{h_{lweb} + h_{tweb}} \tag{18}$$

Determination of the area of the idealized sections

For the center of mass to coincide with the geometric center of the section, the boom areas after idealization must be equal.

The moments of inertia of the section are given by:

$$I_{xx} = \frac{S_{Boom,i}h_{lweb}^2}{2} + \frac{S_{Boom,i}h_{tweb}^2}{2} \tag{19}$$

$$I_{zz} = \frac{S_{Boom,i}{d_{CG}}^2}{2} + \frac{S_{Boom,i}(wbi - d_{CG})^2}{2} \tag{20}$$

The axial stress at a generic point can then be expressed as:

$$\sigma(x,z) = \frac{M_x z}{I_{xx}} + \frac{M_z x}{I_{zz}} \tag{21}$$

According to **Eq. 21**, it is possible to deduce which of the four booms will present the highest axial stress and will consequently be the most critical for sizing. Considering that the rupture stress of material that constitutes the wing is known. the *critical* boom can be dimensioned. In this step, the idealized area of the boom and not its real area is employed. At the end of the sizing procedure is when the thicknesses of the stringers and the skin will be known.

Shear flow

Figure 20 shows an example of shear force due to aerodynamic loading for a load factor, *n*, equal to 1.

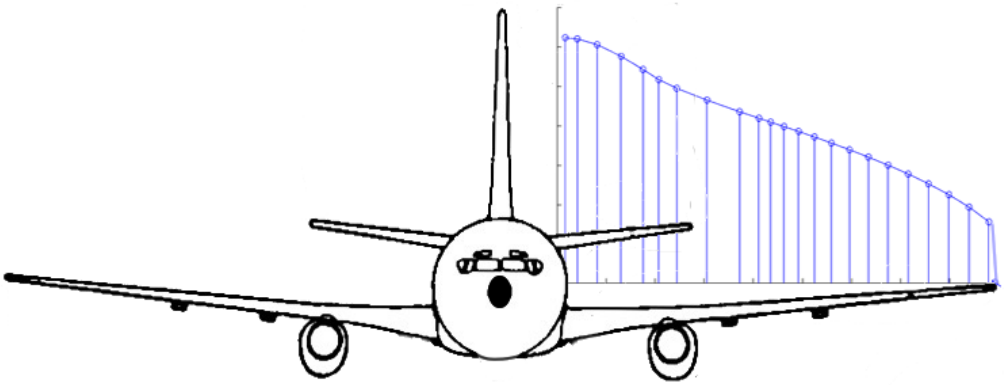

Figure 20: Example of shear force distribution along semispan of jet transport aircraft ((M∞ = 0.80, C_L=0.48, *n*=1)

To find the values of the shear flow of a closed section, the method presented by Megson [22]. The shear flow is divided into two parts:

$$q = q_B + q_{s,O} \tag{22}$$

In **Eq. 22**, q_B is the flow calculated after making a "cut" on one of the walls of the closed section. This flow varies depending on the path around the perimeter of the section:

$$\begin{aligned} q_B = &-\left(\frac{S_x I_{xx} - S_y I_{xy}}{I_{xx} I_{yy} - I_{xy}^2}\right)\left(\int_0^s t_D x ds + \sum_r^n S_{Boom,i} x_r\right) \\ &- \left(\frac{S_y I_{yy} - S_x I_{xy}}{I_{xx} I_{yy} - I_{xy}^2}\right)\left(\int_0^s t_D y ds + \sum_r^n S_{Boom,i} y_r\right) \end{aligned} \tag{23}$$

As the section is symmetrical concerning the axis x => $I_{xy} = 0$. Besides, the idealization assumes that the thickness is null, $t_D = 0$, so that the expression of **Eq. 23** can be simplified:

$$q_B = -\frac{S_x}{I_{yy}} \sum_r^n S_{Boom,i} x_r - \frac{S_y}{I_{xx}} \sum_r^n S_{Boom,i} y_r \tag{24}$$

Eq. 24 indicates that the shear flow is constant on the same wall and any variation is caused solely due to the presence of a boom. The contribution of $q_{s,O}$ is constant on all walls of the closed section. Its function is to equalize the torque produced by the external forces with the internal torque that will arise due to the internal shear flow. Therefore, knowing the external forces and the idealized area of the booms, shear flows can be determined and consequently size the thickness of the stringers and skin.

Shear stress is given by the division between shear flow and material thickness. Thus, smaller thicknesses result in higher shear stresses.

$$\tau = \frac{q}{e} \Rightarrow e = \frac{q}{\tau_{MAX}} \tag{25}$$

The last step of structural sizing is to revert the idealization of the structure to obtain the actual areas of the booms:

$$B_1 = S_{Boom,i} - \frac{e_{lweb} h_{lweb}}{6} - \frac{e_{upanel} wbi}{2} \tag{26}$$

$$B_2 = S_{Boom,i} - \frac{e_{tweb} h_{tweb}}{6} - \frac{e_{upanel} wbi}{2} \tag{27}$$

$$B_3 = S_{Boom,i} - \frac{e_{tweb} h_{tweb}}{6} - \frac{e_{lpanel} wbi}{2} \tag{28}$$

$$B_4 = S_{Boom,i} - \frac{e_{lweb} h_{lweb}}{6} - \frac{e_{lpanel} wbi}{2} \tag{29}$$

Rib sizing

Contrary to what was performed for the sizing of the coating, stringer, and booms, a statistical and historical approximation is used to determine the mass of the ribs. This is due to failed attempts to scale this component, whose main structural function is to resist buckling to ensure the shape of the ass when loaded.

Another difficulty presented was the fact that the ribs of the aircraft presented holes for the passage of hydraulic components and weight alleviation, for example, or to form the fuel tank inside the wings.

The solution adopted was to use an area density for the ribs, $\rho_{Nerv} = 9.6 kg/m^2$. The average spacing between the ribs on a passenger transport aircraft is 0,70 m. Thanks to the planform known data and the location of the rear and front spars, and other data a routine was built to define the structural layout and therefore all positioning and some dimensions of ribs in the wing. The mass of all ribs is given as:

$$M_{Nerv} = \rho_{Nerv} S_{Nerv} \tag{30}$$

Where is the sum of the areas of all cross-section sum of the areas of the cross-section where the ribs are located, S_{Nerv}.

Model for the secondary structure

In the previous chapter, a model for calculating the mass of the primary structure of the wing was elaborated. Now, it remains to do the same procedure for the secondary structure (flaps, spoilers, hydraulic systems, etc.) to obtain a complete model of the wing of an aircraft. However, due to the complexity of scaling the devices of the secondary structure, a statistical approach is used to estimate the mass.

The difficulty comes, among other factors, from the wide variety of types of hyper-support devices that an aircraft can have:

In addition, the sizing of systems such as hydraulics is a complex task, with a level of difficulty that escapes the objectives of this work and that are not compatible during the conceptual design stage of the aircraft.

Historically, the mass of the secondary structure contributes with 20-30% mass of wings. This enables a very simple first mass estimation:

$$M_{Wss} = 0.26 M_W \tag{31}$$

Torenbeek [24] proposed a method to estimate the mass of the secondary structure with more accuracy. This method requires that the area of high-lift devices be known. However, due to unsatisfactory results when compared to the actual mass of existing aircraft wings, its use was then not here considered [25]. The more accurate formula proposed by Roux [25] is to assume that the mass of the secondary structure is proportional to the power of the wing area.

$$M_W = K\, S^n \tag{32}$$

Being the factors and adjusted from historical values, minimizing the quadratic error between the model and the actual mass. $K = 25.9$ and $n = 0.97$ for airplanes with MTOW higher than 20 t.

Once the tensor of stresses is constructed, the design of the primary structure of the wings can be started. The sizing of the primary structure can be divided into two cases:

- Sizing of *continuous* structures along with the aircraft's wings, such as stringer, skin, and reinforcers. The structural module must be written in a routine that from the geometry of the wings and the force tensioner returns the area of each section to be sized.
- For the sizing of the *discontinuous* structures along the aircraft wing, more specifically the ribs, the same subroutine must provide the total volume of this structure throughout the whole wing.

Two test cases were run with aircraft like B737-200 and A320-200 (**Tables 3** and **4**). Since airfoil geometry and other relevant information are unknown; airfoils presenting the same maximum relative thickness as those of the real airplanes were utilized, instead. Overall wing mass estimated using the Torenbeek method [24] is also provided. The MZFW that is required by the Torenbeek approach was furnished based on the fuel capacity calculated by the present methodology considering that fuel is stored only on the wings.

Table 3: Airplanes selected to test the methodology

	Similar to Boeing 737-200	Similar to A320-200
Seating abreast in the Y-class	6	6
Single class passenger capacity (32-in pitch)	132	180
Wing aspect ratio	8.83	9.38
Wing taper ratio	0.266	0.240
Wing area [m^2]	91.04	122.4
Location of the front/rear spar	23/64% chord	23/64% chord
Rib spacing (in)	22	22
tc_root	15.4% at 19.6% chord	15.13%
MMO	0.82	0.82

Table 4: Mass estimation compared with actual on

	Similar to Boeing 737-200	Similar to A320-200
Estimated wing mass (primary/secondary/total)	3432/2060/5492	5950/2744/8694
Mass according to Torenbeek [24]	5346 kg	8285 kg
Actual overall wing mass [25]	5038 kg	8766 kg

3. A fluid-structure simulation for capturing elastic effects on wing structure

The objective of this Section is to highlight the importance of considering aeroelastic effects on the aircraft conceptual design. For this purpose, aeroelastic effects observed in a military jet airplane were computed by a fluid-structure interaction (FSI) computer simulation procedure and compared to available experimental data. The effects of elastic characteristics of the configuration on pressure coefficient distribution were deeply investigated. The detailed aircraft wing structure of the KC-135 aerial refueller was built by using preliminary sizing procedures based on estimated main aerodynamic loadings, flight enveloped, V-n diagram, and detailed structural layout reports. The simulation results are in excellent agreement compared with wind tunnel and flight-test data.

3.1 Fluid-structure interaction models

The modeling of fluid-structure interaction can be classified under three major branches, following the coupling strategy: fully coupled, loosely coupled, and closely coupled analyses.

The fully coupled approach combines structural equations of motion and fluid dynamics equations in integral form and solves the related time-discretized equations. However, such a procedure requires constructions that produce matrices with different orders of magnitude for solids and fluids because they are written for different modeling reference frames (**Figure 21**). This hinders the discretization of the problem, limiting the construction of the grids and being expensive from the computational point of view, usually being used in two-dimensional problems [26].

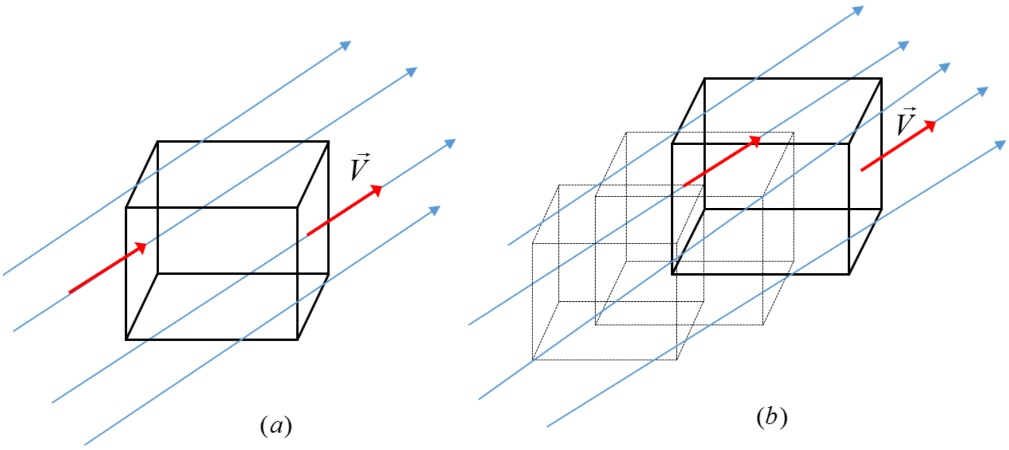

(a) Eulerian control volume

(b) Lagrangian control volume moving and deforming with fluid flow

Figure 21: Reference frames

Loosely coupled approaches [27], unlike fully coupled strategy, structural dynamics and fluid dynamics are solved using separated solvers and have different computational grid topologies in which boundaries are non-coincident. An external connection between fluid and structure modules is made. The fluid solver, in general, has reasonable techniques to export forces to the interface with the structure solver.

The closed approach is one of the most widely used methods in the field of computational aeroelasticity. Fluid models and structures are solved in different solvers. However, it has an internal connection module that exchanges information between the two models, which intercommunicate iteratively (**Figure 22**).

The information exchanged are the surface loads, mapped on the CFD surface grid and transmitted to the structural dynamics (CSD) grid, which maps the displacement field, transferring this information to the CFD solver [28].

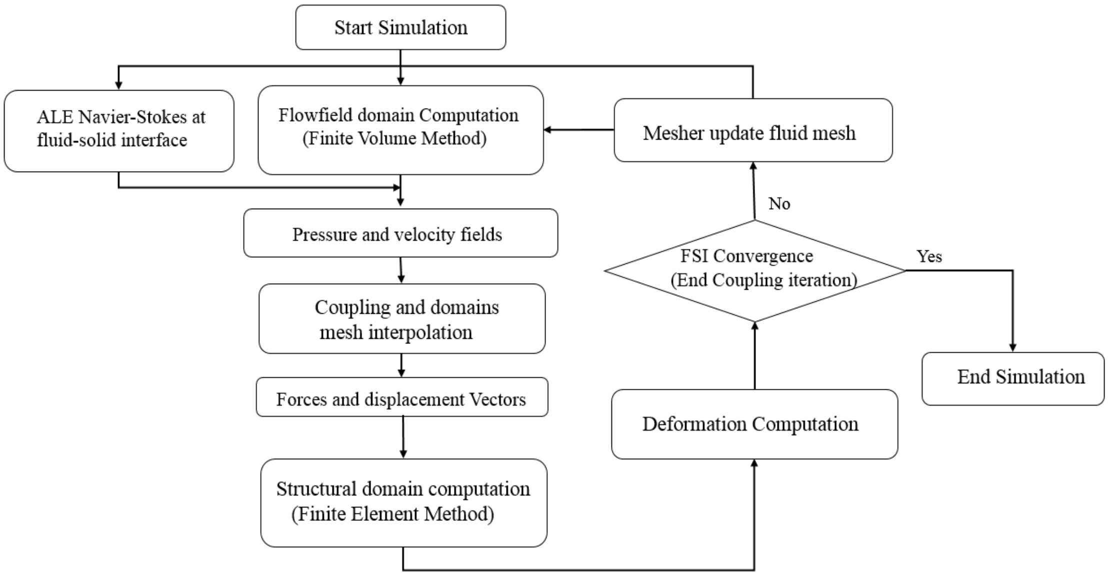

Figure 22: Fluid-structure coupling procedures

3.2 Fluid Flow Dynamics Fundamental Equations

In this section, an overview of the fluid dynamics equations for an Eulerian reference frame is given.

The fluid model assumes a linear relationship between viscous stress and strain:

$$\sigma_{ij} = \mu\left(\frac{\partial v_i}{\partial x_j} + \frac{\partial v_j}{\partial x_i} - \frac{2}{3}\frac{\partial v_k}{\partial x_k}\delta_{ij}\right) - p\delta_{ij} \tag{33}$$

The laws of conservation of mass, motion, and energy may be written as:

$$\frac{\partial \rho}{\partial t} + \frac{\partial(\rho v_i)}{\partial x_i} = 0 \tag{34}$$

$$\frac{\partial(\rho v_i)}{\partial x_i} + \frac{\partial(\rho v_i v_j)}{\partial x_j} = \frac{\partial}{\partial x_j}\left[\mu\left(\frac{\partial v_i}{\partial x_j} + \frac{\partial v_j}{\partial x_i} - \frac{2}{3}\frac{\partial v_k}{\partial x_k}\delta_{ij}\right)\right] - \frac{\partial p}{\partial x_i} + \rho f_i \tag{35}$$

$$\frac{\partial(\rho e)}{\partial t} + \frac{\partial(\rho v_i e)}{\partial x_i} = \mu\left[\frac{\partial v_i}{\partial x_j}\left(\frac{\partial v_i}{\partial x_j} + \frac{\partial v_j}{\partial x_i}\right) - \frac{2}{3}\left(\frac{\partial v_i}{\partial x_i}\right)^2\right] - p\frac{\partial v_i}{\partial x_i} + \frac{\partial}{\partial x_i}\left(\kappa\frac{\partial v_i}{\partial x_i}\right) + \rho q \tag{36}$$

where ρ is the density of the fluid, f_i are the external forces, and q represents heat sources.

The realizable $\kappa - \epsilon$ turbulence model is well known, and it was employed in the computations of the present Section. Enhanced wall treatment was also chosen, where the entire domain is subdivided into a viscous-affected near-wall region and a fully turbulent region determined by a wall-based turbulent Reynolds number and interpolated by enhanced wall functions that approximate expected boundary layer behavior and the region between viscous-affected and fully turbulent is represented by a blending function.

A finite volume method was used to solve numerically partial differential equations of fluid flow. It consists of the approximation of integral by applying Gauss's divergence theorem. Finite volume methods integrate the partial differential equations over each control volume to find discretized equations to each control volume, conserving physical quantities (e.g., mass, heat transfer) to each control volume.

This method is applied over a conservation equation reformulated into the general form, called as general transport equation [29], written in its differential form:

$$\frac{\partial \rho\phi}{\partial t} + div(\rho\phi u) = div(\Gamma_{\phi}\nabla\phi) + S^{\phi} \tag{37}$$

Eq. 38 was written in divergence form to allows application of Gauss's theorem, that follows:

$$\frac{\partial}{\partial t}\int_{\Omega} \rho\phi d\Omega + \oint_{\Gamma} J \cdot n d\Gamma = \int_{\Omega} S^{\phi} d\Omega \tag{38}$$

Integrating the generalized transport equation considering a time interval Δt in the control volume Ω, the following finite volume equation can be obtained:

$$\frac{(\rho\phi_p)^{t+\Delta t} - (\rho\phi_p)^{t}}{\Delta t}\Delta V + \sum_{f}^{N_{faces}} \rho_f V_f \phi_f \cdot A_f = \sum_{f}^{N_{faces}} \Gamma_{\phi}\nabla\phi_f \cdot A_f + S^{\phi}V \tag{39}$$

For spatial discretization, it is assumed that properties are constant on a given control volume at a given time in its center of gravity, varying these properties along with elements through interpolation functions in which the most known are centered, upwind (first-order or second-order accuracy), and hybrid, based on Péclet number.

The solvers generally used to handle these equations are pressure-based ones (SIMPLE, SIMPLE-C, PISO, FSM) [30] [31] and density-based solvers (ROE-FDS, AUSM, HLLC) [31] [32] [33].

The present simulation used is an implicit density-based with ROE-FDS scheme, with a second-order upwind scheme applied in the flow and on turbulence model (calculation of kinetic energy and dissipation rates). The condition of convergence is based on the Courant number for a given cell size and time step.

3.3 Structural dynamics approach

We consider the Lagrangian reference frame and a linear relationship between stress and strain in these models.

$$\varepsilon_{ij} = \frac{1}{2}\left(\frac{\partial u_i}{\partial x_j} + \frac{\partial u_j}{\partial x_i}\right) \tag{40}$$

The equations of linear elasticity are derived from linear stress and strain relationship and describe conservation of displacement and are known as equations of motion, in its generalized form, known as Navier-Cauchy equations for linear elasticity.

$$\rho_s \frac{\partial^2 u_i}{\partial t^2} - \nabla \cdot \sigma(u) = 0 \tag{41}$$

To solve numerically **Eq. 41** is used the finite element method (FEM) that divide the solid domain Ω_s (or Ω^s) into multiple finite elements Ω_e and the calculation of the displacement field U_e is performed on each finite element from values calculated on its nodes (points that are part of finite element edges) and interpolated by polynomials.

According to that was described in the preceding paragraph, a linear equation on the element Ω_e can be then obtained:

$$U(x_i, t) = N_e(x_i)U_e(t) \tag{42}$$

where $U_e(t)$ is the nodal displacements unknowns and $N_e(x_i)$ is the interpolation polynomial matrix, polynomials called shape functions (based on Hermite's polynomials).

Using the Galerkin method to discretize $U(x_i, t)$, we obtain the generalized equation of motion for each finite element as follows:

$$m_e \ddot{u}_e + k_e u_e = f_e \tag{43}$$

with elementary mass matrices m_e, stiffness elementary matrix k_e, and external forces vector represented by the element f_e.

Assembling the equations of all elements presented into the domain, we have the generalized equation of motion to the domain Ω_s:

$$[M]\{\ddot{u}\} + [C]\{\dot{u}\} + [K]\{u\} = [F(t)] \tag{44}$$

The equation can be solved using a modal approach in which the solution is composed by eigenvectors of the vibration subproblem, which can be written as n individual equations, corresponding one equation to each vibration shape mode, as follows:

$$\begin{cases} \ddot{u}_i(t) + 2\xi_i\omega_i\ddot{u}_i(t) + \omega_i^2 u_i(t) = f_i(t) & \quad i = 1,2,3,\dots,n \\ f_i(t) = \Phi_i^T[F(t)] \end{cases} \tag{45}$$

where ω_i is the natural frequency for i^{th} mode and ξ_i is the damping parameter for i^{th} mode. To solve this system is necessary to calculate numerically integrals in the mass and stiffness matrices using Gaussian quadrature and after that, solve the linear system to obtain displacement vector through Gauss-Seidel methods and perform modal extraction through Lanczos Method.

3.4 The fluid-structure interface

In the case of the FSI problem we consider a solid domain Ω^s and a fluid domain Ω^f in contact with each other along with the interface $\Gamma_{f/s}$ (as we can see in **Figure 23**). The density of contact forces on the fluid in the solid domain perspective is written as:

$$t_s = \sigma_s n_s \tag{46}$$

Similarly, the density of contact forces on the fluid in the fluid domain perspective is written as:

$$t_f = \sigma_f n_f \tag{47}$$

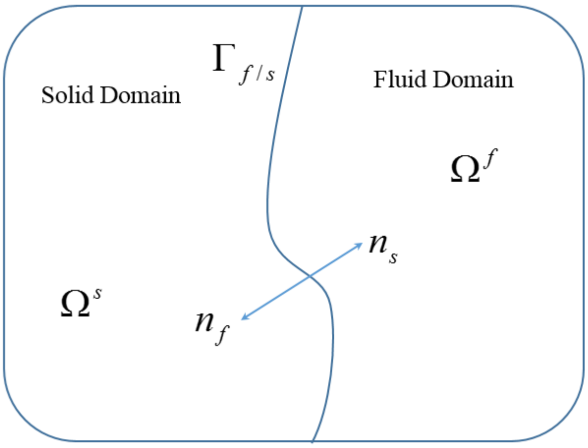

Figure 23: FSI domains

There are the Dirichlet displacement function u and Dirichlet data functions based on velocity vector v on boundary conditions regarding the solid domain. Therefore, two assumptions are made to solve this general problem. The first assumption is that the velocities are continuous along with the interface $\Gamma_{f/s}$, given by:

$$v = \dot{u} \tag{48}$$

The other assumption is relative to the mechanical equilibrium on $\Gamma_{f/s}$

$$t_s + t_f = 0 \tag{49}$$

The normal vectors are linked by the following relationship:

$$n = n_s = -n_f \tag{50}$$

Therefore, the interface equilibrium condition arises:

$$(\sigma_f - \sigma_s) n = 0 \tag{51}$$

To model meshing motion in the fluid domain is necessary to reconcile characteristics of both reference frames seen in **Figure 21**, to allow carry through a control volume quantity of mass and heat, and at the same time, this control volume may deform and move with time.

To meet these requirements, there is an Arbitrary Lagrangian-Eulerian (ALE) formulation that combines the regions in the fluid domain where we need to approximate a Lagrangian formulation to follow particle motion (for example close to the interface between the fluid and the solid domains) and the regions where an Eulerian description is sufficient to describe the flow (far away from solid domain). This formulation is succinctly described by **Eq. 52**.

$$\begin{cases} \text{Find } (v, p) \in V(\Omega_t^f)^d \times L^2(\Omega_t^f), t \in I \text{ such that} \\ \int\limits_{\Omega_t^f} \left[\left.\frac{\partial v}{\partial t}\right|_x + (v-w)\cdot\nabla v \right] \upsilon d\Omega = \int\limits_{\Omega_t^f} \left[p\nabla\cdot\upsilon - \frac{2}{\text{Re}}\nabla v : d(\upsilon) + b_f\cdot\upsilon \right] d\Omega,\ \forall\upsilon \in V(\Omega_t^f)^d \\ \int\limits_{\Omega_t^f} (\nabla\cdot v) q d\Omega = 0,\ \forall q \in L^2(\Omega_t^f) \end{cases} \tag{52}$$

Applying the Galerkin Method, substituting velocity and pressure fields by its discretized versions and the original spaces by approximation spaces and its respective test functions, we have:

$$\begin{cases} \text{Find } (v_h, p_h) \in M_H \times P_H \text{ such that} \\ \sum_{i=1}^{2K} v_i \int\limits_{\Omega_t^f} q_l \nabla\cdot\upsilon_i d\Omega = 0 \\ \sum_{i=1}^{2K} \frac{\partial v_i}{\partial t} \int\limits_{\Omega_t^f} \upsilon_k\cdot\upsilon_i d\Omega + \sum_{i=1}^{2K} v_i \int\limits_{\Omega_t^f} \upsilon_k\cdot(v-w)\cdot\nabla\upsilon_i d\Omega = \\ \sum_{j=1}^{2K} p_j \int\limits_{\Omega_t^f} q_l \nabla\cdot\upsilon_k d\Omega - \frac{1}{\text{Re}} \sum_{i=1}^{2K} v_i \int\limits_{\Omega_t^f} \nabla\upsilon_k : (\nabla\upsilon_i + [\nabla\upsilon_k]^T) d\Omega \\ \forall(\upsilon_k, q_l)_{k=1\ldots 2K; l=1\ldots L} \in M_H \times P_H \end{cases} \tag{53}$$

The spatial discretization of this model is realized by choosing special types of elements, Crouzeix–Raviart that allows a discontinuous approximation of the pressure or Taylor-Hood elements which allows continuous approximation of the pressure. The temporal discretization has the following form:

$$\begin{cases} \nabla\cdot v^{n+1} = 0 \\ \left(\frac{3v^{n+1} - 4v^n + v^{n+1}}{2\Delta t} \right) + \left(v^* - w\right)\cdot\nabla v^* = -\nabla p^{n+1} + \frac{1}{\text{Re}}\nabla v^* \end{cases} \tag{54}$$

with

$$\nabla p^{n+1} = \frac{3}{2\Delta t}\nabla\cdot v^* - \nabla p^n \tag{55}$$

To determine the field velocities, it is necessary to treat the nonlinearities present in the convective term within ALE. This limitation is resolved using the iterative fixed-point method or Picard's method to minimize residues as assures the ALE algorithm convergence.

The position of mesh motion is determined using the spring analogy, suggested by Hartwich and Agrawal [34], in which the strategy was based on the master/slave node relationship between the moving surface points (masterpoints) and vertices located at the other blocks (slave points).

The movement of the masterpoints is based on the displacements obtained from the structural calculation solver. The movement of the slave points depends on the movement of its corresponding master point from point x_m to x_{m+1} and slave points move from x_s to x_{s+1}.

$$x_{s+1} = x_s + \theta(x_{m+1} - x_m) \tag{56}$$

where θ is a decay function that depends on stiffness factor β, in which larger values mean that meshes act like a rigid body and f_{min} ensures optimal remeshing behavior if master nodes present small displacements.

$$\theta = \exp\left\{-\beta \min\left[\left(f_{\min}, \frac{dv}{(\varsigma + dm)}\right)\right]\right\} \tag{57}$$

where dv and dm are spatial gradients and a ς number sufficient small to avoid division by zero.

$$dv = \sqrt{(x_v - x_m)^2 + (y_v - y_m)^2 + (z_v - z_m)^2}$$
$$dm = \sqrt{(x_{m+1} - x_m)^2 + (y_{m+1} - y_m)^2 + (z_{m+1} - z_m)^2} \tag{58}$$

Figure 24 summarizes fluid-structure Interaction numerical calculation. CFD and CSD (FEM) solvers perform calculations normally in regions where the domain is purely solid or fluid. In the fluid-structure interface region, the ALE solver performs the fluid computation by emulating a Lagrangian fluid particle frame, interpolating information in the solid mesh of the interface region the virtual displacements resulting from the velocity field and the forces from the pressure field (**Figure 24**).

The FEM solver calculates the deformations, and the equilibrium condition of the interface is checked by the coupling module. If this condition is not attained, the coupling module sends the deformations calculated by the FEM solver to the dynamic mesher of the fluid domain, which deforms the mesh and the calculations restart, and the iterations continue until the equilibrium condition is reached.

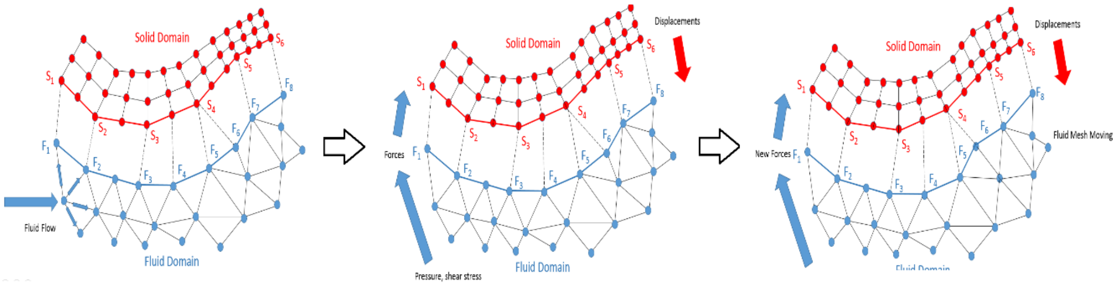

Figure 24: Mesh domains coupling and interpolation

3.5 Airplane model

From reports and other sources of information [35] [36], the external geometry (**Figure 25**) and structural layout of KC-135 could be obtained. The detailed structural layout could also be then defined, as well as the flight envelope of the airplane (**Figure 26**), and the *V-n* diagram (**Figure 27**). The highest load factor is 2.5 and the lowest is -1.

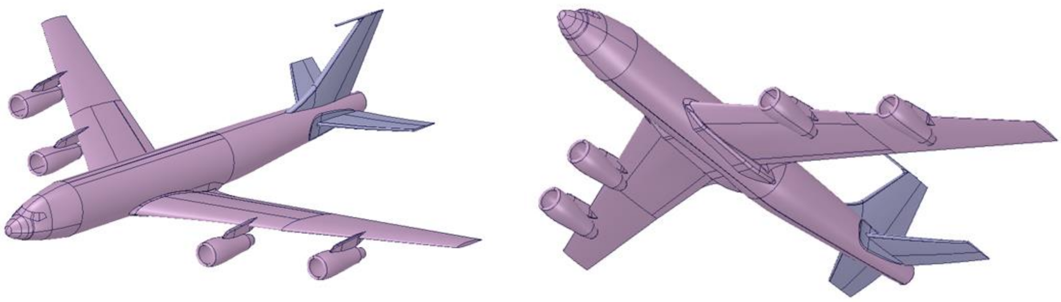

Figure 25: CAD model of the KC-135

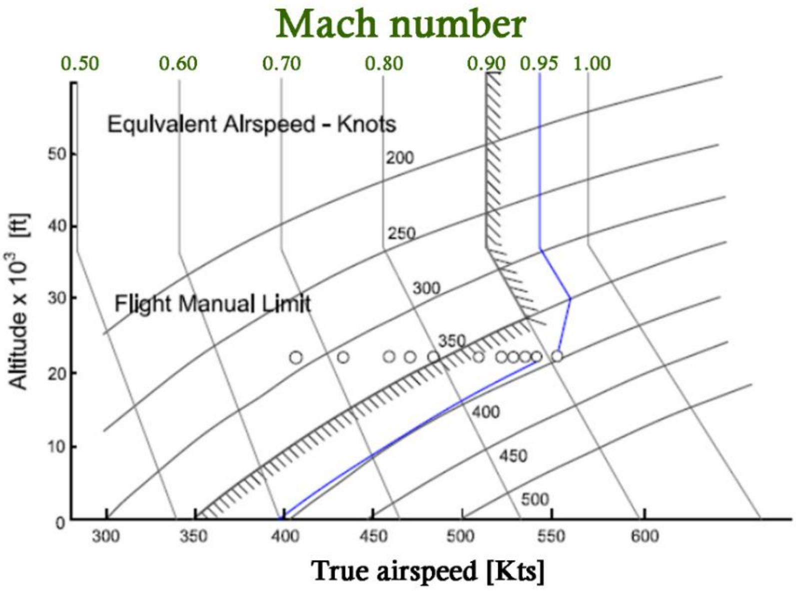

Figure 26: Boeing KC 135 Stratotanker flight envelope [35]

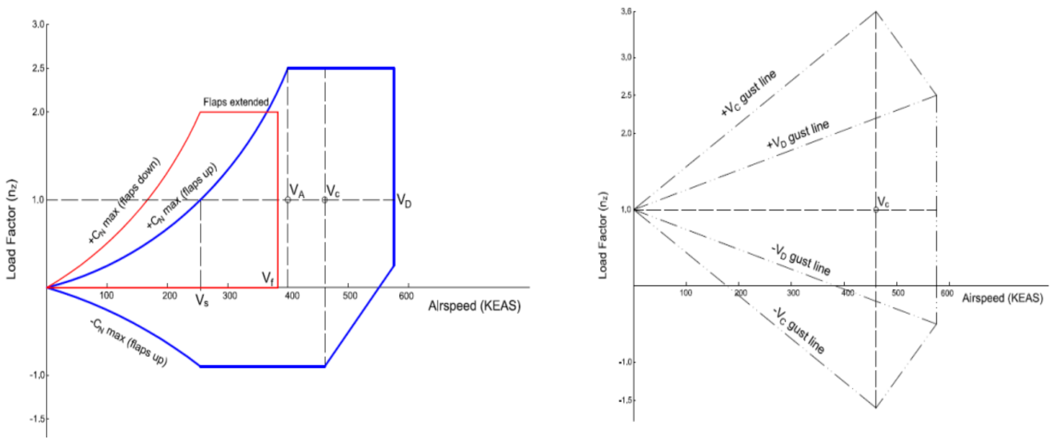

Figure 27: V-n diagram for the structural sizing of KC-135

Figure 28 shows the structural calculation procedure for the sizing of the KC-135 wing. Based on the collected performance data of the aircraft, the loads and load distributions along the wingspan and the chord could be calculated. The load calculation considers cases from maneuvers, gust loads, rolling acceleration, flap and aileron deflections, fuel tank, and engine weights. However, it is necessary to ensure proper safety margins to withstand unforeseen loads at adverse operational conditions.

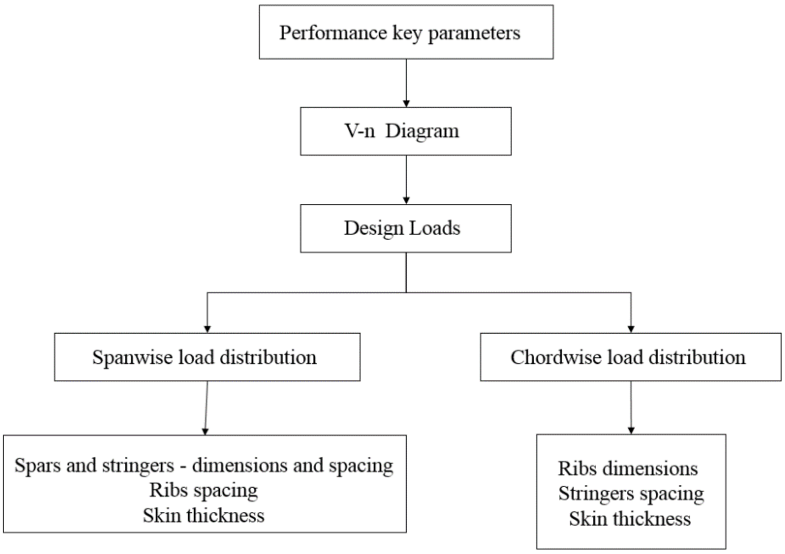

Figure 28: Calculation procedure of KC-135 wing structural elements

The spanwise distribution of bending moment and shear force is important for sizing components whose buckling, and shear stresses are significant, such as stringers and spar sections. The inertia moment of the structure also depends on the number of stringers and spacing of both stringers and spars. Chordwise distributions are important for sizing the local buckling of the stringers and the shearing stresses under the ribs. The thickness of the skin is influenced by the spanwise and chordwise loadings that affect the panel buckling at each wing station. Some dimensions of wing structural elements are shown in **Table 5**. The actual dimensions were obtained from [37], [38], and [39]. The calculated values agree very well with them. The rebuilt wing structural layout can be seen in **Figure 29**.

Table 5: Calculated wing structural elements and their comparison with available data

	Calculated	Data
The average thickness of wing skin [in]	0.050	0.038
Ribs minimum thickness range [in]	0.025-0.098	-
Maximum allowable spacing of ribs [in]	32.48	26.4-28.5
Maximum allowable spacing of stringers [in]	13.39	12.5
The chordwise relative position of spars [%]	23.5/65	23/65
The average thickness of spars [in]	0.285	0.32
Wing mass [kg]	11320	10859 [25] 11462 [24]
Fraction of wing weight in terms of MTOW* [%]	8.40	8.05-8.50
* $MTOW_{Ref}$=*134838 kg* [24]		

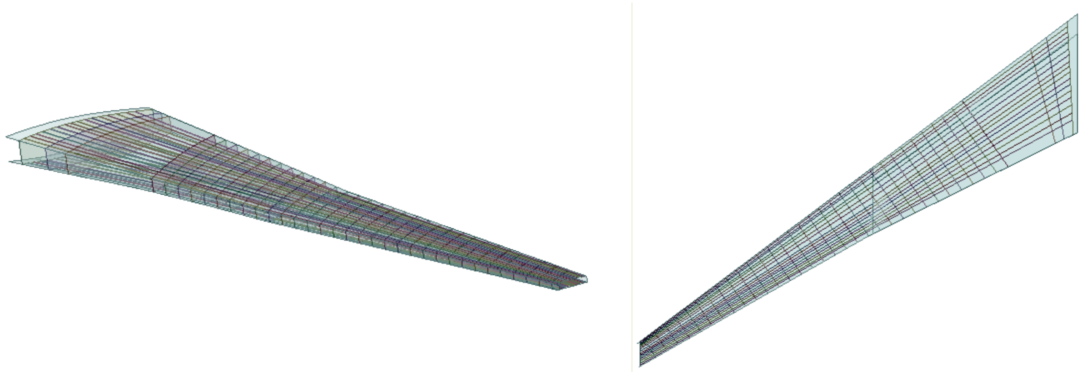

Figure 29: Structural layout of the rebuilt KC-135 wingbox

After the creation of the geometrical model, the CSD and CFD computational meshes were built. The finite element meshes contain quadrilateral shell elements to comply with the skewness criteria of elements as close as possible to 0, which guarantees the accuracy of the analysis (**Figure 30**). In the case of the structural model, the meshes referring to the geometry of the outer surfaces of the wing were defined as the fluid-structure interaction interfaces as well as the communication parameters with the Multiphysics coupling module, discretized in quadrilaterals shell elements with skewness values between 0.22-0.26. CFD meshes were generated using tetrahedral and hexahedral elements to meet the orthogonal quality criteria of cells close as possible to 1, to ensure the convergence and the use of inflation close to the walls, to allow the accurate calculation of the boundary layer in the region through interpolation of the wall functions. The mesh of the fluid model was discretized in tetrahedral elements with orthogonal mesh metrics values between 0.85-0.92.

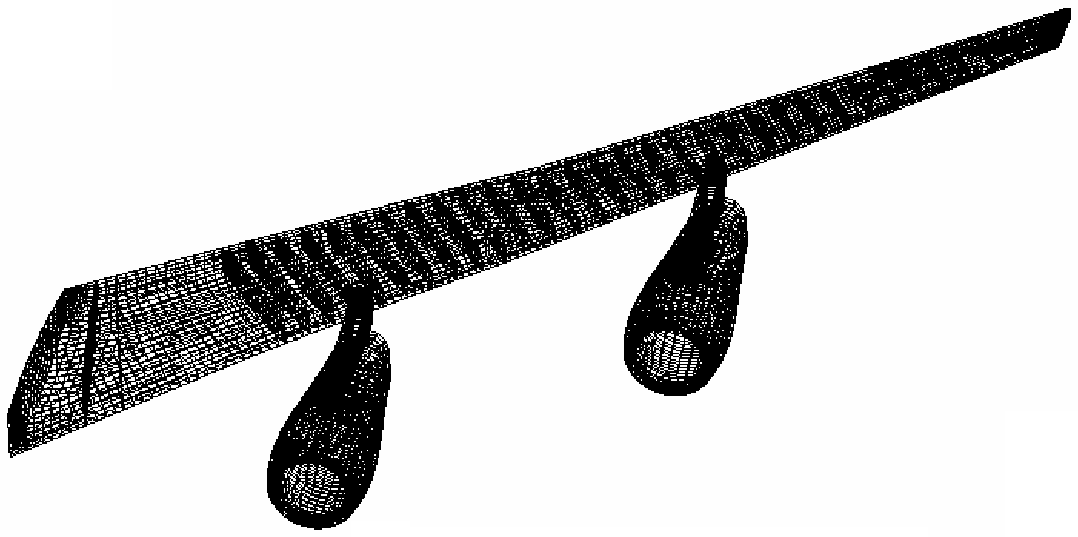

Figure 30: CSD finite element model

3.6 Results

Simulations considering rigid and elastic models were carried out. Their results were compared with wind tunnel data (rigid) and flight test ones (flexible). The wind tunnel runs were carried out for two scaled models: one featuring winglets; the other had no winglets. The flight test is only concerned with a version of KC-135 fitted with winglets. The winglet was also introduced into the computational models, and it features a 15º dihedral angle and a -4º twist.

Figure 31 shows the results of a transonic flow simulation for the configuration with no winglets. As expected, there is an excellent agreement between the calculated distribution and the wind tunnel data. **Figure 32** presents two distinct calculated *Cp* distributions for the configuration fitted with winglets: one obtained with a pure CFD simulation; the other considering a simulation encompassing FSI. Again, the fluid dynamic simulation, which considers that the model is rigid, agrees very well with wind tunnel data whereas the simulation considering aeroelastic effects is in perfect accordance with flight test data.

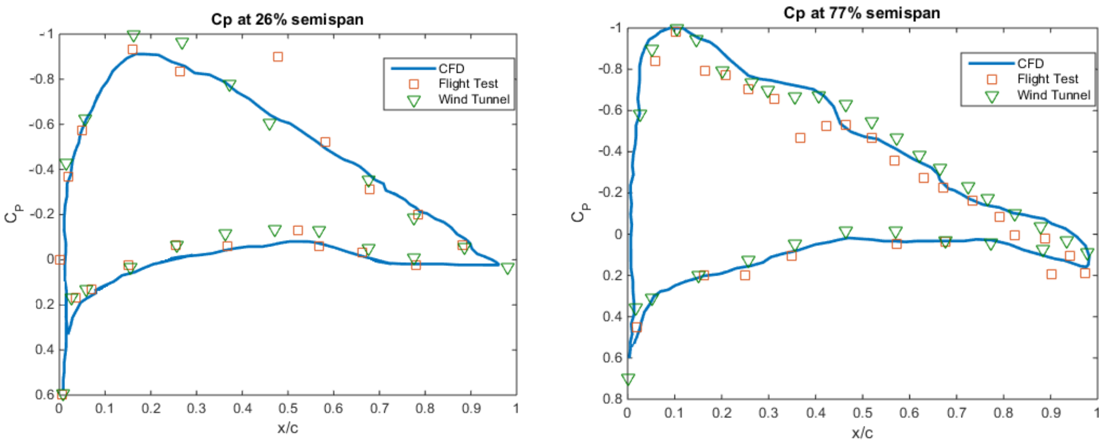

Figure 31: Calculated Cp distributions for the rigid model wing with no winglets compared with wind tunnel test and flight test data (Mach = 0.70, α = 3.5º)

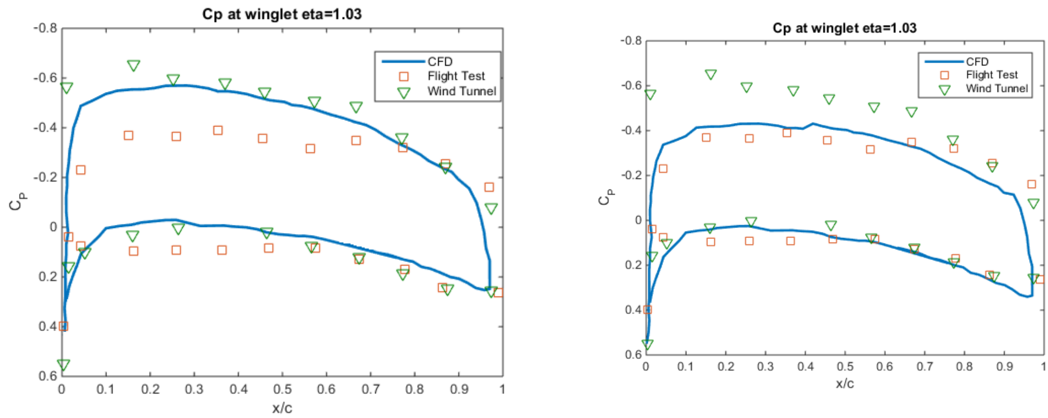

Figure 32: Calculated Cp distributions for the rigid and flexible models fitted with winglets. At left, Cp distribution in a winglet station for a CFD solution. At right, the FSI simulation results agree very well with flight test data (Mach = 0.70, α = 3.5º)

In **Figure 33**, calculated elastic displacements for the baseline configuration without winglets and the KC-135 wing fitted with winglets. The wing fitted with a winglet presents a greater displacement at the wingtip. A wider range of wingtip displacements at a freestream Mach number of 0.76 and for a wider range of lift coefficients can be seen in **Figure 34**. This includes some winglet twist variation for a fixed dihedral angle of 15º.

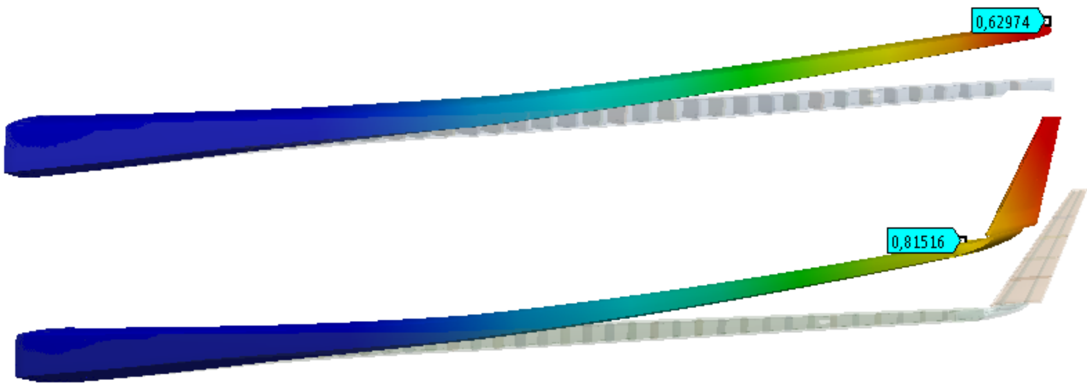

Figure 33: Calculated wingtip displacement in meters (Mach = 0.70, α = 3.5º)

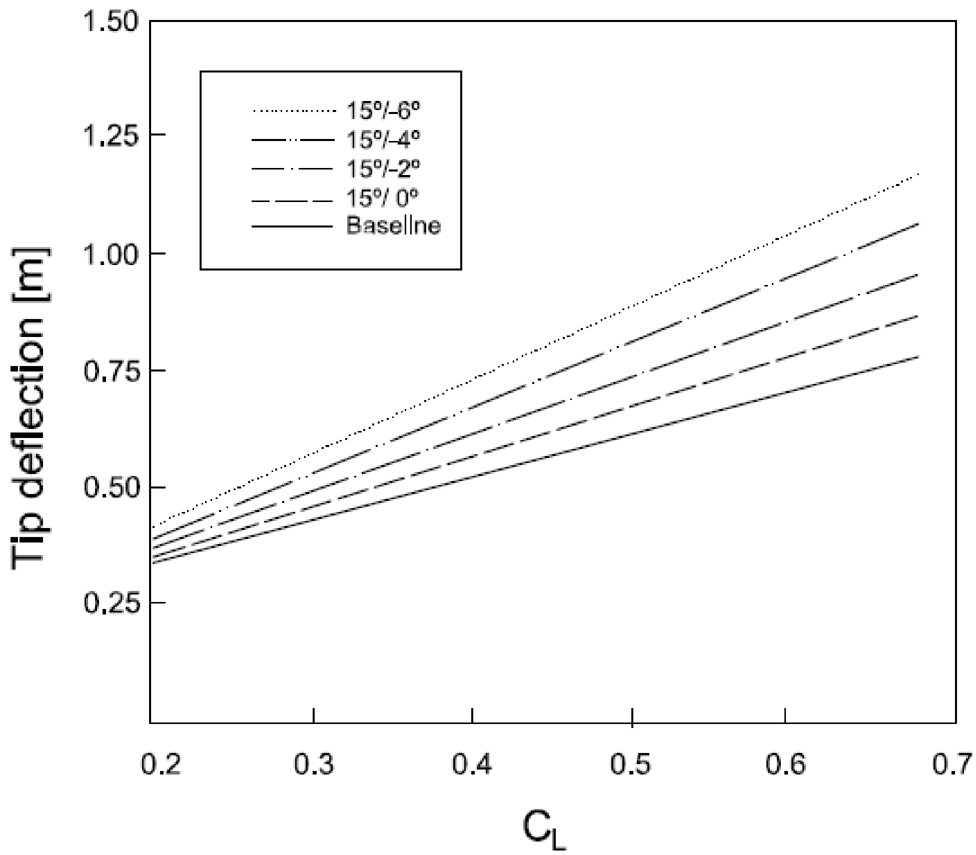

Figure 34: Wingtip deflection for some winglet configurations

Figure 35 reveals that the addition of winglets to the KC-135 configuration reduced the modal frequencies. The addition of winglet weight at the wingtip region, behind the elastic line, therefore, increases the moment of inertia there and may decrease flutter speed. The additional lift generated at the wingtip increases the bending moment at the wing root, demanding a slightly heavier structure. There is an extended aerodynamic effect due to the winglet presence on the configuration. Comparing the lift distribution to the wing without winglets, the unloading of the central and inner part of the wing may further reduce the drag coefficient at transonic conditions due to the eventual reduction of the strength of shock waves there.

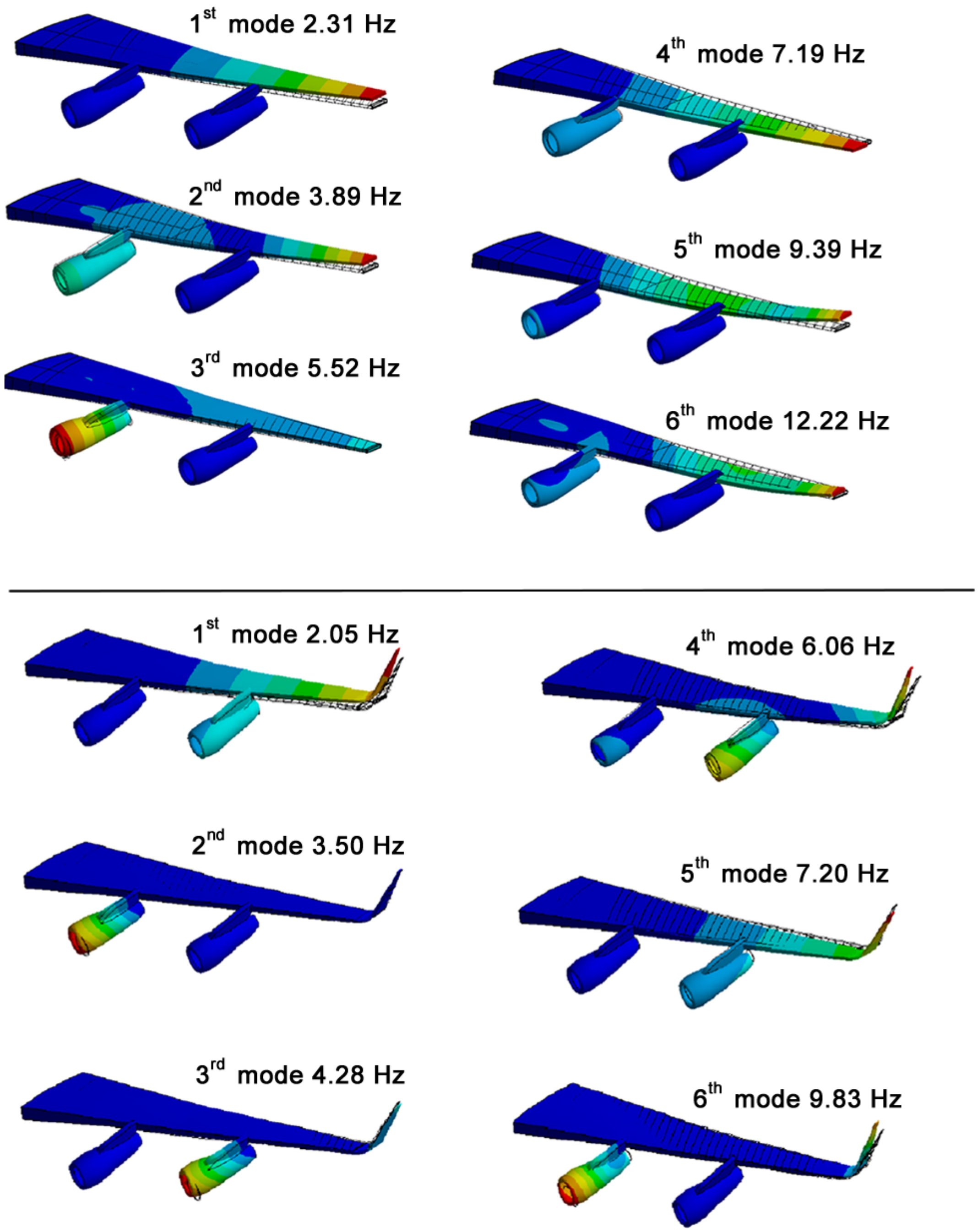

Figure 35: Mode shapes and frequencies of KC-135 wing with and without winglets

4. Considerations about flow modeling

In the applications, concerning optimization of transport aircraft that are shown in the following Sections, the flow model that was adopted for calculating aerodynamics was the full potential one. Because of this, it is important to address the advantages and drawbacks of such a formulation, as well as to justify its use here.

During the computation of airplane mission performance, where critical masses like the MTOW must be accurately calculated, aerodynamic coefficients are intensely required. For this purpose, aerodynamic databanks are usually built up with computational fluid dynamic analyses, wind tunnel data, or a combination of both. In this approach, only the total drag is modeled, and not its components, and this leads to inaccurate interpolations. The alternative to this is the call of aerodynamic codes in real-time. In the case of Euler or RANS formulations, this is not viable, because of the high computation time that is necessary for every flow condition. A realistic mission calculation may require more than one hundred runs for aerodynamic coefficient calculation at each step of the mission. This means that even for full potential codes, which require an average computation time of one minute for a transonic case calculation, an MDO task, where thousands of airplanes must be evaluated, can become a burden for a Linux cluster composed of few processors. A metamodel of aerodynamics offers an elegant and viable alternative to overcome those limitations. Thanks to its faster calculation time, full potential codes are an attractive formulation for the build-up of databases for the training of ANNs.

A viable alternative for MDO computations is the utilization of full potential codes with viscous and non-isentropic corrections [40]. Their cost-benefit makes this formulation extremely attractive for external aerodynamic calculations of aircraft configurations inside an MDO process, which requires extensive calls of the flow analysis codes for performance, load, and stability calculations. However, the extremely sensitive nature of transonic flow regarding airplane geometry, in which geometric variations of lifting surfaces in the order of boundary-layer thickness or lower lead to significant changes in pressure distribution, makes it mandatory that integral boundary-layer routines be coupled with the transonic potential codes. Besides delivering satisfactory zero-lift drag values, the viscous coupled calculation shall also be able to handle shock-boundary layer interaction. Tinoco affirms that the full potential equation offers a quick alternative for analyzing transonic flow with a good degree of accuracy [41]. **Eqs. 59** and **60** are the non-stationary three-dimensional equations of the full potential in three dimensions.

$$\frac{\partial \rho}{\partial t}+\frac{\partial(\rho\phi_x)}{\partial x}+\frac{\partial(\rho\phi_y)}{\partial y}+\frac{\partial(\rho\phi_z)}{\partial z}=0 \tag{59}$$

$$\rho=\left[1-\frac{\gamma-1}{\gamma+1}\left(\phi_x^2+\phi_y^2+\phi_z^2\right)\right]^{\frac{\gamma}{\gamma-1}} \tag{60}$$

In **Eq. 60**, γ is the isentropic expansion factor, the ratio of the heat capacity at constant pressure to heat capacity at constant volume. The velocity components on the x, y, and z axes are u, v, and w, respectively, and they can be obtained by deriving the potential for velocities ϕ:

$$\begin{aligned} u &= \phi_x \\ v &= \phi_y \\ w &= \phi_z \end{aligned} \tag{61}$$

For acceptable solutions of the full potential equation, it is recommended that the Cartesian mesh close to the body be normal to it. The full potential equation can be written in strong conservation-law form for a general, body-conforming, curvilinear coordinate system (**Figure 36**). As an example, for the bi-dimensional equation:

$$\left(\frac{\rho U}{J}\right)_{\xi} + \left(\frac{\rho V}{J}\right)_{\eta} = 0 \tag{62}$$

Here, ξ is the chordwise coordinate, η is the coordinate in the normal direction regarding the airfoil. J is the Jacobian of the coordinate transformation. If velocities are made dimensionless concerning the critical speed of sound (a*), the density can be expressed as

$$\rho = \left[1 - \frac{\gamma - 1}{\gamma + 1}\left(U\phi_{\xi} + V\phi_{\eta}\right)\right]^{1/(\gamma-1)} \tag{63}$$

Eq. 63 also assumes that density is made dimensionless concerning stagnation density. Moreover, the present formulation considers mass and momentum conservation, besides the isentropic hypothesis.

The nomenclature that is typically adopted is the standard one, such that ϕ is the full velocity potential, and the subscripts indicate partial derivatives concerning each of the spatial coordinates. The contravariant velocity components, U and V are given by

$$U = A_1\phi_{\xi} + A_2\phi_{\eta} \tag{64}$$
$$V = A_2\phi_{\xi} + A_3\phi_{\eta} \tag{65}$$

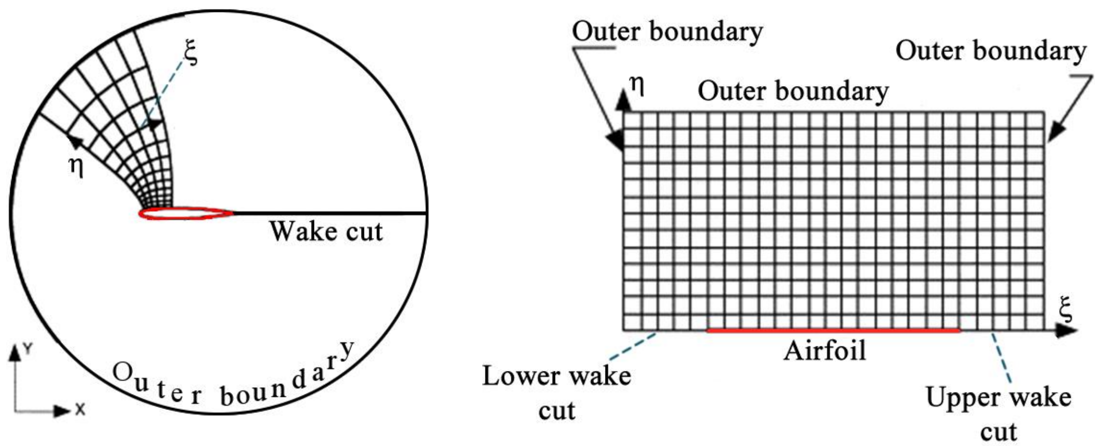

Figure 36: Coordinate transformation and mesh topology

Holst [42] reviewed various potential equation forms with emphasis on the full potential equation. The review also discussed applicable mathematical characteristics and all assumptions adopted for equation derivation. The impact of the derivation assumptions on simulation accuracy, especially concerning models for the capture of shock waves was analyzed. The extensive article also contains the description of key characteristics of all numerical algorithm types employed for solving nonlinear potential equations, including steady, unsteady, both space and time marching, and design methods. Both spatial discretization and iteration scheme characteristics were examined by Holst.

The full potential code employed here presents the following characteristics:

- It solves the three-dimensional full potential equation in the conservative form.
- The airplane configuration to be analyzed is comprised of the fuselage, low wing, and winglet.
- Both subsonic and transonic flow can be calculated.
- The implicit AF2 algorithm [1] is employed for the time-marching in the pseudo time [43].
- A fast viscous-inviscid coupling with a blowing technique is utilized for 3D calculations.
- The location of flow transition can be prescribed. In the present work, the value of 5% of correspondent reference length was used.

A non-isentropic correction is applied to the pressure coefficient (*Cp*) distributions [44].

To demonstrate the accuracy and cost-benefit for employing full potential codes in conceptual design, a comparison of *Cp* distributions from Euler and RANS codes with those from full-potential solutions was carried out for a transonic airfoil flow as well as for the airflow on a twinjet airliner with rear-mounted engines.

The two-dimensional FPE2D full potential code used the formulation described in Mattos [45] and the simulation was used to calculate a transonic flow over an 11.823%-thick airfoil, called here ITADX4. The convergence history is shown in **Figure 37** as well as the Mach number contours of the converged solution. The Euler code used to calculate the flow over the same airfoil at the same conditions is the NSC2KE developed by Bijan Mohammadi [46]. This is a finite-volume Galerkin program computing 2D and axisymmetric flows on unstructured meshes. To solve the Euler part of the equations, a Roe, Osher, and a kinetic solver are available. To compute turbulent flows a k-epsilon model is available [46]. **Figure 38** shows a comparison between the *Cp* distribution on airfoil from the full potential code and the Euler solution. As expected, the conservative full potential solution shock location lies behind that of the Euler solution and it turns out to be a stronger shock wave than that from the Euler formulation. However, if a non-isentropic correction is applied to the full potential solution, both distributions will match closely [44].

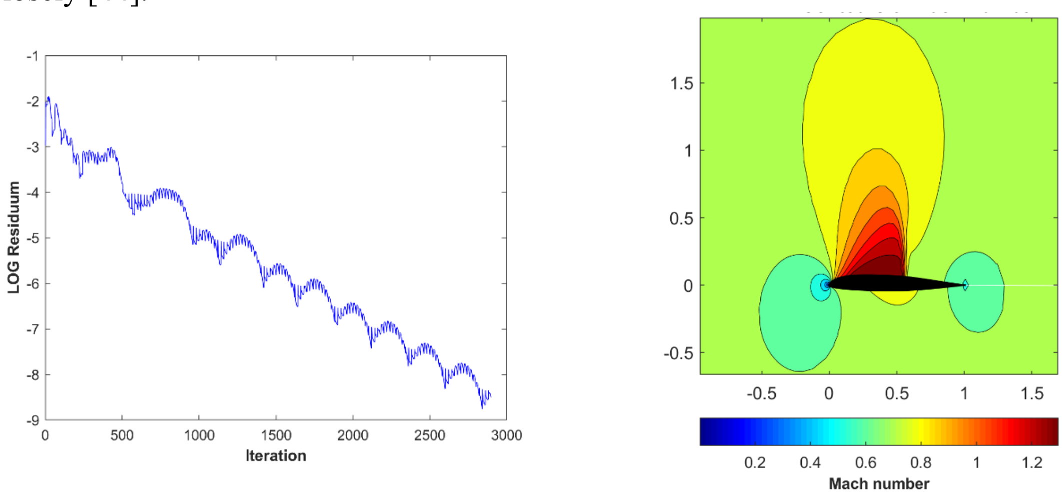

Figure 37: Solution of a transonic flow calculated over the airfoil ITADX4 with a full potential code (M_∞= 0.73 and 1.5º angle of attack)

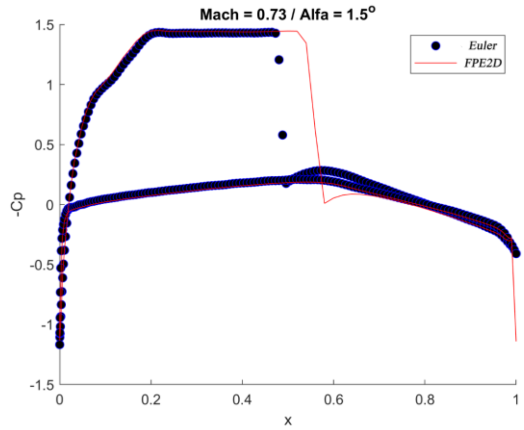

Figure 38: Comparison of *Cp* distributions for the ITADX4 airfoil obtained by an Euler solution and with the one from full potential code

An inverse technique was developed for this code [45] [47]. From a prescribed Cp distribution and an initial airfoil geometry, a new geometry that satisfies the prescribed distribution at the desired flight condition can be found just in a few interactions of the redesign process. The difference between the prescribed and existing pressure distribution is translated into a normal velocity to airfoil or wing geometry. Through an interactive process where the geometry is modified, this difference is progressively eliminated.

A test case that handles the design of a supercritical profile for a specific flow condition was chosen to demonstrate the capability of the inverse design technique. The pressure distribution calculated with the code FPE3D for the profile RAE2822 with Mach number = 0.730 and angle of attack 2° is characterized by a moderate compression shock located at 65% of the chord. The prescribed pressure distribution, shown in dashed lines in **Figure 39**, eliminates the shock wave on the upper surface. The design process converged after 24 cycles and **Figure 39** shows that there is a particularly good agreement between the calculated pressure distribution and the prescribed one. **Figure 39** also compares the RAE2822 profile to the obtained with the inverse technique that typically converges in a few interactions **[47]**. The RAE2822 airfoil was mainly modified on the upper surface after the shock location by a flat curve extension, with its nose geometry suffering almost no modifications. However, the inverse technique presents the disadvantage of undesirable behaviors off the design point. However, conjunctly with optimization techniques, it can be incredibly useful within a multi-objective optimization context.

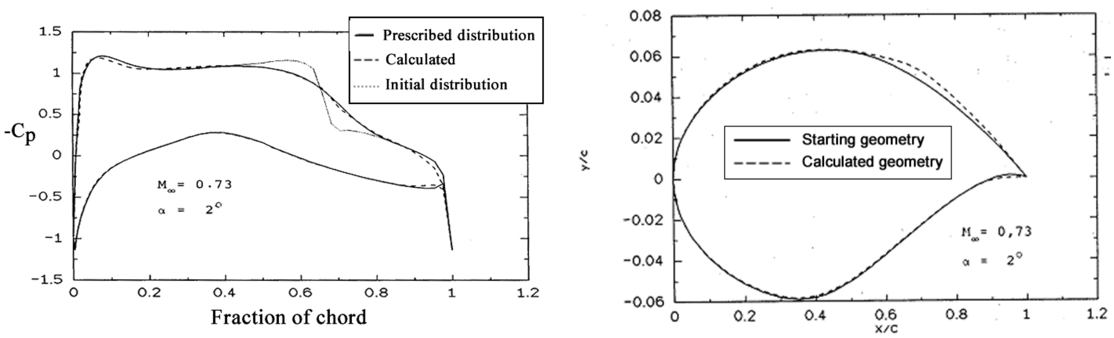

Figure 39: Example of the inverse technique application for airfoil design at a transonic condition (M_∞= 0.73, α=2º) [45] [47]

The TRE planform has a typical shape designed for the transonic regime: the twist between the wingtip and the wing root is 4°, the aspect ratio is 8.4, the leading-edge sweepback angle is 25.5°, a taper ratio of 0.22, and the root profile is 15% thick. The TRE planform can be seen in **Figure 40**. The computing mesh comprises 60x21x30 points in ξ-, η- or ζ-direction, respectively.

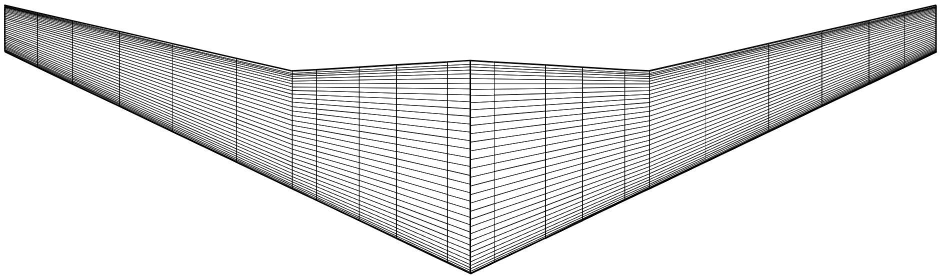

Figure 40: TRE-planform with surface mesh

A complete configuration with the TRE planform was investigated for a wide range of Mach numbers in Boeing's transonic wind tunnel [45]. The configuration includes fuselage, tail units, wings, winglets, and rear-mounted engine nacelles. The experimental measurement data used here were obtained for a variant without a vertical stabilizer. The numerical calculation was performed with the DWING full potential code for wing-alone configuration.

Figure 41 shows the calculated and measured pressure distributions for wing stations at 22% and 66% of the wingspan respectively at a Mach number of 0.70, α=0.365°. For the inboard station, the flow has a moderate compression shock in the front area and is slightly overcritical in the suction tip of the station at 66% of the wingspan. There is a very good agreement everywhere between the experimental Cp values and the pressure distribution calculated by DWING. Due to a missing pressure sample at the bottom of the trailing edge, it is not possible to make a direct comparison of both pressure distributions at this point. In this part of the wing, the viscous effects are of great importance and their effect on the geometry is expressed by a decambering effect of the airfoil geometry in this region.

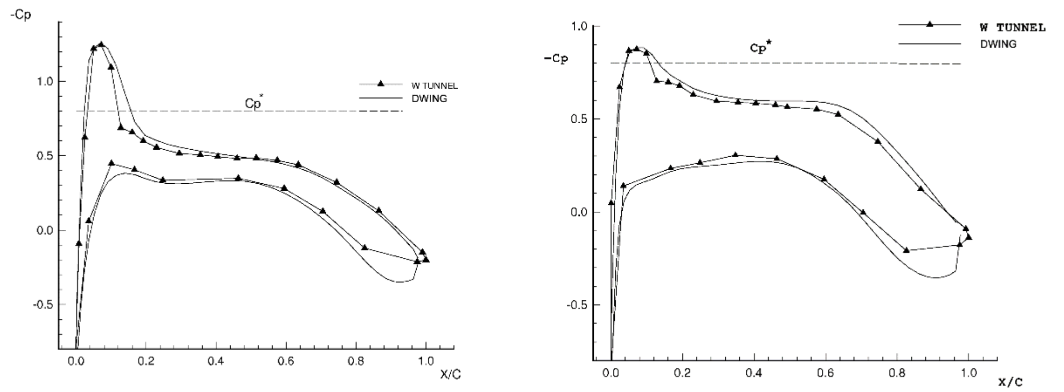

Figure 41: Pressure distributions for a station of the TRE planform at 22% (at left) and 66% (at right) of the wingspan. Mach = 0.700, α = 0.365°

For the analysis of the twinjet airliner designated ITA50SR (**Figure 42**), the RANS simulation [48] employed the SST k-ω turbulence model, and the hexahedral mesh that was created for the simulation was composed of approximately 2.1 million cells. Making use of an implicit scheme for time marching, the convergence was reached after all residuals dropped to values below $1x10^{-4,}$ which consumed 5675 iterations and some mesh adaptions [49]. Each iteration running on three cores of a desktop computer fitted with an Intel® Core™ i5-11600K processor demanded on average 18 secs. The full potential solution for the wing-fuselage combination took 25 secs to converge on the same machine. **Figure 42** shows contours of velocity magnitude over the airplane and **Figure 43** shows a comparison between the results from the RANS simulation and the full potential code. There, *Cp* distributions for two wing stations of the airliner of ITA50SR are shown. The agreement between the related *Cp* distributions is particularly good. In addition, Mattos et al. show another comparison between a RANS code and a full potential one, where drag coefficients were computed for a wing-body-winglet configuration [50]. There is a particularly good agreement between both flow formulations.

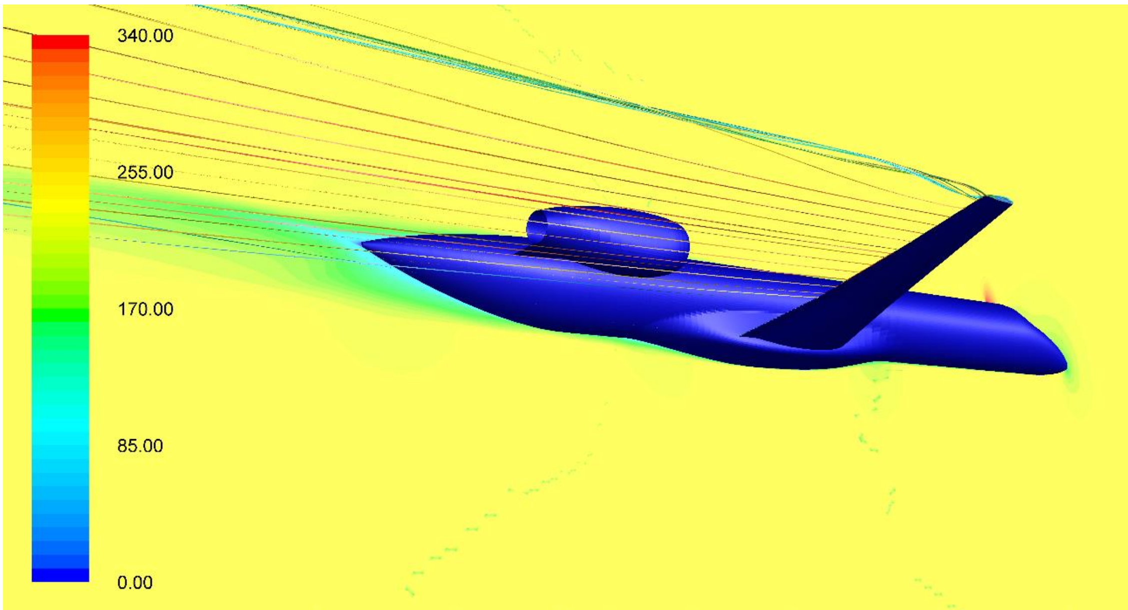

Figure 42: Contours of velocity magnitude for the ITA50SR airliner (M_∞ = 0.775, α=1.21º)

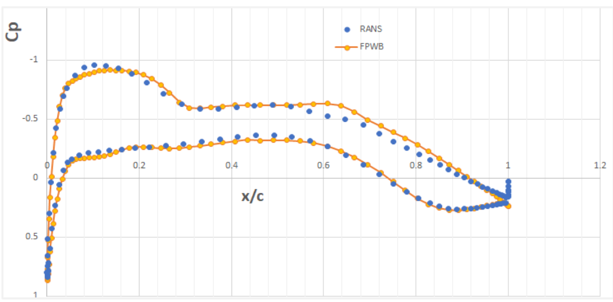

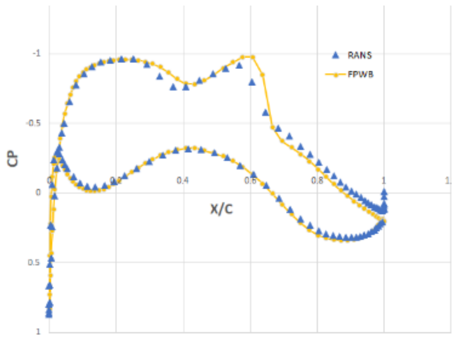

Figure 43: *Cp* distributions obtained with a RANS code and a full potential one for the ITA50ADV airliner. At left, station a 22% of semispan; right, station located at 50% of semispan (M_∞ = 0.775, α=1.21º, Reynolds number of 15x10^{6})

5. Machine Learning overview and applications

5.1 Introduction

Machine learning is the elaboration and application of computational techniques to discover patterns and trends contained in data (call it experience, to some extent). Machine learning algorithms can learn information directly from data, without relying on a predetermined equation as a model. Sometimes is almost impossible to derive equations or a system of equations to model a physic phenom. In other cases, even considering that a system of differential equations is available, it can be very costly to solve and therefore surrogate models are a good option.

Machine learning algorithms improve their performance adaptively as the number of samples available for learning increases and it can be split into two types of techniques (**Figure 44**): supervised learning, which trains a model from known input and output data enabling predictions when inputs of non-trained data are provided; and unsupervised learning that finds hidden patterns or intrinsic structures in the input data.

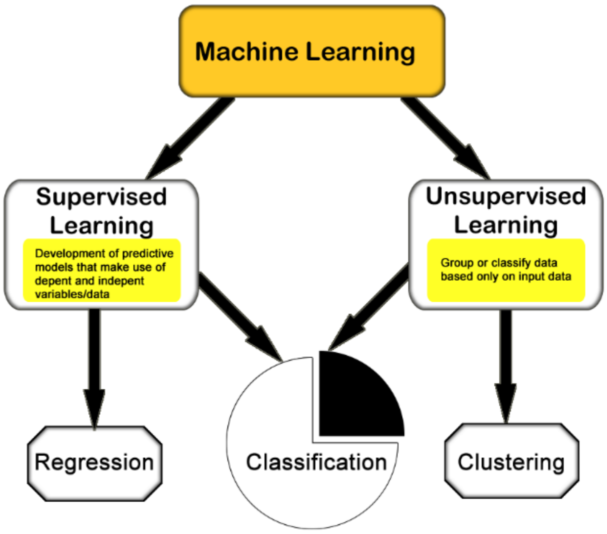

Figure 44: Machine learning branches

The main goal of supervised machine learning is to build a model that makes evidence-based predictions in the presence of uncertainty. A supervised learning algorithm employs a known set of input data and known responses to the data (output) to create a model that generates accurate predictions when new and untrained data is supplied. Supervised learning uses classification and regression techniques to develop predictive models. In other words, supervised learning can be defined by using labeled datasets to train algorithms that classify data or accurately predict outcomes.

Classification techniques properly provide for categorical answers. A simple example is whether an email can be categorized as genuine or as spam. Another example is predicting the imminence of a heart attack. Classification models sort input data into distinct categories. Typical applications naturally include medical imaging, speech recognition, customer behavior, and credit score. Classification can be precisely defined as the process of assigning a label to an object based on its characteristics according to a class. Problems can involve any number of them, which are defined as a group containing objects that share attributes. In binary classification, however, two classes are only allowed.

Regression analysis is widely used for prediction and forecasting, where its use has substantial overlap with the field of machine learning. Prediction of oil prices and stock prices are examples of application. In some situations, regression analysis can be used to infer causal relationships between the independent and dependent variables. Importantly, regressions by themselves only reveal relationships between a dependent variable and a collection of independent variables in a fixed dataset. To use regressions for prediction or to infer causal relationships, respectively, a researcher must carefully justify why existing relationships have predictive power for a new context or why a relationship between two variables has a causal interpretation. The latter is especially important when researchers hope to estimate causal relationships using observational data.

Unsupervised learning discovers hidden patterns or intrinsic structures in the data. It is used to make inferences from datasets that consist of input data without labeled responses. Grouping is the most common unsupervised learning technique. It is used for exploratory data analysis to find hidden patterns or data groupings. Applications for grouping include gene sequence analysis, market research, and object recognition.

There are plenty of supervised and unsupervised machine learning algorithms (**Figure 45),** and each has a different approach to the learning process [51]. Merely choosing a good one may prove difficult because there is no direct approach or the best method and therefore finding the right algorithm for a particular problem. Highly flexible representations tend to super-adjust data by modeling small variations that can be noised; simple ones are easier to interpret and faster to run but may inevitably have less accuracy. Therefore, choosing the right algorithm requires exchanging one benefit for another, including speed, accuracy, and complexity of the model. Trial and error are the essences of machine learning - if one used the approach or used algorithm does not work, the concerned user must merely try another.

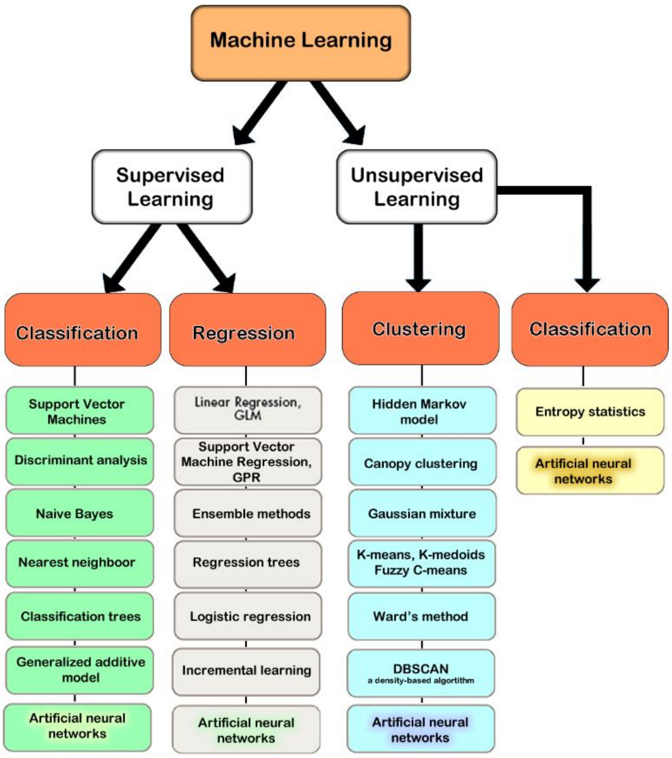

Figure 45: Supervised and unsupervised learning algorithms

Kireev et al. developed Self-Organizing Maps (SOM) to solve a classification problem of large databases of chemical reactants [52], i. e., an application of unsupervised learning with Korhonen neural networks. With the utilization of entropy statistics, Frenken and Leydesdorff [53] analyzed scaling patterns in terms of changes in the ratios among characteristics of 143 configurations of commercial transport aircraft. In their research, the piston-powered DC-3, and the jet-powered Boeing 707, were revealed to have triggered scaled trajectories. Some configuration characteristics of both airplanes have been scaled at different moments in time, which points to the versatility of a dominant design that allows a firm to react to a variety of customer requirements. Scaling at the level of the industry took off only after subsequently re-engineered models were introduced, like the piston propeller Douglas DC-4 and the twin-aisle Boeing 767. The two scaling trajectories in civil aircraft corresponding to the piston propeller and the turbofan paradigm can be compared with a single, less pronounced scaling trajectory in helicopter technology for data during the period 1940–1996 [53]. They state that management and policy implications can be specified in terms of the phases of codification at the firm and the industry level, thanks to the entropy statistics analysis.

5.2 Artificial neural networks

Artificial Neural Networks (ANNs) are a special type of machine learning algorithms that are modeled similarly as information is processed by the human brain. That is, just like how the neurons in our nervous system can learn from the past data, similarly, the ANN can learn from the data and respond to the form of predictions or classifications. ANNs are nonlinear statistical models which display a complex relationship between the inputs and outputs to discover a new pattern. They can be used for a broad range of applications such as image recognition, regression, speech recognition, machine translation as well as medical diagnosis. ANNS can handle a mix of many variables of different types (logical, real, integer). They can also deal with a large amount of data, whereas usual regression methods do not.

An important advantage of ANN is the fact that it learns from the example data sets. The most common usage of ANN is that of a random function approximation. With these types of tools, one can have a cost-effective method of arriving at the solutions that define the distribution. ANN is also capable of taking sample data rather than the entire dataset to provide the output result. With ANNs, one can enhance existing data analysis techniques owing to their advanced predictive capabilities.

A neural network is an interconnected structure of processing elements, called nodes, whose goal is to mimic the biological neuron. Weights are attributed to the inter-unit connections, and they are obtained by a process of adaptation from a set of training data. After the trained ANN is stimulated with a group of inputs, the signal processing through the neuron layers will produce an output, simulating an interpolation of the database.

Lipmann [54] performed a description of the evolution of ANN research and McCulloch [55] presented one of the first mathematical models of ANN. Rosenblatt [56] introduced and endorsed the single-layer perceptron (Linear Neurons) network for classification problems. However, Minsky [57] stated the weakness of perceptron architecture. This led to some disinterest in the ANN research field [58] until the development of new network architectures and learning methods, such as the back-propagation algorithm [59].

ANNs find applications in many areas such as pattern recognition, non-linear control, optimization, and decision making. The use of ANN also improved the techniques for computer speech and image recognition [60]. There are many neural network types and architectures. Below, short descriptions of some of the most known types are provided:

- *Feedforward Neural Network – Artificial Neuron*. This is the simplest type of ANN, where the data or the input flows from input to output layers, going through the intermediate layers to the output nodes. Hidden layers are optional in the architecture and there are not any loops in this network type. Feedforward networks are utilized for any input to output mapping [61].
- *Radial basis function Neural Network*. The radial basis function (RBF) is a real-valued function whose value depends only on the distance between the input and some fixed point, which can be the origin or some other fixed point. Sums of radial basis functions are used to approximate intricate functions. In an RBF network, radial basis functions perform the role of the activation function.
- *Kohonen Self Organizing Network*. A Kohonen network maps inputs of arbitrary dimension to a discrete neuron map. A Kohonen map is an unsupervised learning (self-organizing) model. It is a method for dimensional reduction, as high-dimension inputs are mapped into a lower-dimensional discretized representation and conserve the implicit structure of its input space. When training the map, the location of the neuron remains constant, but the weights will differ depending on the value [62]. This self-organization process has distinct steps: initially, every neuron weight is initialized with a small value in the input vector; in the second phase, the neuron closest to the point is then selected as the *winning neuron* and the neurons that are linked to it will also move towards that point. The distance between the point and the neurons can be calculated by the several distance approaches like, for instance, the Euclidean one, and the closest neuron is then taken as the winner. Through the interactive process, all points are clustered, with each neuron representing each kind of cluster.
- *Recurrent Neural Networks* are based on the principle of feeding the output of a layer back to the input to help in recalibrating neuron weights to better predict the outcome of the layer. Here, the first layer is formed like the feed-forward neural network with the product of the sum of the weights and the features [62]. Indeed, the recurrent neural network process starts once this is calculated. Thus, from one-time step to the next, each neuron will remember some information recorded in the previous time step. This way, each neuron acts as a memory cell in the computations. In this process, it is necessary to let the neural network work on the front propagation and save what information it needs for later use. Hopfield networks are recurrent or fully interconnected neural networks. There are two versions of Hopfield neural networks: in the binary version all neurons are connected but there is no connection from a neuron to itself, and in the continuous case all connections including self-connections are allowed. Hopfield neural networks are applied to solve many optimization problems. In medical image processing, they are applied in the continuous mode to image restoration, and the binary mode to image segmentation and boundary detection.
- *Convolutional Neural Network* (CNN) is an architecture for deep learning, in the field of machine learning. Here, a model learns to perform tasks directly from images, text, video, or audio. Examples of deep learning are computational vision, natural language processing, and audio recognition. CNN may have tens or hundreds of layers that each learns to detect different features of an image. Filters are applied to training images at different resolutions, and the output of each convolved image is used as the input to the next layer [63]. The filters can start with simple features, such as brightness, contrast, and edge detection, and then with increasing complexity, they capture unique features of the object of interest [63]. After the learning process in many layers of the image features is completed, the architecture of a CNN is then ready for classification.
- *Modular Neural Networks*. This sort of network encompasses an assortment of different networks working independently and contributing to delivering an output. Each neural network presents distinctive input sets when compared to other networks constructing and performing other derated assignments. These networks do not interact or signal each other for the accomplishment of the assignments. The advantage of a modular neural network is that it breaks down an outsized procedure into smaller parts decreasing its complexity

ANN consists of many simple computational elements denominated artificial neurons, which are densely interconnected and operate in parallel. They are many possible neuron combinations and therefore many ANN architectures. **Figure 46** shows a typical arrangement of an artificial neuron, which converts a group of inputs into a single output after being processed by an activation function. These activations can derive from external variables or other artificial neurons.

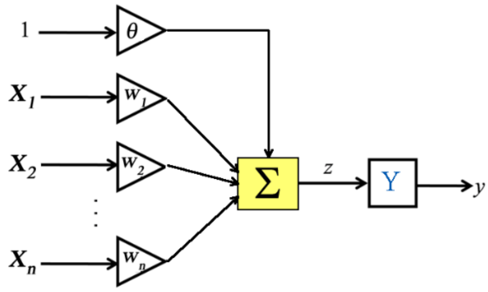

Figure 46: Artificial Neuron structure

Figure 47 shows an example of the application of an ANN to trace straight boundaries among four clusters of points, a classification problem, indeed. The neural network type perceptron of MATALB® was used in the code [64] [65]. The perceptron algorithm initializes all weights to zero and performs an iterative process for training using the cloud of points. It updates the weights only if the classification was wrong. The activation function *hardlim* (hard limit) was used, and the solution's convergence is very fast.

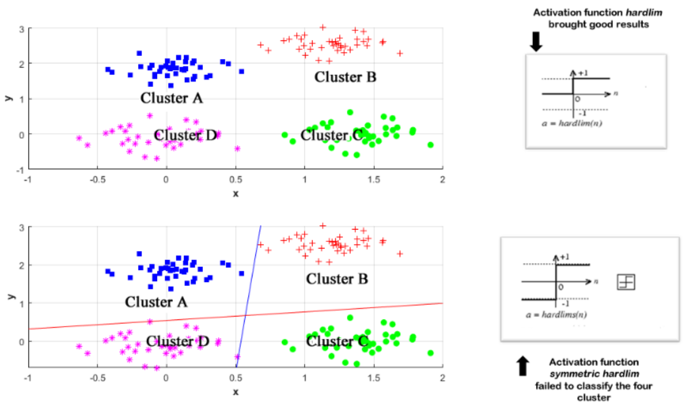

Figure 47: A simple cluster classification problem using an ANN

Another example of the application of the artificial neural network is the accurate representation of the following function, called here *Peaks*:

The shape of this function can be seen in **Figure 48**. It is characterized by a hill adjacent to a valley.

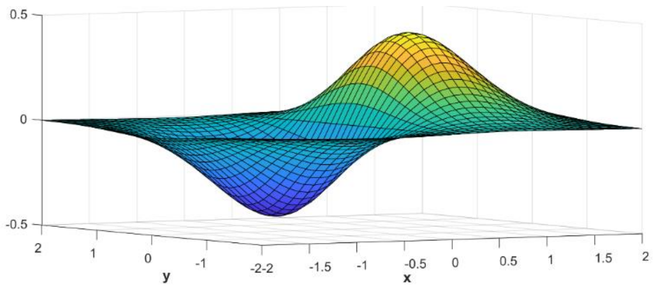

Figure 48: A graph of a function called here *Peaks*: $f_{peaks} = xe^{-x^2-y^2}$

Radial basis networks can be used to approximate functions. The MATLAB® command *newrb* adds neurons to a radial basis network's hidden layer until it meets the specified mean squared error goal [66]. A parameter called *spread* must also be provided to the *newrb* command. The larger *spread* is, the smoother the function approximation. Too large a *spread* means a lot of neurons are required to fit a fast-changing function. Too small a *spread* means many neurons are required to fit a smooth function, and the network might not generalize well [66]. It is recommended to use *newrb* with different *spreads* to find out the best value for a given problem.

Figure 49 shows the surrogate model of the *Peaks* function using the radial basis network of MATLAB®. The parameter spread was set to 1, the *goal* parameter received $1x10^{-7}$, and 1681 points were used for training and validation of the ANN model. The number of neurons that was adopted for this model is 20, but it is recommended to test a set of them to obtain an optimal representation of the *Peaks* function. **Figure 49** also contains a graph of the estimation errors by the ANN, and it can be observed that they are higher close to the boundaries determined by the set of points that were used for the training and validation. As homework, it is suggested to the experienced reader to carry out two optimizations with MALAB®: the first directly utilizing the *Peaks* function as objective; the second one should use the estimated ANN values for function estimation. It is a good test to verify whether the surrogate model can be used in optimizations or not.

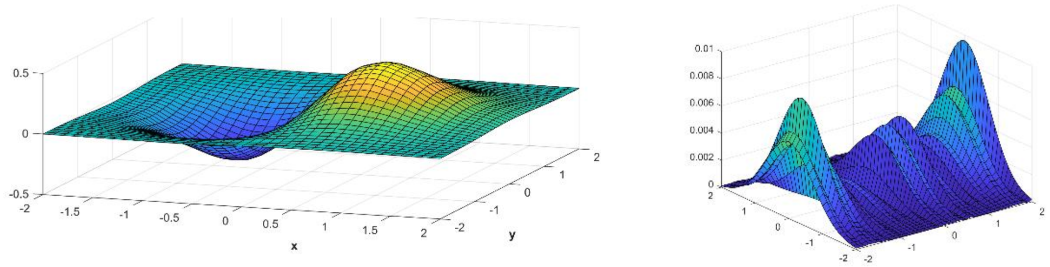

Figure 49: Peaks function as modeled by radial basis network and estimation errors

5.3 Extracting flight data from large databases

A. Improving mission profiles

Although the system-of-systems philosophy in aircraft design allows for tools for the inclusion of operational aspects during the optimization process, few existing design frameworks consider information about the actual aircraft mission profiles, their inherent constraints, and how they impact the airline economics. The increase of distance flown by a long-range aircraft when compared to a benchmark distance (Great Circle Distance), is often referred to as en-route inefficiency.

Figure 50 shows a route performed by a Boeing 777-300ER that flew from New York to Narita Airport in Japan in May 2020. The flight data were obtained from a flight tracking website [67]. Another route this time of a transatlantic flight is with a Boeing 747-8 in May 2020 [68] as illustrated in **Figure 51**. Taking off from São Paulo Guarulhos Airport the time spent to reach the initial cruise altitude was 23 min and 21 s (**Figure 52**). Two distinct marks for this flight are the step cruise and a speed overshoot at the beginning of the cruise phase. Although the Boeing 747-8 service ceiling is 43,100 ft, the maximum altitude this airplane flew in this long-range flight was 38,000 ft. For both flights, there is a considerable departure from the Great Circle trajectory.

Recent operational data have shown that depending on the region, en-route inefficiency may vary between 2 and 7 percent [69]. Such values are naturally associated with a proportional increase in fuel burn and emissions. Rios Cruz et al. [69] evaluated the consequences of such an increase in traveling distance in the design of a European airline network. Data data-driven mission profile definition was incorporated into an MDO framework for airplane conceptual design. Machine learning methods were applied to Automatic Dependent Surveillance-Broadcast (ADS-B) flight data considering ten major EU airports over six months. Thus, the definition of principal flight patterns was possible to feed an aircraft performance module whose output is the operational cost. A genetic algorithm optimizer is part of the design framework, which also contains an aircraft sizing module, a data-driven mission performance evaluator, and an embedded airline network optimizer. Altogether, the proposed algorithm aims to maximize the network profit. The results show that more conservative estimations in terms of profit and direct operational cost are achieved when accounting for realistic mission profiles.

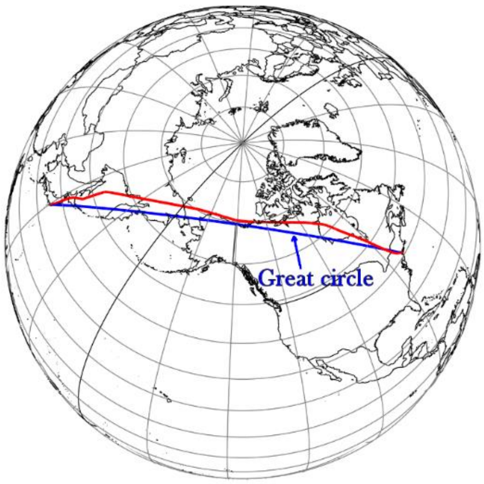

Figure 50: Three-dimensional view of the route from New York to Tokyo with a Boeing 777-300ER. Some data of the cruise phase are missing and were linearly interpolated

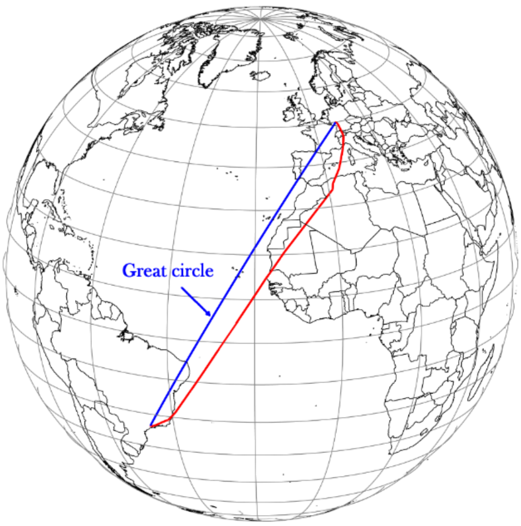

Figure 51: Three-dimensional view of the route from São Paulo to Frankfurt with a Boeing 747. Some data of the cruise phase are missing and were linearly interpolated

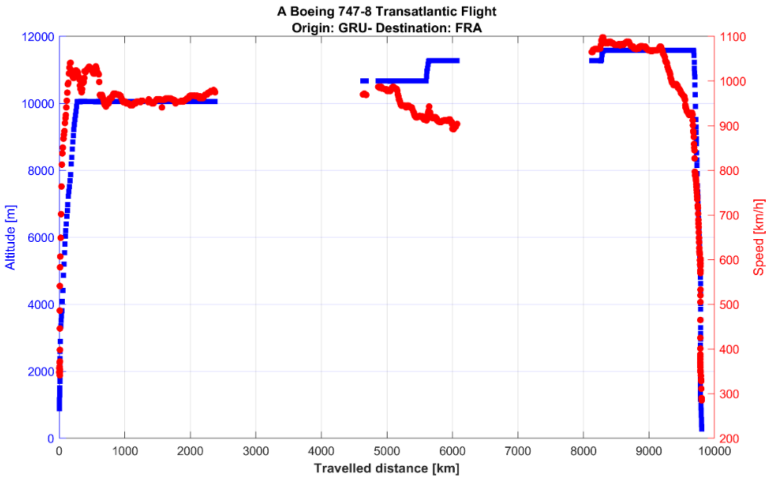

Figure 52: Flight profile of a flight GRU-FRA in May 2020. Ground speed and altitude are given as a function of traveled distance

To enhance the cluster detection performed by the DBSCAN algorithm [70] without losing flight information, a phase identification was added to the framework elaborated by Rios Cruz. This process employs the methodology elaborated by Sun et al [71], which applied fuzzy logic on the time series data following the theory from [72].

Fuzzy logic was applied to establish to which phase a certain point in the dataset pertains considering a set of membership functions to describe altitude, speed, and rate of climb, related to a certain flight phase. Four types of membership functions are used: Gaussian, Z-shaped, S-shaped, and Pi functions. Differently from [71], the *Pi* function was included to increase the accuracy in the cruise and level descent phase detection. Additionally, during the process of phase identification, it was observed that cruise phase detection is a function of the distance between airports. Because of that, the settings proposed by [71] for the definitions of high altitude, needed to be tuned for situations where the distance between airports was small than 200 nautical miles, considering a value of $H_{hi}(\eta)$ = G(η,30000,15000).

The membership functions related to the different characteristics of the flight stages are shown in **Figs. 53** to **55**. The x-axis represents the low and high extremes of each feature. Four membership functions were used for the altitude and RoC, and only three for the speed. This is justified considering that is expected that the same range of speeds takes place during the last part of the climb, the cruise, and the beginning of the descent phase.

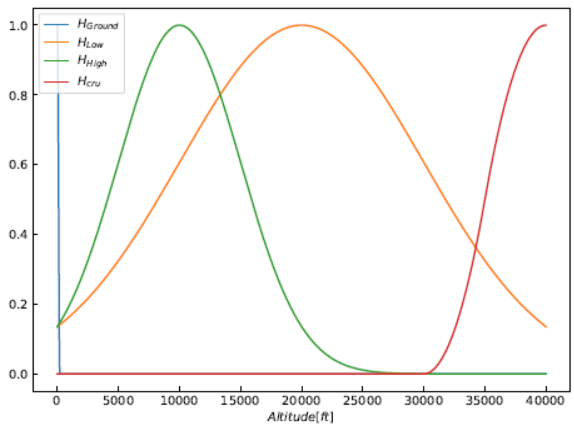

Figure 53:Altitude

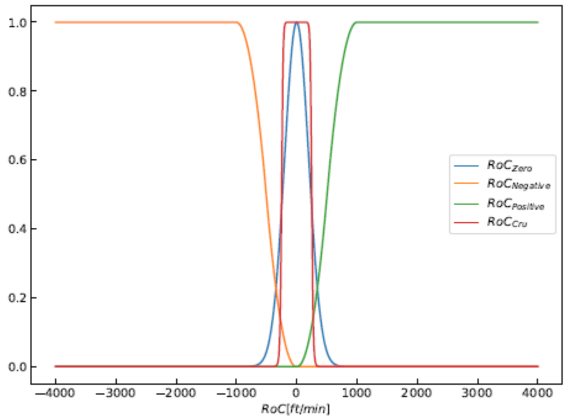

Figure 54: Rate of climb

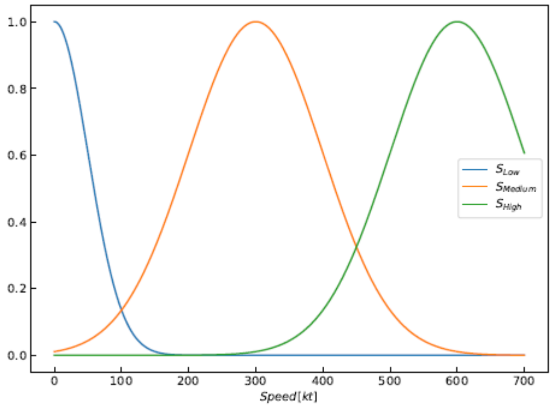

Figure 55: Speed

The following rules were used to identify the correct phase:

- if $Hgnd \wedge Vlo \wedge RoC0$ then Ground
- if $Hlo \wedge Vmid \wedge RoC+$ then Climb
- if $Hcr \wedge Vhi \wedge RoCcr$ then Cruise
- if $Hlo \wedge Vmid \wedge RoC-$ then Descent
- if $Hlo \wedge Hhi \wedge Vmid \wedge RoC0$ then Level flight

The fuzzy logic then uses this information for a given data point and all possible discrete flight phase states $P(0 \leq P_i \leq 6)$ (all represented by Gaussian functions). Finally, a defuzzification takes place, where the most likely flight phase state is found using **Eq. 66**.

$$\hat{P} = round(\arg \overset{max}{P} S(P)) \tag{66}$$

In **Eq. 66**, $\hat{P}$ represents the output where the highest combined fuzzy value occurs. The labels generated in this step ('GND', 'CL', 'CR', 'DE', 'LVL') are included in a column of the data frame to be used in the following steps.

To detect the main horizontal and vertical flight patterns, a two-step cluster approach followed the preceding procedure. Only the cruise information of the trajectories was used to measure the distance between them (input for the selected algorithm), envisioning the reduction of outliers. Considering this and due to the spatial nature of the dataset, the Density-Based Spatial Clustering of Applications with Noise (DBSCAN) algorithm was selected to perform the clustering task.

B. Estimating airliner mass from flight data

This is another good example of the use of inverse techniques. There have been several approaches to compute the mass at initial climb segments. These masses are used for fuel consumption calculation and trajectory prediction.

Bayesian inference has been used for the estimation of the mass of airliners from statistical flight data. Bayesian inference derives the posterior probability from two known data: a prior probability and a "likelihood function" derived from a statistical model for the observed data (**Figure 56**).

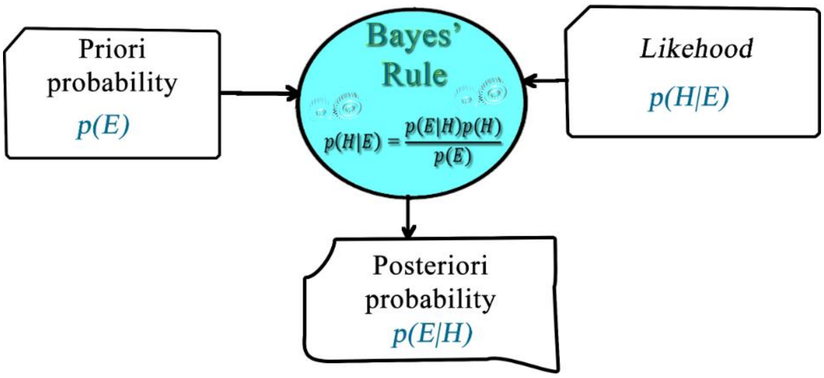

Figure 56: Illustration of application of Bayes' rule

After a study presented by Sun et al. [73], the estimation of the initial mass of airplanes not just at one specific flight phase, but a combination of all phases, derived an improvement of their methodology [74]. The mass estimation problem was considered as a single parameter for a Bayesian inference task, considering observational masses computed along with the entire flight. In addition to multiple observations, prior knowledge of weight was used to improve the estimation. Sun et al. used approximations to obtain the number of passengers, considering constraints for the variation of weight estimation according to the known payload for each airplane. The authors state that prior knowledge can be very valuable for the estimation of actual aircraft mass when applying Bayesian inference. Fuel consumption was modeled by using the ICAO aircraft engine emissions database, which is freely available. Using this data, the authors proposed a quadratic fuel flow model that is constructed setting the fuel flow as a function of the ratio between thrust at a given flight condition and maximum static thrust [74].

Silva [75] proposed three methods to estimate airliner takeoff mass from en-route climbing data, gathered from Automatic Detection Surveillance-Broadcast sources (ADS-B). The first method proposed by Silva is a deterministic one, consisting of the identification of flight procedures for climbing segments such as initial altitude for acceleration before the climb itself, and, for example, where the calibrated airspeed is constant. The second and the third approaches compute operational parameters directly from Automatic Detection Surveillance-Broadcast data and utilize them in each step for the performance calculation. Mass estimation process can be optionally carried out considering wind effects. Silva [75] made use of the BADA 3 performance model [76], calibrated with ADS-B data, and used a genetic algorithm for error minimization. The derivatives dV/dH and dV/dt (necessary for trajectory computations) are calculated from ADS-B data plots, providing more efficient results than on previous academic studies, which normally use the constant calibrated airspeed method.

The objective function utilized is summarized in **Eq. 67**.

$$Fobj = \left(\frac{1}{N} \sum_{i=1}^{Npoints} [(H_p)_{observed}(t_i) - (H_p)_{siml}(m, \delta_{red}, t_i)]^2 \right)^{0.5} \tag{67}$$

where:

- N represents the number of samples extracted from ADS-B at a specific time stamp t_i
- $(H_p)_{observed}$ is the observed altitude (from ADS-B string) at a specific time stamp t_i
- $(H_p)_{siml}$ is the simulated altitude, calculated via Aircraft Performance Model, related to the time stamp t_i.
- δ_{red} is a thrust setting coefficient.

Data from selected flights operated with A330-200 were employed to validate the three approaches employed for mass estimation. All flights departed from Medellin (Colombia) to Madrid (Spain). The methodology for mass estimation from an integrated simulation on several points along stable segments in the climb phase contributed to the good accuracy of the results. The simulations with and without wind models have shown equivalent results, with errors between 2% to 4% when compared with actual mass data for two of the approaches (**Table 6). S**ensitivity analyses by varying δ_{red} with altitude were performed. An improvement in mass estimation was recorded when compared with previous academic studies, which present errors ranging from 5% to 10% for masses at the initial climb phase.

Table 6: Estimated and actual masses for flights with A330 @ 11,500 ft [75]

Flight	Approach	F_{Obj} [m]	δ_{red}	Calculated mass [kg]	Actual mass [kg]	Error [kg]	Error [%]
1	dVdH	11.56 m	0.950	200,340	202,701	2361	<2%
	dVdt	14.54 m	0.989	208,192	202,701	5491	<4%
2	dVdH	26.54 m	0.942	204,205	206,420	2215	<2%
	dVdt	32.19 m	0.973	208,971	206,420	2551	<2%
3	dVdH	11.56 m	0.966	207,759	209,324	1564	<1.5%
	dVdt	14.54 m	0.966	213,495	209,324	4172	<2%

5.4 applications of multi-layer perceptron network

A. Multi-layer perceptron network

Multi-disciplinary airplane design frameworks, essential tools for today's aircraft design, require considerable computational power, and the computing cost grows when higher fidelity tools are used to model the associated disciplines. The use of surrogate models offers an efficient alternative to overcome this issue. In turn, artificial neural networks have been successfully used to generate auxiliary models in complex systems with many variables. In this context, the present work deals with the design and application of artificial neural networks to predict aerodynamic coefficients of transport airplanes with a high degree of accuracy. The neural networks are fed with calculations from computational fluid dynamic codes, and they can predict lift, pitch moment, and drag coefficients for wing-fuselage-winglet configurations of transport airplanes. The input parameters for the neural network control the wing planform, winglet geometry, fuselage geometric parameters, airfoil geometry, and flight condition. Airfoil geometry is modeled by attributing weights to 14 basic airfoils compounding a database. An aerodynamic database consisting of approximately 62,000 cases calculated with a full-potential code with computation of viscous effects is used for the neural network training, validation, and test. Networks with different numbers of neurons are evaluated and those with the lowest mean quadratic errors are selected.

A Multi-layer Perceptron (MLP) network consists of an input layer, several intermediate layers (to transform inputs into something that the output layer can use), and an output layer. Connecting several nodes in parallel and series, an MLP network is formed. The image shown in **Figure 57** reveals the schematic of a feedforward network, which consists of a layered structure with information flowing from the inputs to the outputs. The inputs are points or data collection that may differ in nature which receive structured information and repass them to the first layer containing neural (Perceptron) nodes. This first layer of functional nodes is known as the hidden layer because it is not targeted to inspect or control the output values on these nodes during the process of training when the network weights are obtained. The incorporation of hidden layers enables the network to model complex non-linear behavior [77] by using the usual transfer functions already mentioned before. The optimal number of hidden layers could be smaller than the number of inputs. Typically, just two hidden layers work fine with few data and a higher number of hidden layers can be fruitful for the difficult object. Several architectures must be evaluated and presented the lowest mean quadratic error should then be taken. The outputs that flew through the hidden layers are subsequently processed by an output layer and the results are compared to the known values associated with the input pattern.

Eq. 68 illustrates the simplicity of the calculation of output values for the two-hidden-layer network shown in **Figure 57** using the input set.

$$y_i = \emptyset\left(\sum_{j=1}^{3} w_{ji,2}\,\Upsilon\left(z_{j,1}\right) + \theta_{j,2}\right) = \emptyset\left(\sum_{j=1}^{3} w_{ji,2}\,\Upsilon\left(\sum_{k=1}^{K} w_{kj,1}x_K + \theta_{j,1}\right) + \theta_{j,2}\right) \qquad (68)$$

It is possible to generate a layer with neurons that share the same inputs. An artificial neural network is the juxtaposition of these layers. Several ANN architectures are described in recent literature. Among these architectures, the multi-layer feed-forward ANN is recommended for non-linear regression problems [78]. This type of network can approximate any function to any desired degree of accuracy, provided it has enough neurons [79]. When multi-layer feed-forward ANN is used in regression problems, the neurons of the last layer use linear transfer functions, as the output might be any real number. The neurons of other layers usually use the hyperbolic tangent transfer function.

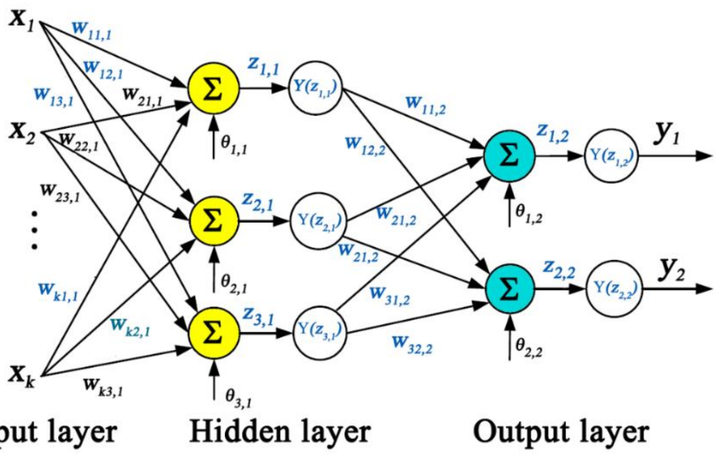

Figure 57: Exemplification of a multi-layer feed-forward network

All networks that were considered for the estimation of aerodynamic coefficients present two hidden layers. MATLAB® *fitnet* function fitting neural network [80] was employed in the present study. The *fitnet* is a specialized version of feedforward networks. The hyperbolic tangent sigmoid [81] was employed as transfer functions in the hidden layers. The network training function updates weight and bias values according to Levenberg-Marquardt optimization, also known as the Damping Least Square method [82] [83]. Like the quasi-Newton methods, the Levenberg-Marquardt algorithm was designed to approach second-order training speed without having to compute the Hessian matrix. The training/validation/test with the Levenberg-Marquart algorithm was fed with 57,000 cases. Training stops when any of these conditions occur [84]:

- The maximum number of epochs is reached.
- The maximum stipulated processing time is exceeded.
- Performance is minimized and reaches the goal.
- The performance gradient falls below a minimum value that was previously set.
- The damping factor exceeds the prescribed maximum value.

B. Forecasting oil price

Crude oil is a commodity found in geological formations below the Earth's surface, and at the bottom of the oceans. It can be refined into various kinds of consumer fuels and other substances, many of them finding applications in the petrochemical industry. Crude oil is amongst the most important energy resources on earth right now. So far, its derivatives remain the world's leading fuel, providing nearly one-third of the global energy consumption. In addition, this information is crucial to methodologies that elaborate the market outlook of transport aircraft [85]

To forecast the oil price precisely, a two-hidden-layer perceptron network was chosen to train and validate data from crude oil production, demand, and stocks. The activation functions for the first and second layers are tangent sigmoid and log sigmoid, respectively. The input variables and their respective sources of information are as follows:

- World oil demand [86].
- U.S. oil stocks [87].
- Total oil production [88] [89].

The output variable, or the variable to be forecasted, is the West Texas Intermediate (WTI) crude oil price [90].

Figure 58 shows the crude oil output from three different sources and **Figure 59** is a two-vertical axis graph containing the WTI crude oil price and demand over time. The available data were compiled and adjusted for the 1987-2019 period.

A set of networks comprising different combinations of several neurons into two hidden layers was evaluated. The number of neurons in the first hidden layer varied from 20 to 120. The second layer could then receive neurons starting from 20. The maximum number possible to attain depends on the number of neurons existing in the first layer.

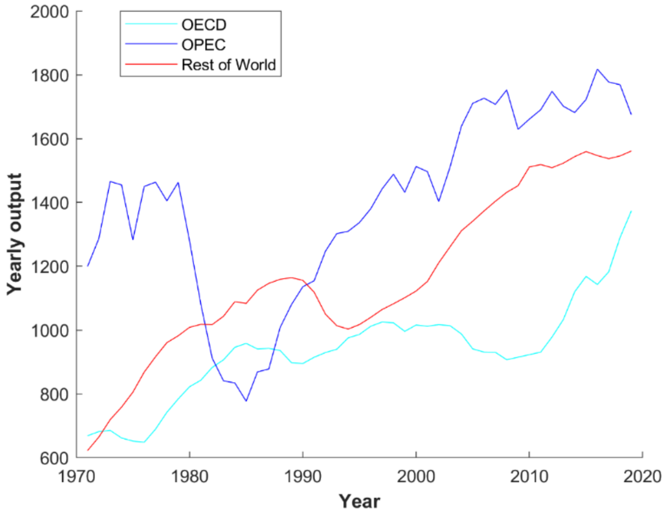

Figure 58: Crude oil yearly output

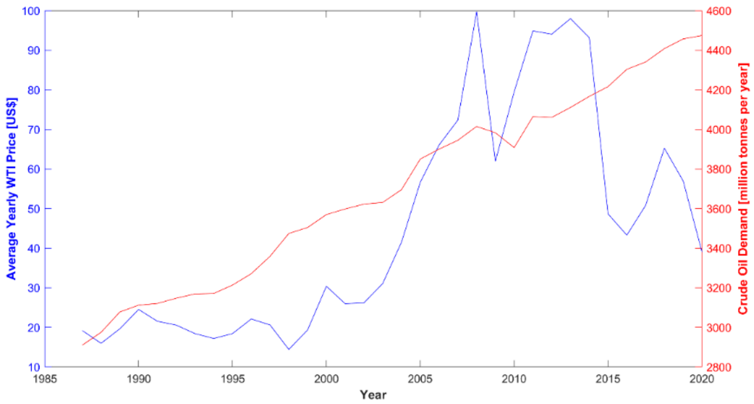

Figure 59: Average WTI crude oil price and demand

Ten years of the compiled data were normalized and thereafter separated for forecasting by ANN. The remaining data were then used for training and validation. The ANN with the lowest mean square error has 120 and 60 neurons in the first and second hidden layer, respectively. **Figure 60** compares the forecasted values by the selected ANN with actual data. The average error in the period analyzed was US$ 16.37.

Figure 60: Forecasted and actual crude oil prices for the 2012-2019 period

C. Estimating drag coefficients with a surrogate model

Here, a surrogate model with ANN to replace a full-potential code in airplane MDO frameworks is described and some results are presented. A database with almost 72,000 cases to train and design the ANNs was generated. The data robustness of the database was checked with the learning curves method. The 59 design variables were used for the surrogate model with neural networks. **Figure 61** shows some range and boundaries for some of them, whose distribution in design space was performed by a Latin hypercube Design of Experiment (DOE) algorithm. Some additional runs at higher Mach numbers were enforced because of the non-linear relationship among the design variables and the aerodynamic coefficients in this part of the design space.

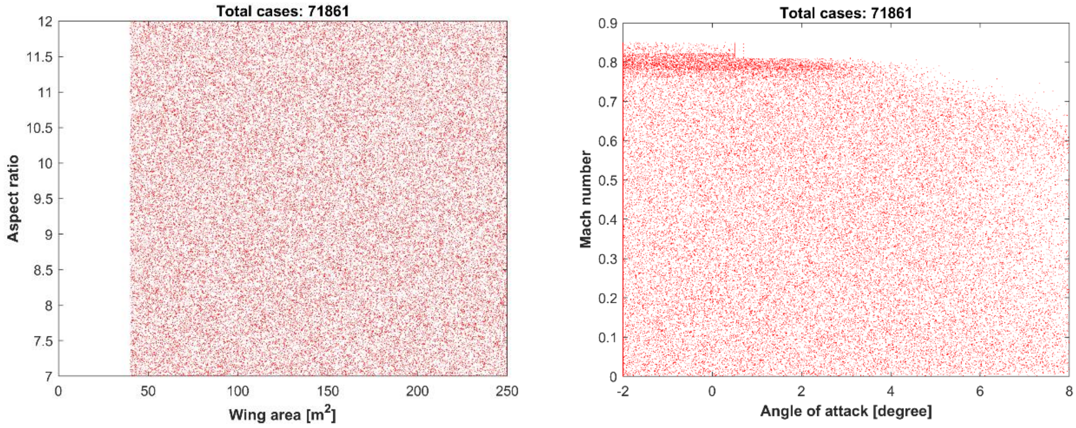

Figure 61: Some variables used for flow calculation with successful output. Notice the good coverage provided by a Latin hypercube DOE.

All training validation and testing of candidate networks ran on a desktop computer fitted with an Intel® Core™ i9-9900K CPU @ 3.60 GHz clock. **Figure 62** displays the main panel of the training/validation/test process for the 120x120 network. The process for this network took over 39 h of computing time.

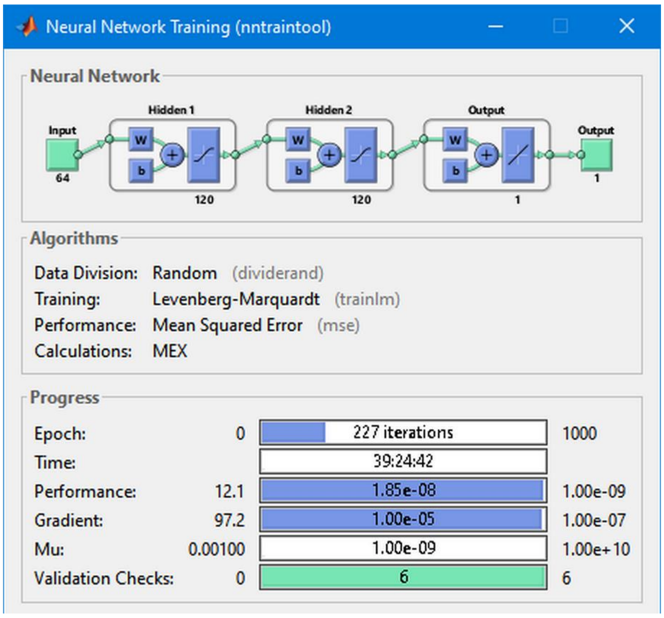

Figure 62: A main panel of the training/validation/test process with MATLAB® for the 120x120 network targeted to estimate the pitching moment coefficient

The airplane with ID 165218 (**Figure 63**) was chosen to verify the capability and accuracy of drag coefficient prediction of the neural network system that was developed in the present work. This configuration was not used in the training/validation/test procedure. The features of this configuration are provided in **Table 7**. **Figs. 64** to **68** show a comparison among results from the surrogate ANN model and calculations performed with the full potential code at the same flow condition.

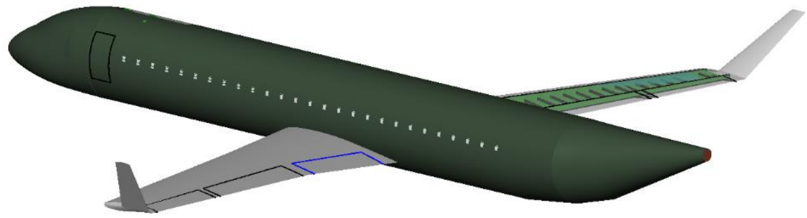

Figure 63: Configuration with ID 156218

Table 7: Data for the ID 156218 configuration

Wing aspect ratio	10.85
Wing taper ratio	0.433
Location of the wing break station	43% of semispan
Dihedral angle	2.60º
Root incidence angle	2.83º
Incidence of the break station	1.08º
Incidence of the tip station	-4.00º
Wing area	133.88 m^2
Quarter-chord sweepback angle	16.19º
Winglet aspect ratio	2.81
Winglet taper ratio	0.493
Winglet sweepback angle	30.04º
Winglet dihedral angle	48.20º
Winglet twist angle	-2.36º
Fuselage length	38.90 m
Fuselage width	3.331 m
Fuselage height	3.642 m
Fuselage wetted area	367.76 m^2

Figure 64 shows the comparison between the results for the lift coefficient at several numbers of Mach. All flow conditions were considered at a one-degree angle of attack and 13,000 m flight altitude. The Reynolds number with the wing MAC as reference length varies with the Mach number. The agreement between the CFD code and the surrogate model is excellent with errors lower than a fraction of one drag count, even at higher Mach numbers where strong shock waves are present.

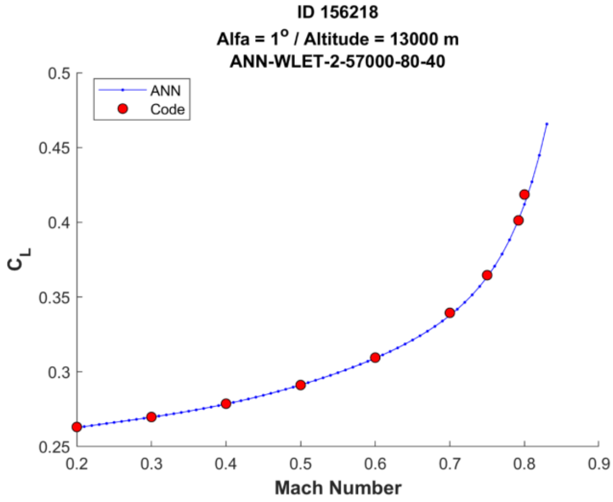

Figure 64: Comparison between lift coefficient estimation for airplane 156218 by the chosen ANN and those calculated with the full potential code

Figure 65 and **Figure 66** show graphs that compare calculations carried out by the full potential code with predictions from the surrogate models for Mach numbers varying from 0.20 to 0.83. The vertical scale of graphs was set in drag counts - one drag count corresponds to a drag coefficient of 1x10^{-4} - to facilitate readings. Only for reference purposes, the green symbols in both graphs are relative to the configuration with ID 156218 with no winglets. The winglet increased the configuration drag but the comparison shall be made at the same lift coefficient when its benefit regarding lower drag will emerge.

Figure 65 reveals that there is an exceptionally good agreement for the C_{D0} between the values estimated by ANN of size 100x60 and the results from the CFD code. According to **Figure 66**, the same is valid for the estimation of the induced drag, C_{DI}, with those from the chosen ANN of size 100x100. In both curves, the difference between the CFD code and the ANN lies below one drag count except for the Mach number of 0.80, where the discrepancy increased approximately to two drag counts. However, this is a region of drag divergence and this difference can be considered negligible and the capacity of the ANN system to predict viscous and induced drag coefficients is outstanding.

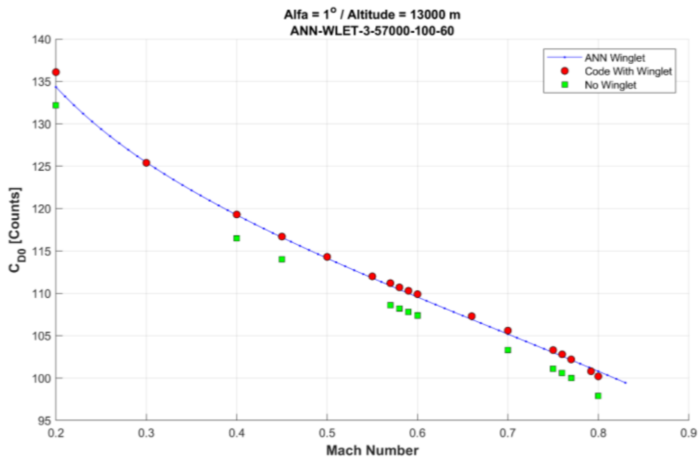

Figure 65: Comparison of zero-lift drag coefficient for airplane 156218 between ANN and those calculated by the full potential code

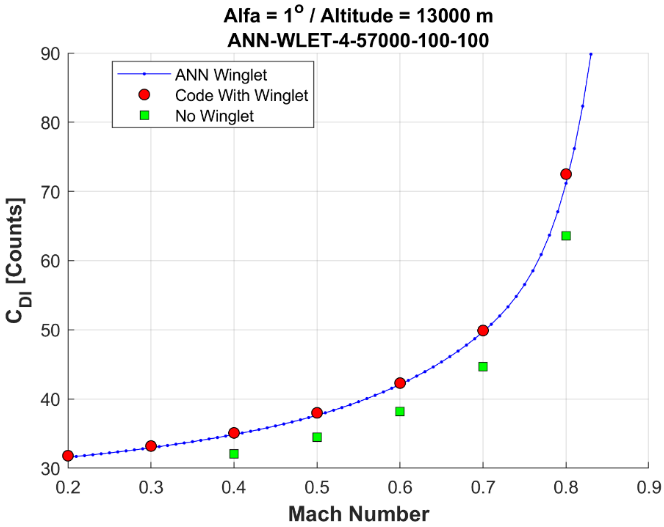

Figure 66: Induced drag coefficient for airplane 156218 at α=1° at an altitude of 13,000 m

Figure 67 and **Figure 68** show graphs that compare calculations carried out by the full potential code with predictions from the surrogate models for the wave drag, C_{DW}, and the wing pitching moment coefficient, C_M. **Figure 67** reveals that there is a good agreement for the C_{DW} between the values estimated by the dedicated ANN of size 100x100 and the results from the CFD code. The main difference between calculated and predicted values is in the order of four drag counts, taking place at curve foothills. **Figure 68** reveals an excellent agreement between the calculated and predicted C_M. The graph at left, the variation of pitching moment with the angle of attack, meaning that the slope, which corresponds to $C_{M\alpha}$, is constant as expected for a subsonic flow condition.

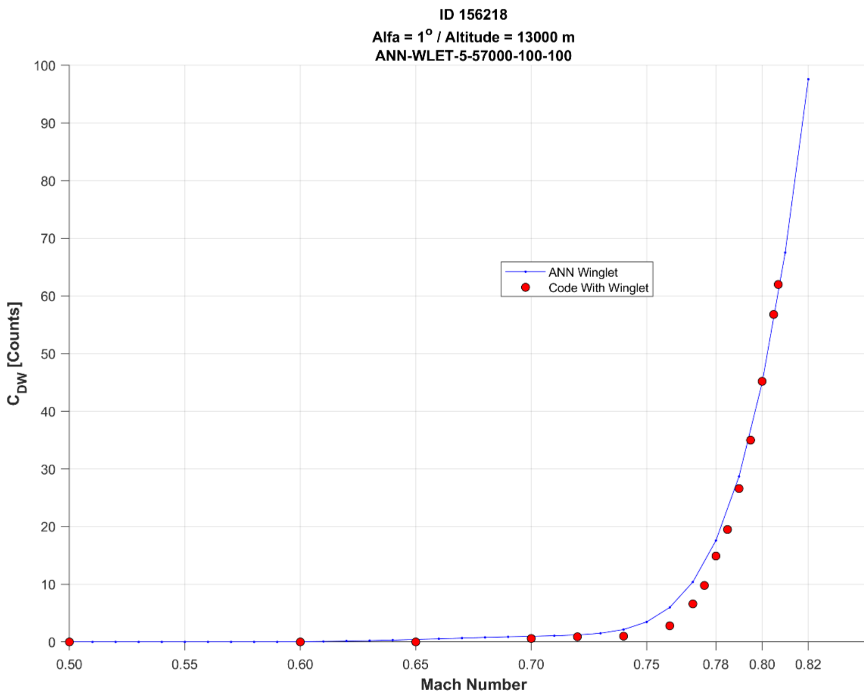

Figure 67: Comparison between wave drag coefficient estimation for airplane 156218 by the 100x100 ANN and that calculated by the full potential code

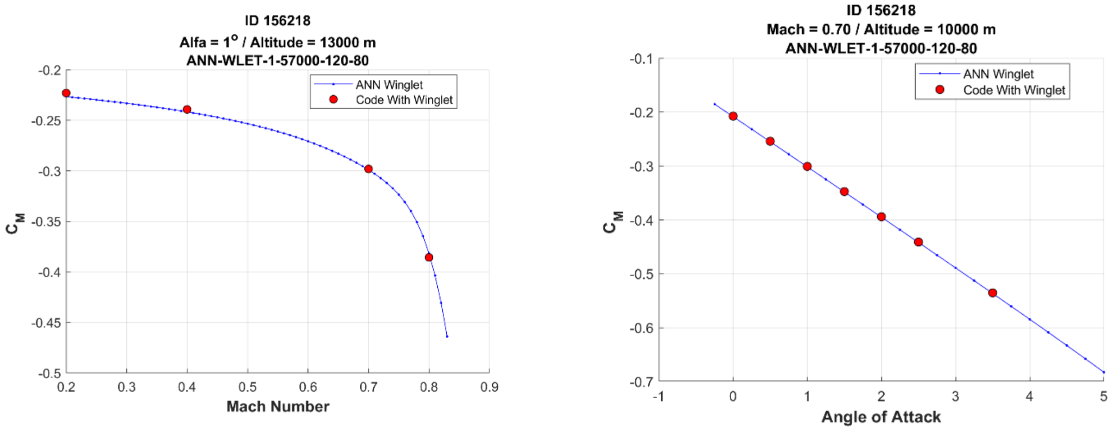

Figure 68: Comparison of pitch moment coefficient estimation for ID 156218 by the chosen ANN and that calculated by the full potential code. At left, variation with Mach number at a constant angle of attack; at right, variation with angle of attack at a Mach number of 0.70 and altitude of 10,000 m

To illustrate the utilization of the ANN surrogate model, an aerodynamic optimization of an airplane similar in capacity to the B757-200 was carried out. This is our baseline or reference airplane, and it is designated here BF-200LR. A top view of both airplanes is provided in **Figure 69**. Basic data for BF-200LR is given in **Table 8**.

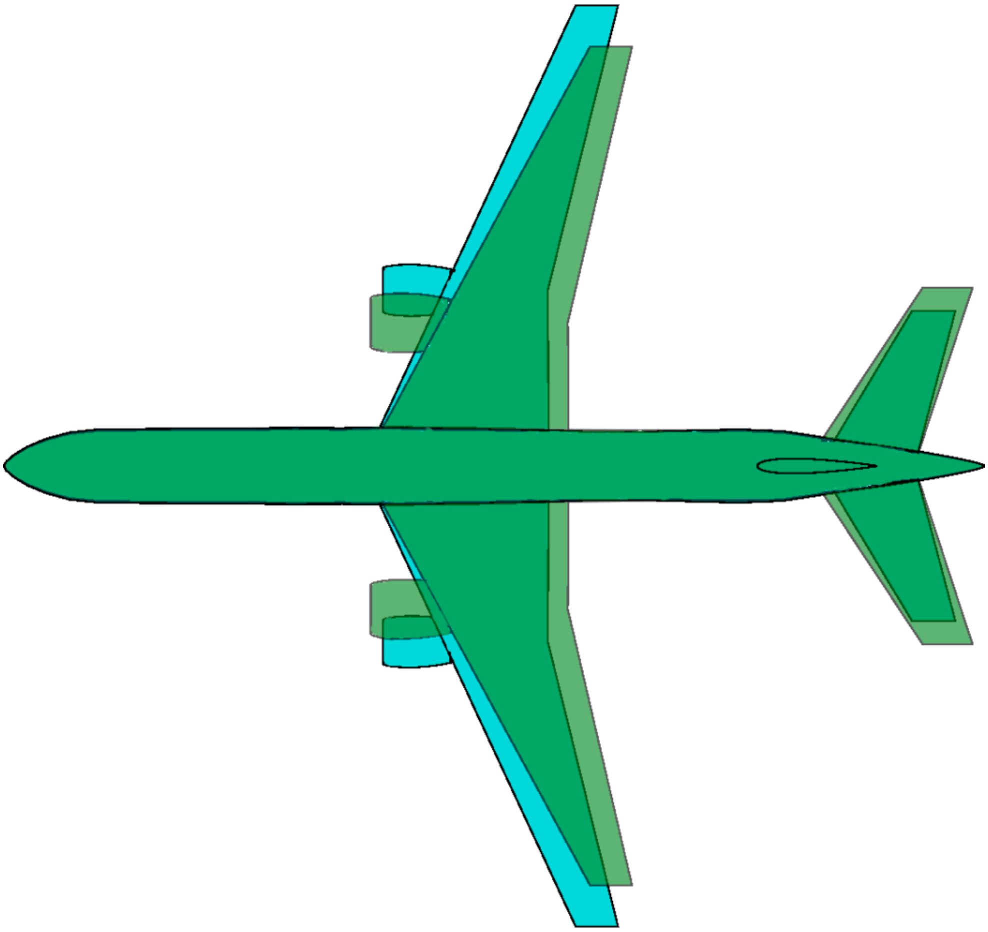

Figure 69: B757-200 and BF-200LR top-view juxtaposition for comparison purposes

Table 8: Basic data for BF-200LR

Wing Aspect ratio	Wing area	Wing sweep	Overall thrust	Engine BPR	Engine diameter	Two-class Accommodation @ 32-inch pitch in Y-class	Design range
9.97	175.35 m^2	22.29°	285.6 kN	6.00:1	1.93 m	192	3,420 nm
MTOW		**OEW**		**MMO**	**Fuel capacity**		**Range**
100,111 kg		53,573 kg		0.81	30,924 kg		3,470 nm$^{\alpha}$
α @ FL370 and FL390, Mach number of 0.80, payload of 19,200 kg, ISA+0 °C, takeoff with MTOW, 200 nm to an alternate, 30 min loiter @ 1,500 ft							

This additional study was intended to design the break- and tip-station airfoils, jointly to find out the optimal wing twist angle, and the incidence of the break station for a set of objectives and constraints.

Airfoil geometry impacts enormously the maximum lift coefficient. According to Ref. [91], the C_{Lmax} at landing for the B757-200 is 2.38, considerably lower than that of its computational representation airplane considered here, which presents a value of 3.06 for this coefficient. This is due to the different wing airfoil geometries that compose the actual airplane and its counterpart of the present work. There is no information available about the B757-200 airfoils and that utilized here are transonic airfoils that intend to match the maximum relative thickness of them as close as possible. On the other hand, the MMO of B757-200 is 0.86 [91], relatively high considering the moderate sweepback angle of its wing. Despite the typical mission established for the B757 was to fly domestic routes in the United States, even for medium populated cities, the North American manufacturer preferred a configuration with higher speed, which certainly worse field performance. In general, airfoils presenting good transonic characteristics like higher divergence Mach number tend to reveal some degradation of field performance. Thus, an optimization with these two conflicting objectives may produce interesting results.

The optimization task that was then carried out included two objectives:

- the maximum value of the Mach x Lift/Drag (MLD) in the 0.70-0.85 Mach number range,
- and the maximum lift coefficient at landing configuration.

The constraints for this problem are:

- the maximum relative thickness of break-station airfoil must be greater than that of tip-station airfoil.
- The maximum relative thickness of the root-station airfoil must be greater than that of the break-station airfoil.
- MMO must be higher than 0.80.
- Fuel capacity greater than 30,000 kg.
- C_{Lmax} @ landing must be higher than 2.5.
- Drag rise to MMO lower than 20 counts.

The aerodynamic coefficients at the transonic regime for this simulation were calculated by an ANN system with 64 input variables for wing-fuselage-winglet combinations [92] and the remaining aircraft components a Class-II approach was employed. The airfoils were generated by 14 weights applied to the geometry of 14 airfoil geometries composing a database. Thus, 42 input variables are necessary to define the geometry of three basic wing stations, root, break, and tip. The clean-wing maximum lift coefficient is calculated by a full-potential code in combination with a 2D panel code by the critical section method [93]. Utilizing this information and additional configuration characteristics, the Datcom method [94] is then employed for the estimation of the C_{Lmax} coefficients at landing and takeoff configurations.

The simulation for airfoil optimization was stooped after 20 generations with 1200 individuals being analyzed. The multi-objective *gamultiobj* genetic algorithm of MATLAB® was employed in all simulations that were carried out here [95]. **Figure 70** shows the Pareto front and the characteristics of feasible and unfeasible individuals that arose in the simulation. A considerable improvement of MLD for the reference airplane was obtained, the same cannot be said for the C_{Lmax}. **Figure 71** compares the original and optimized airfoils that resulted from the optimization run.

Table 9 shows the characteristics of a selected individual from the Pareto front. MMO of 0.82 was obtained with the utilization of the surrogate ANN system considering a lift coefficient of 0.50. The aircraft module of the present design framework calculated the MTOW based on the same mission as that for the BF-200LR of maximum takeoff thrust, and a value of 97,841 kg was obtained. This is considerably lower than that shown in Table XI, of our reference airplane. However, this be only credited to the new airfoils, because MMO was increased from 0.81 to 0.82. A lower MMO means lower structural loads, and this will lead to a lower OEW. In addition, an aircraft with a similar mission of B757-200 when fitted with new, high by-pass engines, higher aspect ratio wings, and optimized airfoils, recorded a 17-t decrease in MTOW.

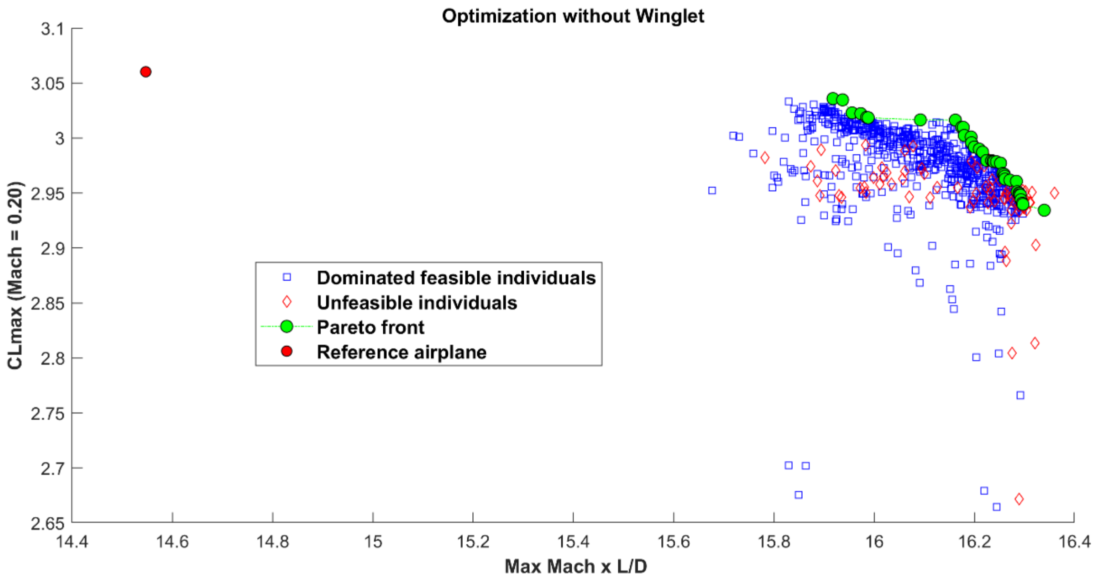

Figure 70: Optimization of wing airfoil geometry for a B757-200 similar aircraft

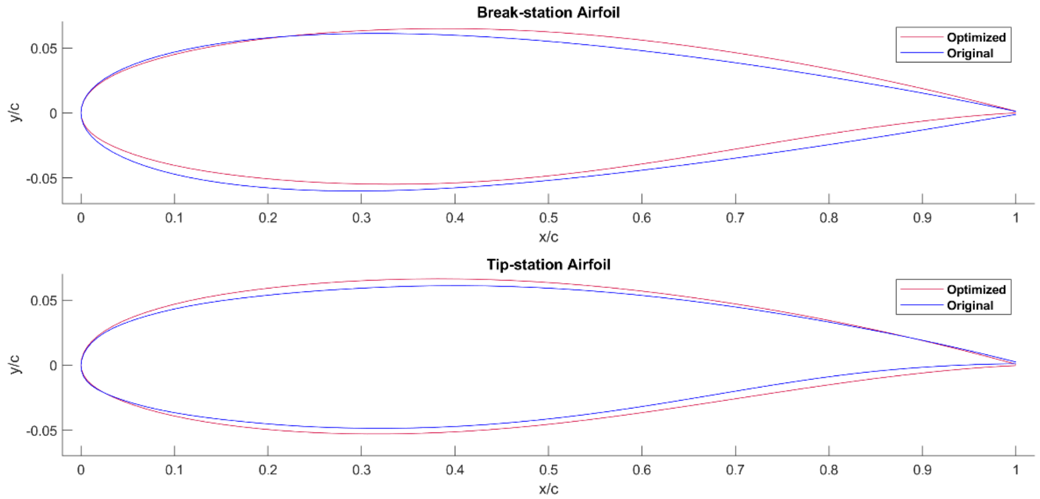

Figure 71: Break- and tip-station airfoils of the selected airplane optimal configuration

Table 9: Optimization of wing airfoils of BF-200LR

Parameter	Value
Max. MLD	16.21
C_{Lmax} landing configuration (Flap 40º)	2.987
C_{Lmax} clean wing	1.59
MMO	0.82
Fuel capacity	31,287 kg
Max. relative thickness of root airfoil	15.1%
Max. relative thickness of the break-station airfoil	12.0%
Max. relative thickness of tip airfoil	11,9%
Wing twist angle	-3.74º
Incidence of wing break station	0.276º
MTOW	97,841 kg
OEW	52,854 kg
ΔMTOW$^{\alpha}$	-2,270 kg
ΔOEW	-719 kg

α @ FL370 and FL390, Range of 3,470 nm @ Mach number of 0.80, payload of 19,200 kg, ISA+0 ºC, takeoff at MTOW, 200 nm to an alternate, 30 min loiter @ 1,500 ft

D. Optimization with prescribed pressure coefficient distributions

An optimization task was carried out for the design of a 90-seat airliner wing. Two objectives were considered: the first one is the maximization of $M\,{}^{L}\!/_{D}$; the remained objective was the minimization of the square error of the difference between the calculated Cp distributions and the prescribed ones at six stations along wingspan ($M_\infty = 0.78, \alpha = 1.8^o$). An airfoil database consisting of 21 geometries was used to build up the root, break, and tip station airfoils. The airfoils belonging to this database vary from NACA airfoils to supercritical ones from NASA e RAE (Royal Aeronautical Establishment). A fixed wing area of 92.29 m^2 was adopted for the airplane configuration considered in the present optimization task. The design variables are as follows:

- Wing quarter-chord sweepback angle
- Wing twist
- Incidence of the break station
- Wing aspect ratio
- Wing taper ratio
- Location of the break station (fraction of semispan)
- Root airfoil geometry (defined by 21 weights)
- Break-station airfoil geometry (defined by 21 weights)
- Tip airfoil geometry (defined by 21 weights)

Two constraints were set:

- Clean wing $C_{L,max}$ higher than 1.65
- Wing fuel storage capacity greater than 8600 kg

The $C_{L,max}$ is calculated according to the critical section method [93] by a combination of a full potential code and the XFOIL panel code [96]. The aerodynamic coefficients were calculated with the ANN developed by Secco and Mattos [97]. The divergence Mach number ($MachDiv$) is computed when the drag coefficient increases 20 drag counts above the subsonic value considering a constant wing-body lift coefficient of 0.45. The maximum $M\,{}^{L}\!/_{D}$ is then obtained in the Mach number range of 0.65-*MachDiv*. The multi-objective *gamultiobj* genetic algorithm of MATLAB® was employed in all simulations that were carried out here [95].

Figure 72 shows the Pareto front composed of four configurations and the individuals that surfaced during just ten generations of the optimization task. The optimal configuration with the lowest $M\,{}^{L}\!/_{D}$ presents the better agreement with the prescribed Cp distributions (**Figure 73**). The divergence Mach number of this configuration is 0.786, which is slightly above the Mach number of the prescribed distributions ($M_\infty = 0.78$). This is a good result, but it may be not enough to guarantee that off-design undesired behavior arises. Considering that the computation of aerodynamic coefficients has become very fast with the utilization of ANNs, is highly recommendable to set up constraints for the divergence Mach number, in addition to those two already employed here. The divergence Mach number should be higher than the Mach number where the Cp distributions are prescribed. This constraint must also encompass not just one but some lift coefficients.

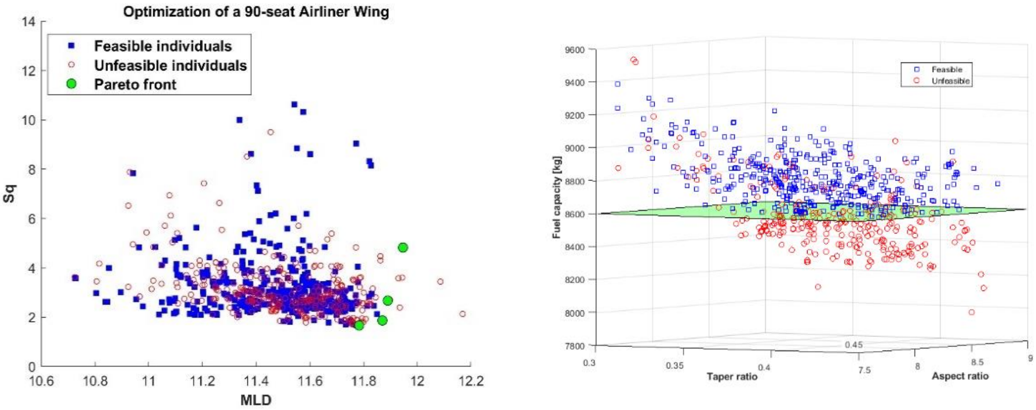

Figure 72: Simulation for the wing design of a 90-seat airliner. *Sq* is the square error that resulted after computing the difference between the prescribed and calculated *Cp* distributions at six stations along the wingspan

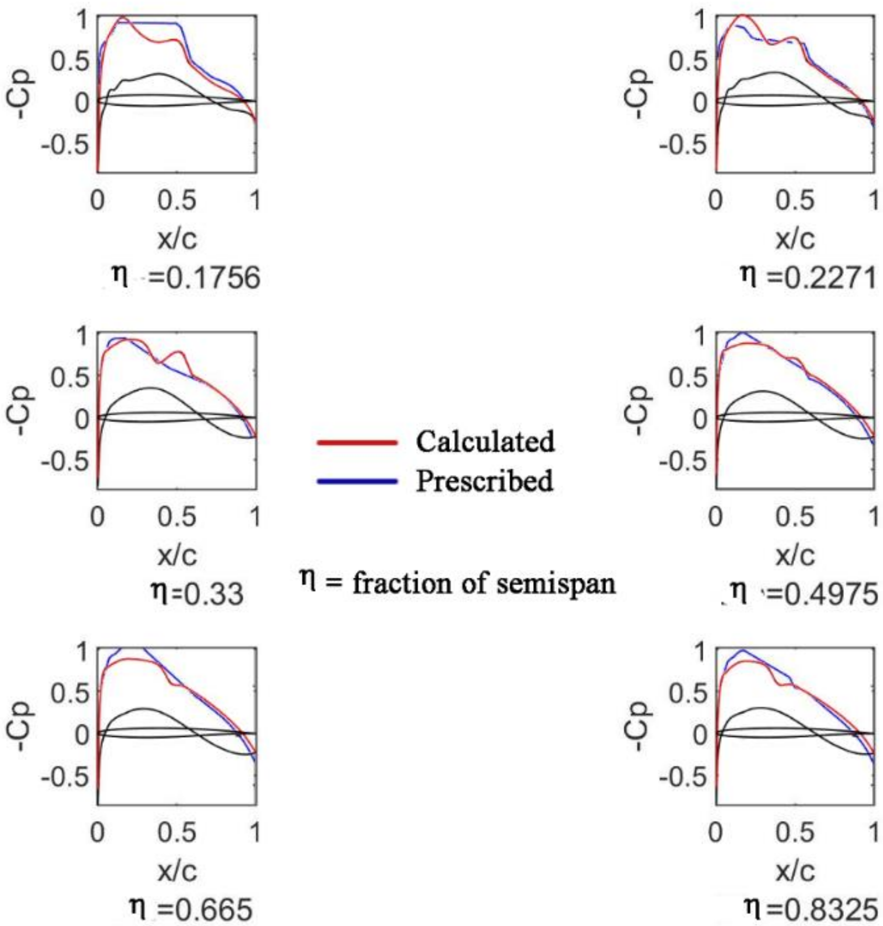

Figure 73: Prescribed and calculated Cp distributions for the optimal configuration with the lowest $M^{L}/_{D}$

6. Flutter Constraints into Conceptual Design of Transport Airplane

6.1 Introduction

Long-haul jet airliners usually present high aspect ratio wings because they perform the cruise phase at the highest possible $M \times L/D$. This is achieved at Mach number lower than the maximum operational one, meaning that the lift coefficients are moderately higher during a large part of the cruise phase and, naturally, during the climb phase. The induced drag coefficient is proportional to the square of the lift coefficient and the inverse of the aspect ratio. Besides a weight penalty, increasing the wing aspect ratio will lead to many adverse effects such as tip stall, lower flutter speed, and pitch up, the latter resulting from the combination of high aspect ratio wing with higher sweep angles. The increase in aspect ratio has a two-sided effect on induced drag because Oswald's factor [98] is playing an important role, as well. There is an additional increase in this drag component that is caused by the loading increase at the outboard wing, which can be mitigated by a combination of wing twist with chord distribution along the wingspan.

The flutter of a lifting surface involves the interaction of flexural and torsional motions. Separately, neither motion may cause flutter, but when considered conjunctly, at critical values of amplitude and phase angle, the forces produced by one motion excite the other; the two types of motion are then said to be *coupled* [22]. Inertial, aerodynamic, and elastic are usual sources of coupling. However, modern aircraft configurations with vortex-dominated flows may involve contained regions of separated flow, unsteady phenomena comprising of separation and subsequent flow reattachment, stalling conditions, besides various time-lag effects between the aerodynamic forces and the motion [99].

Even the addition of winglets must be carefully managed for preventing the appearance of flutter in the flight envelope. The transformation of the Boeing 737-800 airliner into the Boeing Business Jet (BBJ) involved the addition of winglets and for this reason, each wing received 75 lb of concentrated mass to mitigate flutter [100]. The quest for a more efficient aircraft has bumped into the limits of the aluminum-built cantilever wing configuration. Therefore, many approaches have been adopted for new possibilities to mitigate flutter for high-aspect-ratio wings such as the Truss-Braced Wing concept [101] or extremely flexible composite wings [102]. Another possibility is the increase in wing aspect ratio, which enables a reduction in induced drag. However, as mentioned before, cantilever wings of a higher aspect ratio are more likely to have flutter problems. Therefore, studies involving the flutter phenomenon become an even more relevant design consideration for new aircraft concepts and require those constraints to be included in the design as early as possible, preferably at the conceptual design stage. This way, costly changes are avoided at later stages of the aircraft development program.

Problems with torsional divergence affected aircraft in the First World War. They were solved by trial-and-error and stiffening of the wing without carrying for broader implications [103]. The first recorded and documented case of flutter in an aircraft occurred to a Handley Page O/400 English bomber during a flight in 1916 [103]. The airplane suffered a violent tail oscillation that led to an extreme distortion of the rear fuselage and the elevators to move asymmetrically [103]. Although the aircraft landed without injuries and fatalities, in the subsequent investigation some recommendations stated that left and right elevators should be rigidly connected by a stiff shaft. These recommendations subsequently became a design requirement. In addition, the National Physical Laboratory (NPL) was required to investigate the phenomenon theoretically.

The first formal flutter test was carried out by von Schlippe in 1935 in Germany [103]. The test aircraft was submitted to vibration at resonant frequencies at progressively higher speeds. Schlippe plotted amplitude as a function of airspeed and a rise in amplitude would suggest reduced damping with flutter occurring at the asymptote of theoretically infinite amplitude. This idea was applied successfully to several German aircraft until a Junkers Ju 90 military transport suffered flutter and crashed during a flight test in 1938 [103].

The distribution of heavy mass items in the wing can be optimized for flutter prevention. Wing structural design is driven by both strength and stiffness criteria. For example, if the torsion carrying structure of a wing is designed by a stiffness requirement, the wing would probably consist of a structure that carries its normal stresses in the wing skin with a minimum of stringers and flanges. This type of wing structure would require several spanwise webs to stabilize the heavily loaded skin. For a wing designed initially by strength criteria to withstand a specked load factor, it is straightforward that a higher torsional stiffness and hence a higher flutter speed will result if the ratio of stiffener area to skin area is reduced to a minimum. In addition, the use of higher strength alloys, which have no corresponding increase in modulus of elasticity, tends to make flutter more critical for wings designed for strength only. Wing aspect ratio should be treated as a design variable and not as objective as stated in Ref. [104]. Beyond certain limits of this design variable, flutter can no longer be avoided by mass distribution in the wing or by the addition of ballast. For non-linear systems, some design considerations were outlined in the first Section of this Chapter.

In the work of Opgenoord [105], the influence of aeroelasticity was investigated during the conceptual design of a transport aircraft by using a multi-disciplinary optimization tool. His article described an airfoil flutter model based on low-order physics. The flutter model handles the smallest vorticity moments of the flowfield and the volume source density perturbations. The model is calibrated using unstable 2D transonic CFD simulations. The resulting aeroelastic system combines the calibrated aerodynamic model with a beam model. The low computational cost of the model allows its incorporation into a conceptual design tool for state-of-the-art transport aircraft. The results presented in that work showed that the inclusion of flutter restrictions in the optimization of the aircraft design limits the wing aspect ratio, resulting in higher fuel consumption. Therefore, it was concluded that flutter limits performance gains obtained by using more advanced materials in the wing.

Jonsson et al. presented a review of the methods of development, implementation, and application of flutter and post-flutter constraints in the optimization of aircraft designs [106]. Furthermore, discussions about additional requirements associated with this type of project optimization, such as acceptable computational cost, smoothness of function, robustness, and derivative calculus, were introduced. In its conclusion, a summary of the current state of this field and the main open problems were presented.

A comparative sensitivity study for aeroelastic instability of aircraft wings in subsonic flow was carried out by Berci [107], which used analytical models and numerical tools with different multi-disciplinary approaches. His analyses were based on previous works and covered parametric variations of aero-structural properties, quantifying their effect on the aeroelastic stability frontier. Considering various degrees of fidelity both theoretical and computational calculations were evaluated, for possible practical applications in the preliminary design and optimization of aircraft. The results presented in that comparative study recommend the use of a hybrid strategy for the analyses, in which the flutter limit is obtained using a high-fidelity approach, while flutter sensitivity is calculated using a low fidelity approach.

The present work investigates the impact of flutter speed constraints in the configuration of a transport airplane. The package NeoCASS [108], a sophisticated suite developed for aircraft structural sizing and flutter speed calculation, was integrated into an existing MDO platform for aircraft conceptual design [109]. Two simulations tasks were carried out, one incorporating the flutter constraint and the other not. The results were analyzed and are discussed here.

6.2 Aircraft Conceptual Design Framework

A. Multi-disciplinary design framework

A MATLAB-based aircraft conceptual design framework for conceptual airliner design was developed at ITA over the years counting on contributions from several masters and doctoral thesis [109] [49] [110] [97] [111]. This framework is composed of several modules, which can handle and integrate aeronautical disciplines, manage airplane configuration, and control the optimization process. In addition, this MDO tool can calculate airplane noise signature at ICAO reference points [49], estimate engine emissions [49], and can be coupled with unsupervised learning algorithms to provide airplane classification, [112].

The workflow of the airplane design framework of the present work is shown in **Figure 74**. There are many possibilities in terms of fidelity of the discipline modeling that is used for airplane sizing. For example, lift-drag characteristics can be calculated from simpler models like Class-I formulations to CFD codes, or even by surrogate ANN models [97]. NeoCASS can be considered a medium-fidelity structural and aeroelasticity tool and will be described in detail in a dedicated section of the present study, as well as the multi-objective genetic algorithms were chosen to perform the optimization tasks.

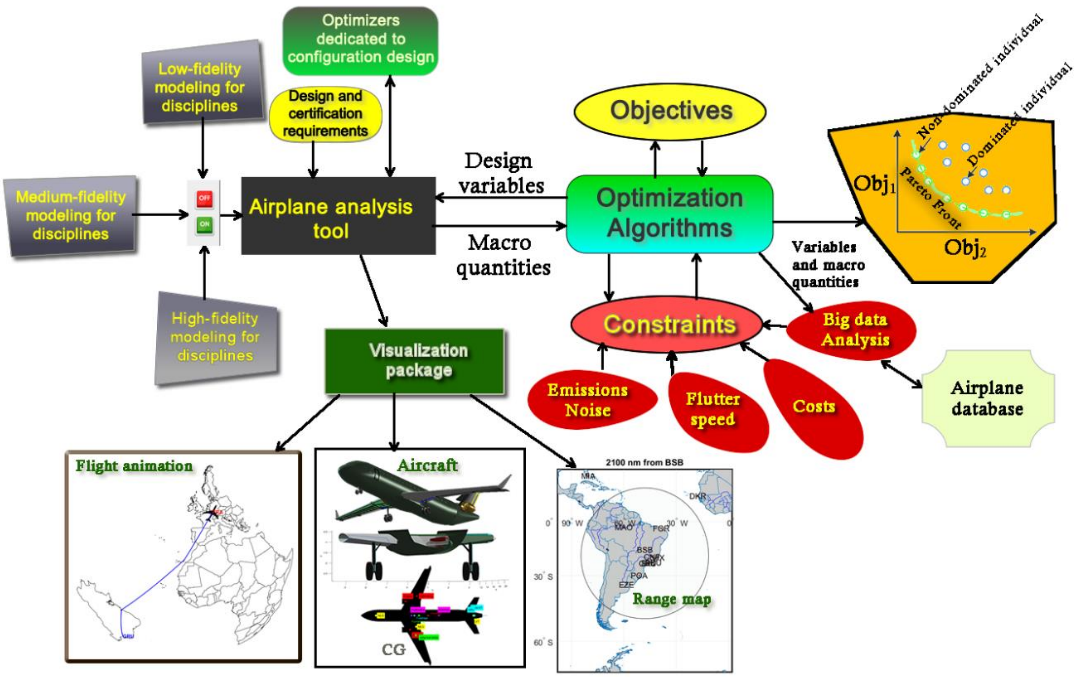

Figure 74: Overview of the present MDO platform

Important design requirements must be considered because they will generate a feasible airplane configuration when satisfied. Certification requirements such as climb gradient in the 2nd segment, cruise and missed approach thrust requirements, rate of climb at service ceiling, and balanced takeoff field length are some of them.

The multi-objective *gamultiobj* algorithm from MATLAB® was employed in all simulations that were carried out in this Section [95]. Two objectives were considered here: direct operating cost per nautical mile and an efficiency index for the configuration that was elaborated by the authors and will be discussed later in the following sections.

B. Airplane analysis tool

The airplane calculator workflow shown in **Figure 75** is an essential part of the MDO framework. From airplane geometry and topology, and mission requirements, an iterative process for MTOW calculation is performed. Designated here of airplane analysis tool (AAT), this component is the masterpiece of the framework. AAT provides an embracing description and characterization of the airplane. Many levels of fidelity for discipline representation are available. Noise and emissions footprint can be optionally calculated. Detailed mission performance and range evaluations are derived from flight profiles set by the user and obeying air traffic constraints, all based on the aerodynamics, mass, and engine characteristics of the airplane. It is possible to examine any design mission or off-design missions corresponding to specific takeoff weights or required block distances.

Realistic airplanes obey must obey some requirements:

- Enough thrust to fly in the service ceiling at MMO.
- Required 2nd segment climb gradient.
- Required FAR 24.119 landing climb gradient.
- Required FAR 24.121 landing climb gradient.
- Enough thrust to perform en-route climb.
- Takeoff field length at a specified atmospheric condition and altitude.
- Landing field length at a specified atmospheric condition and altitude.
- Fuel storage to perform a mission with a specified range and payload.

The airplane mission setup is highly detailed with a flight profile that makes accurate calculations of major airplane masses possible like MTOW, OEW, and MZFW. Air traffic constraints can be incorporated into the calculation, if required [113]. Several aerodynamic methods are available in the framework with different levels of fidelity, including an artificial neural network surrogate model. An in-house generic turbofan engine model is also part of the MDO framework [110]. It is possible to analyze the performance, emissions, and operational costs for missions inside a complex airline network with different takeoff weights or block distances [17]. The fuel storage capacity is precisely calculated considering the actual airplane geometry and structural layout.

All mission segments are analyzed, and optimal and transitional climb altitudes are calculated considering buffet margins, available engine thrust, rate of climb, and accurate airplane lift-to-drag ratio. Alternate airport, hold and descent patterns, reserve and maneuvering fuels, and weight allowances are additional parameters. Typically, after the second segment climb, the in-route climb uses airspeed schedules, namely, a calibrated airspeed (CAS) segment followed by a constant previously stipulated Mach number up to the initial cruise altitude. The cruise phase can be flown at a constant altitude or following a step-increasing altitude pattern. There are two cruise speed profiles, one with a constant Mach number and a long-range pattern.

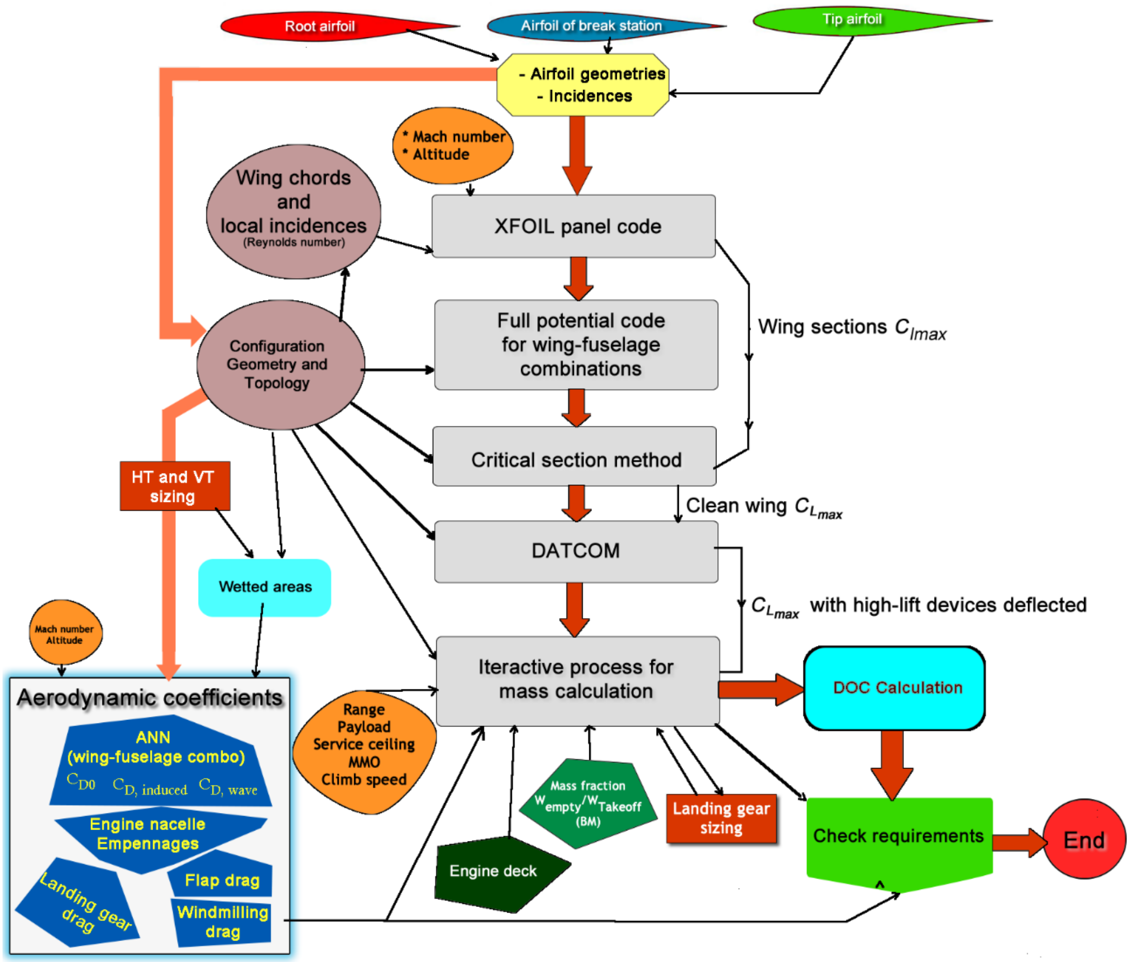

Figure 75: Workflow of the airplane analysis tool

C. Airframe weight and maximum takeoff weight

For the calculation of the maximum takeoff weight (MTOW), the estimation of the empty weight is needed, which can be supplied according to the MTOW (class I weight method) itself or it can be calculated by the sum of the individual structural weights and aircraft systems (Class II method). Within the Class I methodology, the following relationship between MTOW and OEW was developed at ITA:

$$\frac{OEW}{MTOW} = \left[a + b\left(\widehat{MTOW}\ \widehat{AR}\ TW\ \widehat{S_w}\ MMO\ \hat{L}_f\ F_w \hat{\Psi}\ \widehat{SC}\right)^{C0} + c\left(\widehat{MTOW}\right)^{C1}\left(\widehat{AR}\right)^{C2}(TW)^{C3}\left(\widehat{S_w}\right)^{C4}(MMO)^{C5}\left(\hat{L}_f\right)^{C6}(F_d)^{C7}(\Psi)^{C8}\left(\widehat{SC}\right)^{C9}\right] \tag{69}$$

Eq. 69 was tailored for a mix of units of the international and English systems. The MMO, *TW*, and F_w symbols refer to the maximum Mach of operation, the thrust-to-weight ratio, and the equivalent diameter of the cross-section of the passenger cabin, respectively.

Normalizations that were considered in **Eq. 69**, given in **Table 10**.

Table 10: Variable normalization for Eq. 69

$\widehat{MTOW} = \dfrac{MTOW}{50000}$	$MTOW$ = Maximum Takeoff Weight [kg]
$\widehat{AR} = \dfrac{AR}{8}$	AR = Wing aspect ratio
$\widehat{WL} = \dfrac{WL}{100}$	WL = Wing loading [kg/m^2]
$\hat{L}_f = \dfrac{L_f}{30}$	L_f = Fuselage length [m]
$\hat{\Psi} = \dfrac{\Psi}{20}$	Ψ = Quarter-chord sweepback angle [degree]
$\widehat{SC} = \dfrac{SC}{40000}$	SC = *Service Ceiling* [ft]

To obtain the exponents and multipliers of the terms of **Eq. 69**, the authors used a database of line aircraft containing information from 123 airliner models, with their entry into service from the 1950s up to others with commercial operation expected in 2020. **Figure 76** shows the relationship between the MTOW and the reference area of the wings for the aircraft in the database. An optimization algorithm was elaborated for the minimization of the mean quadratic error between the OEW/MTOW estimated by **Eq. 69** and the actual values of the airplanes in the database. The exponents and coefficients of **Eq. 69** are the design variables. The mono-objective genetic algorithm of MATLAB® 2019a [114] was used in optimization simulations and after 5500 generations the simulation was stopped. **Table 11** shows the coefficients and exponents that the optimization run provided. **Table 12** contains some estimation errors for the weight fraction of the present method. The agreement between the actual and estimated weights is very good.

Table 11: Values of the coefficients present in Eq. 69

a	b	c	C1	C2	C3	C4	C5	C6	C7	C8	C9
-0.2359	-0.3065	0.8900	-0.1731	0.0871	0.0857	0.1050	-0.0931	0.1220	0.2232	0.0857	0.0418

Table 12: Estimation error of weight fraction for some jet airliners

Airplane	Actual OEW/MTOW	Calculated OEW/MTOW	Percent error
Boeing 737-700	0.54157	0.53548	1.12
Airbus A320-200	0.54494	0.53829	1.22
B747-400	0.49077	0.4976	1.39
Boeing 757-300	0.53874	0.49639	7.86
Boeing 767-300	0.55681	0.55400	0.505
CRJ200ER	0.59806	0.59552	0.425
EMBRAER E170LR	0.55645	0.56798	2.07
Fokker 100	0.57074	0.55416	2.90
Tupolev Tu-104A	0.54737	0.56043	2.39
VFW 614	0.61048	0.60329	1.18

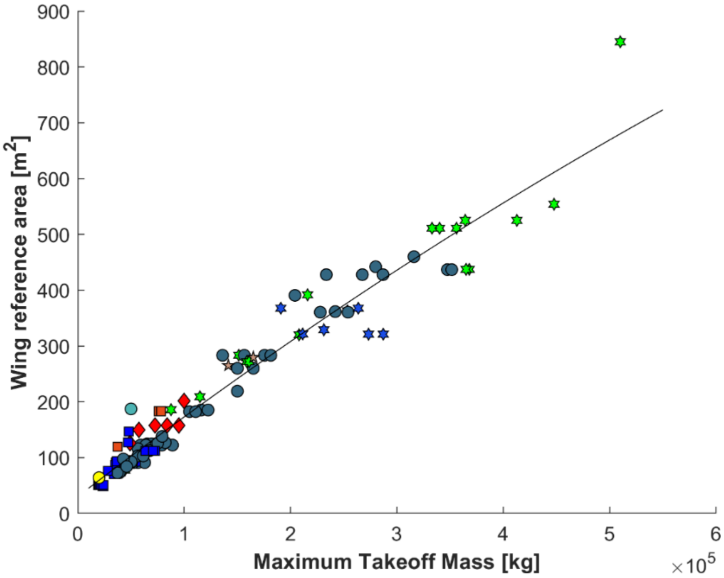

Figure 76: MTOW plotted against wing reference area considering airplanes utilized for the elaboration of Eq. 69. The different symbols in the graph reflect the different engine configurations

D. Engine weight

There are some simple methods as well as some more sophisticated methods for the estimation of turbofan engine weight [115]. But for WATE++, all of them are not accurate enough to be used in the optimization framework for airplane design. Thus, a methodology developed by Fregnani *et al.* [116] was adopted for turbofan engine weight estimation. This approach utilizes a formulation based on some engine geometric and thermodynamic parameters (**Eq. 70**).

$$W_E = \begin{matrix} T1 * (BPR/\overline{BPR})^a (OPR/\overline{OPR})^b (T_s/\overline{T})^c (D_E/\overline{D_E})^d (L_E/\overline{L_E})^e (\dot{m}/\bar{\dot{m}})^f + \\ T2 * (BPR/\overline{BPR})(OPR/\overline{OPR})(T_s/\overline{T})(D_E/\overline{D_E})(L_E/\overline{L_E})(\dot{m}/\bar{\dot{m}}) + T3 \end{matrix} \tag{70}$$

The coefficients and exponents of **Eq. 70** were obtained by an optimization using a genetic algorithm [114]. The objective was the minimization of the mean square error of known engine weights. A database, comprised of 20 engines, was elaborated which embraced a large variety of turbofan engines [14]. **Table 13** shows the T_1, T_2, and T_3 coefficients and a, b, c, …, f parameters obtained with the optimization process. **Table 14** shows the average parameters used for normalization in **Eq. 70**.

Table 13: Obtained exponents and coefficients for Eq. 70

Coefficient/exponent	Value
T1	2587.2461
T2	50.1920
T3	154.6179
a	-0.1965
b	-0.0718
c	1.0435
d	0.2493
e	-0.3444
f	-0.1455

Table 14: Parameters used for normalization in Eq. 70

Parameter	Value
$\overline{BPR}$	4.6911
$\overline{OPR}$	25.4000
$\bar{D}_E$ [m]	1.7906
$\bar{L}_E$ [m]	3.3276
$\bar{T}$ [kN]	148.1217
$\bar{\dot{m}}$ [kg/s]	464.7333

Table 15 contains weight estimation errors for some known turbofan engines.

Table 15: Weight error estimation for some known engines

Engine	Percent error
AE3007A1P	10.94
CF6-50C	2.55
JT8D-219	0.74
GE CF-34-10A	6.48
R&R RB211-535C	0.97
Trent 800-875	3.12
Williams FJ-44	4.29
Pratt & Whitney PW2040	0.44
GE-90/77B	0.31
R&R Tay 620	2.65

E. Direct operating cost

Although it is widely discussed which cost elements do belong to *Direct* Operating Costs and which do not, it is generally accepted that DOC includes those cost elements which depend on the equipment (aircraft) and crew that are necessary to perform a given flight. On contrary, *Indirect* Operating Costs (IOC) depend on the way an airline is administrated [117]. The ATA 67 DOC method [118], a good reference, considers as aircraft-dependent and hence part of DOC:

- cockpit crew costs,
- fuel costs,
- maintenance costs,
- depreciation,
- insurance (against hull loss).

Cockpit crew cost is heavily dependent on MTOW, and it is calculated in terms of flight hours. Training costs for the crew or maintenance personnel traditionally are considered as a percentage of the crew's fixed cost. For the engine, it is necessary to provide to the DOC calculation routine the number of engines, the engine weight, and the time between overhauls that is considered.

Figure 77 displays the result of a direct operating cost estimation performed for the hypothetical 76-seat ITA76ADV airliner with a design range of 2100 nm. The calculation considered two jet-fuel prices, US$ 1.70 and US$ 2.389, a 40.6% increase. The contribution to DOC increased from 25% to 31%, surpassing the crew slice related to that cost. Thus, as expected, the DOC is indeed sensitive to fuel price.

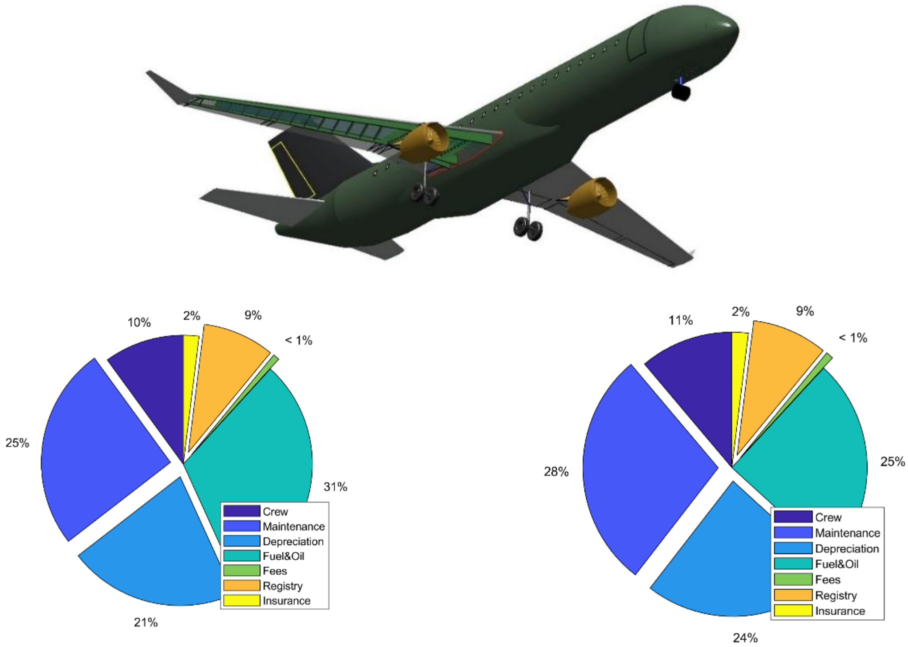

DOC: US$ 10.82/nm DOC: US$7.85/nm

Jet A1: US$ 2.387/gallon Jet A1: US$ 1.70/gallon

Figure 77: DOC breakdown for the ITA76ADV considering two Jet A1 fuel prices

The values here calculated for the DOC have estimated values and no comparison to actual values practiced by airlines is possible, because they handle this information as strategic and confidential. Nevertheless, it offers a relatively good basis for comparison among the airplanes that are an object of investigation. It is worth mentioning, that changing the fuel price will significantly alter the way the airplanes are evaluated, as shown in **Figure 77**, and eventually it could be part of a Pareto front. Ref. [119] provides graph information about the annual variation in jet fuel price.

Efficiency index

The authors elaborated a parameter that synthesizes the value of an airliner and that was designated here as efficiency index:

$$EI_{Liner} = \frac{\widehat{Rnm} \times MMO \times \widehat{NPAX}}{\left(TW \times \widehat{OEW}\right)} \tag{71}$$

The symbols of **Eq. 71** are:

$$\widehat{NPAX} = \frac{NPAX}{150} \quad \widehat{Rnm} = \frac{Rnm}{2500} \quad \widehat{OEW} = \frac{OEW}{40000}$$

An airplane presenting low efficiency may be an indication of a low range, a low cruise speed, or a high OEW for the mission it was conceived for. A low speed may appear not to be important, but it can be translated into a longer block time that impacts DOC. Besides, slower airplanes are obligated by air traffic control to fly at lower altitudes to not interfere with faster airplanes. Flying at lower altitudes, in turn, may cause a higher fuel consumption depending on the mission profile.

F. Passenger cabin sizing

Considering that the medium-range aircraft is the subject of the present research, a two-class cabin configuration was selected, where the cabin is configurated with 10% of the seats destined for first-class, and the other 90% are economy class, this proportion being suggested by [120]. The fuselage is modeled as a long cylinder with a constant ellipsoidal cross-section whose length is determined by the cabin length variable **(L_f)** and the shape of the ellipse by the height-to-width ratio variable (F_{hw}).

The cabin sizing module is divided into two steps. Initially, the layout of the cross-section of the passenger cabin is defined. The cargo hold space of the aircraft is also considered. In the present work, a container of type LD3-45W (2.44m x 1.53m x 1.14m) has been considered. The function makes the layout obey all the minimum clearance distances. A MATLAB® routine was written to design the cross-section of passenger cabins. After sizing the cross-section, the second step begins with the elaboration of the cabin floorplan. The cabin plan code calculates cabin length, toilet and galley positions, emergency exit sizing, and other relevant parameters. **Figure 78** shows an example of some cabin cross-sections. FAR 24.810 rules are employed in the incorporation of emergency exits. Additional considerations are carried out to comply with ditching regulations.

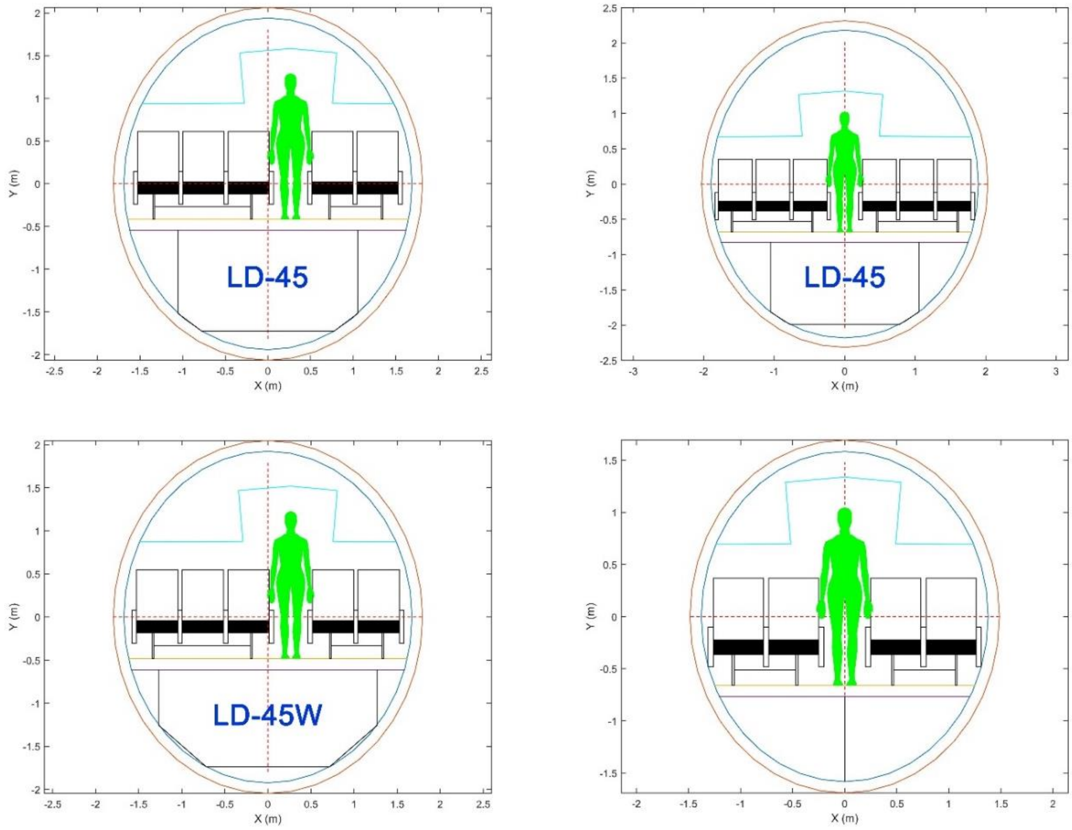

Figure 78: Examples of fuselage cross-sections

6.3 Verification of the B757-200 airliner

The B757 has a six-abreast cross-section and is powered by either RB211 or PW2030 and PW2040 Series turbofans. The B757-200 is the basic version, which entered service in 1983.

In August of 1978, Eastern Airlines and British Airways announced orders for the B757 and chose the RB211-535 to equip the airplane [121]. Designated RB211-535C, the 3-spool engine entered service in January of 1983 when the first B757-200 was delivered to Eastern Airlines. The engine has a nominal thrust of 37,400 lbf (166.36 kN) and an OPR of 21.2:1 [122]. In 1979, Pratt & Whitney launched its PW2000 engine, claiming 8% better fuel efficiency than the -535C for the PW2037 version [121]. The English engine manufacturer reacted and using the -524 core as a basis, the company developed the 40,100 lbf (178 kN) thrust RB211-535E4, which entered service in October of 1984. There are differences in appearance between the two versions like a mixed exhaust nozzle and a bigger fan cone for the RB211-535E4. BPR was slightly reduced to 4.40:1 from 4.46 for the 535C [122]. There is another version of the Rolls&Royce engine designated RB-211E4B, which has a takeoff thrust of 43,500 lb [123]. The 535E4 engine was also the first to use the wide chord fan which increased efficiency, reduced noise, and gave increased protection against damage from foreign object ingestion [121]. As a result, a relatively small number of -535Cs was installed on production aircraft in May of 1988. American Airlines ordered 50 B757s powered by the -535E4 emphasizing the engine's low noise as an important factor for their choice. The stretched version B757-300 entered service with Condor Flugdienst in 1999. With a length of 54.5 m, the type is the longest single-aisle twinjet ever built.

According to Ref. [124], The B757-200 has several sub-versions presenting different MTOW, OEW, and MZFW. Two configurations fitted with RB211-535E4B engines were selected as references for the ongoing work, and their payload-range diagrams are shown in **Figure 79** and some characteristics are given in **Table 16** [123]. Two ranges signaled by the dashed lines in the payload-range diagrams are related to a mission with a payload of 192 passengers.

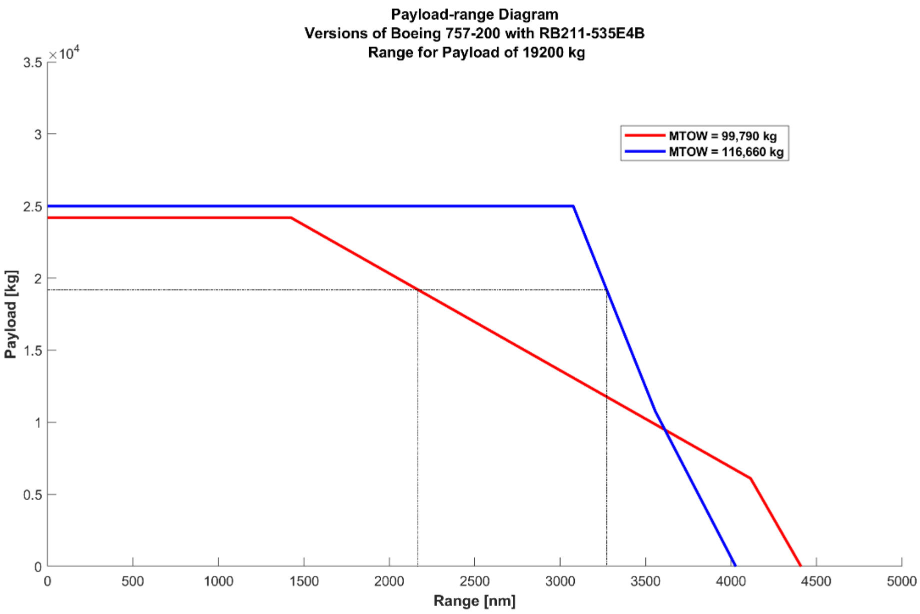

Figure 79: Payload-range diagram for some sub-versions of B757-200 [123]

Table 16: Characteristics of two B757-200 sub-versions fitted with RB211-535E4B engines [121] [122] [123] [125]

Sub-version	MTOW	OEW	MZFW	Usable fuel	Takeoff Thrust	TFL
1	99,790 kg	58,570 kg	83,460 kg	42,680 kg	37,400 lbf	1,660 m
2	115,650 kg	58,570 kg	84,360 kg	43,490 kg	43,500 lbf	2,070 m
L_f	**wAR**	**wS**	**wSw14**	**MMO**	**Aisle width of Y-class**	
46.97 m	7.82	185.25 m^2	25°	0.86	0.508 m	

Some of the B757-200 main characteristics calculated by the present methodology are given in **Table 17**. Again, the agreement between actual and estimated weights is particularly good. The year 1984 was set for the year of service entry. As expected, the airplane was categorized as a classic design (scaled trajectory). However, just for testing, if the year 1981 were adopted for that parameter, the airplane would be labeled by the entropy statistics classification program as a breakthrough, as also is expected. The reason behind this is simple: this way the configuration being analyzed passes its unique characteristics to the actual airplanes that entered service in 1983 and 1984, which are part of the database.

Table 17: Estimated values for the B757-200 fitted with RB211-535E4 by the present design

MTOW	OEW	Fuel Capacity	Range	Categorized as
115,100 kg	58,495$^\alpha$ kg	41,138$^\beta$ kg	3,272 nm $^\alpha$	Classic
α @ FL370 and FL390, Mach of 0.80, payload of 19,200 kg, ISA+0 ºC, takeoff with MTOW, RB211-535E4, 200 nm to an alternate, 30 min loiter @ 1,500 ft				
β wing capacity of 30,918 kg / ε Jet A1 price of US$ 2.387 US$/gal				

6.4 NeoCASS

NeoCASS is an open-source computational package written in MATLAB® that was conceived to be a structural analysis tool focused on the conceptual and preliminary design of aircraft [108]. It is also a structural module for the design framework CEASIOM, a project conceived by SimSAC. The CEASIOM project was started in 2006 with the support of several contributing institutions around the world. The software is divided into several modules, and Politecnico di Milano was responsible for developing a module for aeroelastic studies in conceptual phases, which was called NeoCASS.

The NeoCASS suite was developed with the following objectives:

- Ensure easy coupling with other codes.
- be relatively accurate for the conceptual phase and provide correct trend data to allow the project to move in the proper direction.
- be computationally efficient.
- be interchangeable between speed and accuracy, leaving the level up to the user required mesh discretization.
- do not need many model preparations.
- provide sensitivity derivatives by changing design variables.

Besides other capabilities, NeoCASS provides a method based on fundamental structural principles to estimate the structural weight of an aircraft, which is a hybrid method, because it uses both empirical calculations, based on the actual weights of existing aircraft, and analytical calculations, based on the utilization of simplified finite element models. In this way, it is possible to obtain good results even using unconventional aircraft configurations. For this, the software has an approach in which empirical calculations are first performed, so that, throughout the analyses, the structural weights are changed. For the analytical structural design, different operating conditions from standards or the user are used. The software can deliver both aircraft detail results, such as structural masses; static and dynamic aeroelastic behavior. The explanations about all the methods used in the software that will be presented below were taken from Cavagna and Ricci (2013), which is the software manual.

Figure 80 displays the NeoCASS architecture that was employed in the present study. The suite is composed of two main modules, which are GUESS (Generic Unknown Estimator in Structural Sizing) and SMARTCAD (Simplified Models for Aeroelasticity in Conceptual Aircraft Design), whose functions and operating principles will be explained in detail later. In gray are represented the preprocessing modules called AcBuilder (Aircraft Builder) and WB (Weight and Balance). These modules are considered pre-processing, as they are used only in the creation or preparation of the aircraft.xml file, which is in green color, which is the file that contains all the information of the aircraft and is used in all phases of the program. Also in green is another input file that is called smartcad.dat. This file merges data outputs from GUESS with some parameter settings for solving aeroelastic phenomena. In yellow are the files that must be configured by the user, where the characteristics of the maneuvers and analysis modes to be considered by the program are found. In light blue color are the program outputs, which are the analytical structural masses of the aircraft, the vibration modes, the *mesh.dat* file, which is a structural representation of the aircraft based on a beam model, and the file *smartcad.dat*, which is a file compatible with other software like NASTRAN for post-processing analyses.

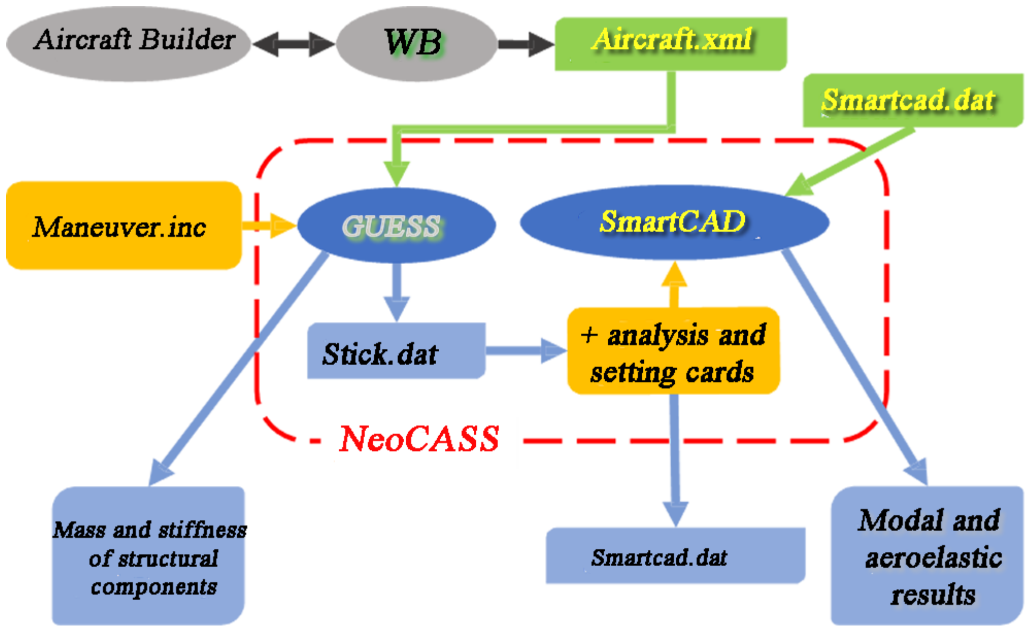

Figure 80: NeoCASS architecture

6.5 Sensitivity analysis

A. Influence of aspect ratio on the flutter speed

To measure the influence of wing geometric parameters on flutter speed, a sensitivity study was conducted by varying wing geometric parameters and determining flutter speed using the present design framework. Wing taper ratio, aspect ratio, and sweep were the geometric parameters that suffered variation.

The aspect ratio has a large influence on the flutter speed, as can be seen in **Figure 81**, which always poses a challenge for aircraft design teams. As expected, the results show that an aspect ratio increase leads to a significant reduction of flutter speed. This is due to the decrease of the wing inertia and the bending moment increase at the wing root. Another important aspect is the small effect of Mach number increase on the flutter speed of the wing analyzed here. The results shown in **Figure 81** agree with the results presented by Opgenoord [105].

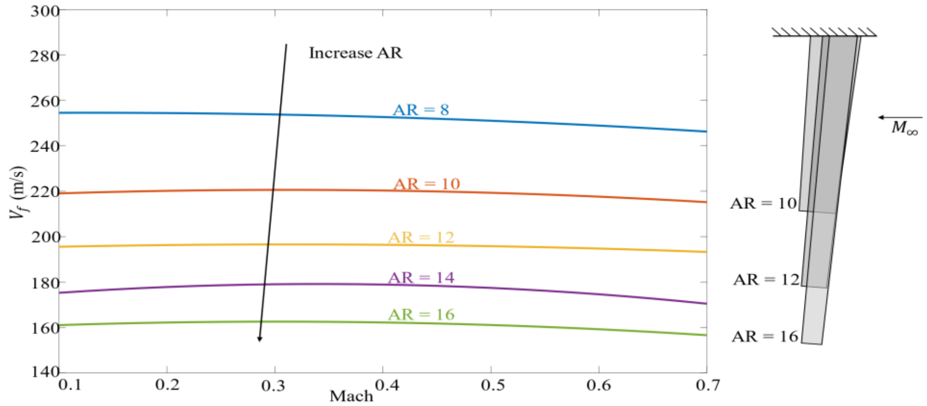

Figure 81: Influence of aspect ratio on flutter speed

B. Influence of wing taper ratio on the flutter speed

The taper ratio tends to decrease the flutter speed when it is increased, as can be seen in **Figure 82.** It can be observed that the Mach variation does not have much effect on the flutter speed and the taper ratio only determines the offset between the curves. This is to be expected since the increase in taper leads to an increase in the total bending and twisting moments, which increases the natural frequency of the wing, as shown in the work of Opgenoord [105].

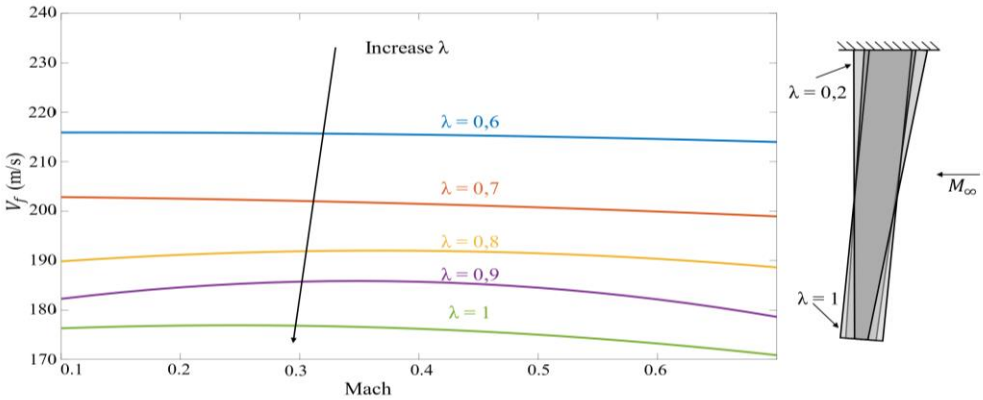

Figure 82: Influence of taper ratio on the flutter speed

C. Influence of sweep on the flutter speed

The wing sweepback angle also has a large influence on the flutter speed, as can be seen in **Figure 83**. It shows a similar behavior as for the aspect ratio as a function of Mach number. On the other hand, as the sweep increases, the flutter speed also increases, which is the opposite result of the aspect ratio. This result was also recorded by Barmby [126].

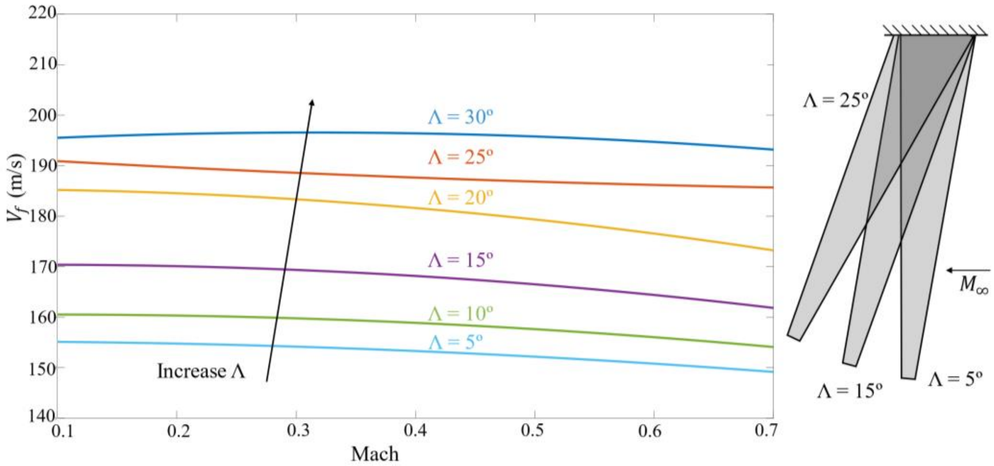

Figure 83: Influence of sweep on the flutter speed

6.6 Results

A. Design variables

The design variables that were used to generate the models of each aircraft are described in **Table 18**. It was necessary to establish lower and upper bounds for each of these variables, as this way it is possible to prevent the algorithm from searching for unconventional individuals during the optimization in regions where the models are not validated, generating misleading results or even in a region where these individuals are unfeasible. The boundaries for each of these variables are also shown in **Table 18**. The boundaries are based on typical values for airliners with passenger capacity varying from 130 to 220, with a small amount of tolerance being added to ensure design space freedom for the optimizer.

Table 18: Boundaries of variables of the present optimization problem

Variable	Lower boundary	Upper boundary
Wing Area ($\boldsymbol{S_w}$)	110 m²	210 m²
Aspect Ratio ($\boldsymbol{AR_w}$)	7.7	11.0
Taper Ratio ($\boldsymbol{\lambda_w}$)	0.24	0.45
Wing Quarter-chord Sweepback angle ($\boldsymbol{\Lambda_w}$)	22°	32°
Fuselage Length ($\boldsymbol{L_f}$)	36 m	50 m
Height/width of central fuselage ratio (F_{hw})	0.9	1.1
Design range starting with MTOW, ISA conditions ($\boldsymbol{R_{nm}}$)	2100 nm	3700 nm
Maximum Mach Operating (MMO)	0.78	0.83
Maximum aircraft certified altitude (SC)	35000 ft	41000 ft
Maximum Takeoff Thrust at sea level / ISA conditions (T)	220 kN	400 kN

B. flight envelope

To define the application of the flutter constraint, it was initially necessary to define the flight envelope of each aircraft being analyzed. The graph of altitude versus speed limit was then elaborated as an example (**Figure 84**).

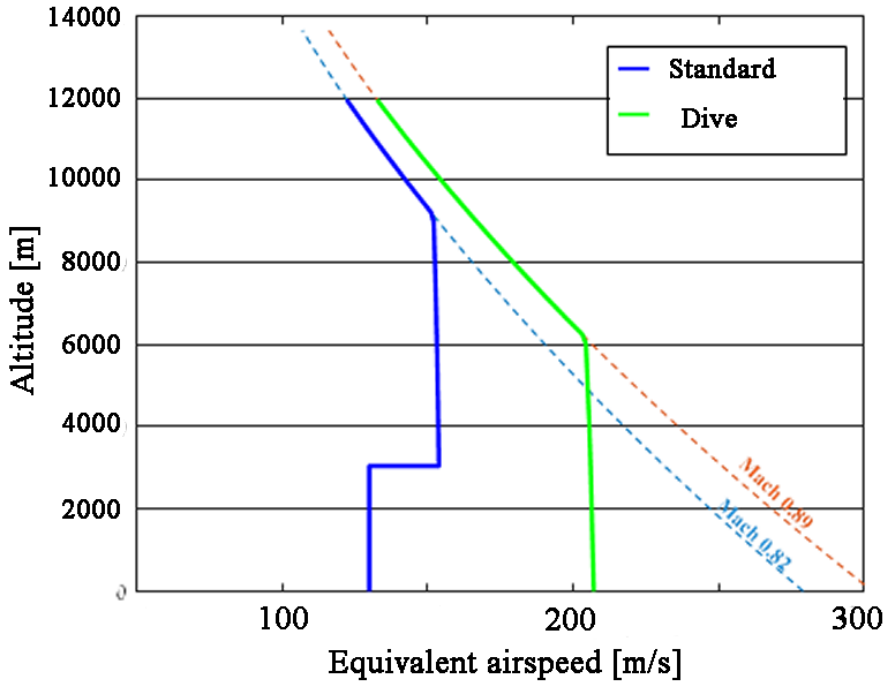

Figure 84: V-H diagram

The flight envelope shown in **Figure 84** restricts the maximum speed possible to be achieved by the aircraft at a certain altitude. The dark blue line represents the flight envelope for a typical mission, where a climb is performed at a constant calibrated speed of 250 kts up to an altitude of 10,000 ft. Afterward, a climb at a constant calibrated speed of 310 knots to crossover altitude is established. Finally, there is the cruise phase, in which the aircraft MMO was the cruise Mach number, which for the airplane of **Figure 84** was 0.82. The green line represents the aircraft's maximum dive speed. In the constant calibrated speed region, 350 kts were used for the envelope considering the dive speed, which was derived from the VMO of some aircraft in the category. VMO is usually associated with operations at lower altitudes and deals with structural loads and flutter. In the region at constant Mach number, the dive speed (Md) is given by:

$$M_d = MMO + 0.07 \tag{72}$$

The FAR 25.629, which determines the aeroelastic stability requirements of commercial aircraft, the minimum limit for the aeroelastic instability velocity is obtained from the V-H diagram of the aircraft's flight envelope. The aeroelastic instability threshold value is drawn from the aircraft's dive velocity curve and must be 15% greater at an equivalent velocity. If this value exceeds 1.00, in the constant Mach region, the value of 1 should be adopted for the Mach number. Based on the V-H diagram shown in **Figure 84**, the diagram of **Figure 85** was elaborated to comply with FAR 25.629 requirements.

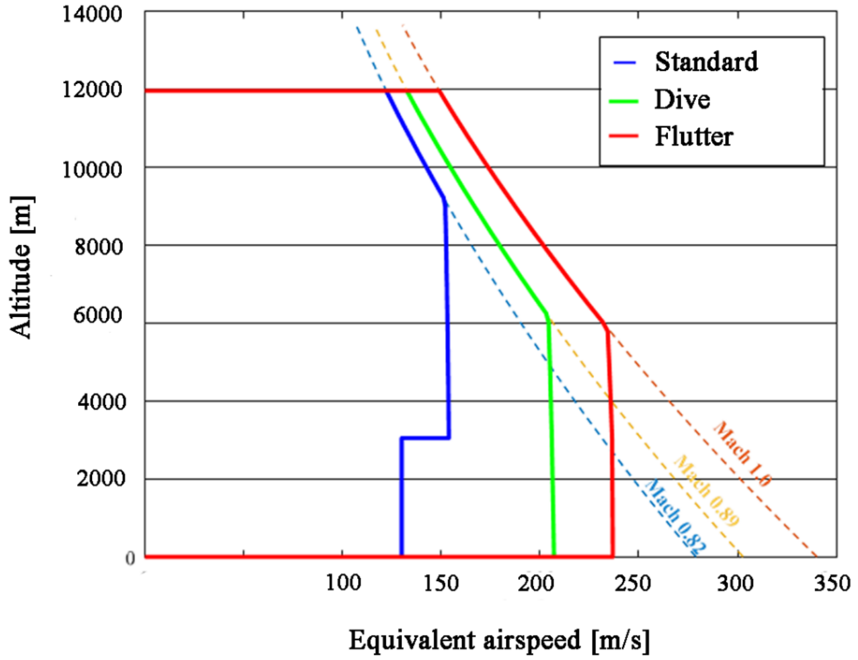

Figure 85: Flight envelope considering flutter speed constraints

C. Multi-objective optimization without flutter constraint

A multi-objective optimization design task was carried out without any flutter constraint. After 35 generations with 55 individuals using the MATLAB® multi-objective genetic algorithm, the number of feasible individuals that emerged from the computations was 1682, i. e., those not violating any constraint. (**Figure 86**) - out of a total number of 1925 configurations analyzed. The analysis of each plane took on average 30 seconds and the optimization task lasted about 16 hours on a Desktop PC fitted with Intel® I9-9800K processor and 32 GB of RAM.

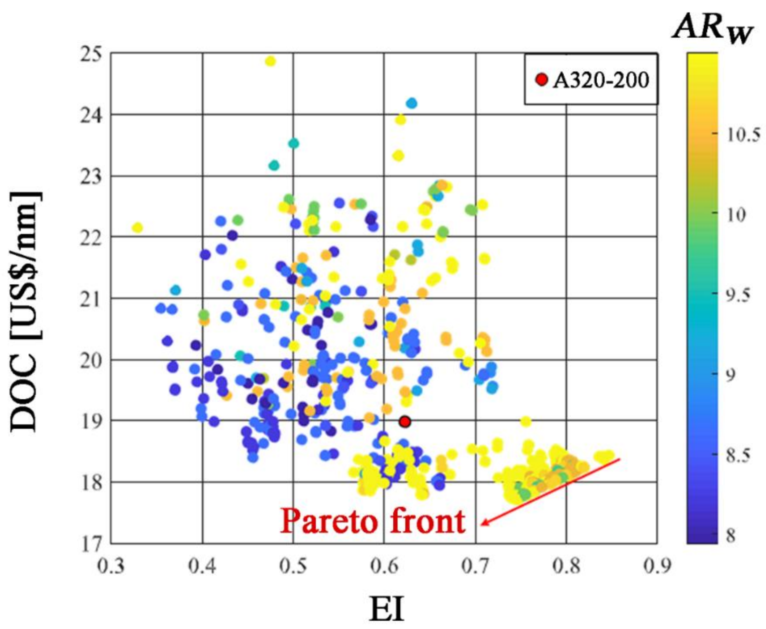

Figure 86: Optimization task with no flutter constraint

The individuals belonging to the Pareto front presented a wing aspect ratio higher than 9.92. **Table 19** contains some characteristics of the optimal airplanes.

Table 19: Some design variables of individuals belonging to the Pareto front of the optimization without flutter constraint

ID	S_w [m²]	AR_w	λ_w	L_f [m]	R_{nm}	DOC [US$/nm]	EI
1855	171.65	10.92	0,263	38.9	3470	18.46	0.846
1627	171.65	10.42	0,267	37.1	3470	18.04	0.790
1808	170.65	10.67	0,263	36.4	3470	17.85	0.765
1907	171.65	9.92	0,263	37.1	3471	18.07	0.795
1590	171.65	10.92	0,263	36.0	3470	17.73	0.744

All individuals in Pareto front for classic airliners share some features:

- MMO of 0.83.
- Wing quarter-chord sweepback angle of 22º.
- Height/width ratio of the central fuselage of 0.91.
- Maximum Takeoff Thrust at sea level of 303 kN.
- Maximum aircraft certified altitude 35,000 ft.

Table 20: Selected optimal airplanes compared to the A320-200 airliner

	A320-200	Highest *EI*	Lowest *DOC*
MTOW [kg]	76,653	89,579	84,771
OEW [kg]	43,298	49,514	47.,439
Npax	150	156	140
AR_w	9.50	10.92	10.092
Range [nm]	2550	3470	3470
Wing area [m²]	122.4	171.65	171.65
EI	0.622	0.846	0.745
***DOC* [US$/nm]**	18.99	18.46	17.73

Table 20 contains some estimated characteristics of the A320-200 airliner compared to those of two optimal individuals. The data for the airplanes presenting the highest *EI* and the lowest *DOC* is compared to those figures estimated for A320-200. To satisfy the maximization of the *EI*, the algorithm found solutions with larger wing areas to increase the fuel capacity, leading to an increase in range. Comparing the aircraft with the highest *EI* to the one with the lowest *DOC*, both present similar characteristics but different passenger capacity carried and the maximum take-off weight, characteristics that directly modify *DOC*.

The aircraft with the smallest *DOC* (#1590) presented a short fuselage and therefore a smaller number of passengers. This characteristic resulted in a reduction in empty weight of about 2 tons when compared with the aircraft with the higher *EI* (#1855). The smaller fuselage also leads to a reduction in the wetted area of the aircraft, a parameter directly related to drag. These factors are crucial for reducing the aircraft's fuel consumption and consequently *DOC*. On the other hand, the aircraft with the highest *EI* (#1855) had the longest fuselage length among the aircraft located at the Pareto front, which is expected, because the number of passengers is a parameter directly proportional to *EI*. The analyzes have shown that the characteristics that most affect the results of *EI* and *DOC* were aspect ratio, range, and wing area.

D. Multi-objective optimization with flutter speed constraint

The second task of the multi-objective optimization involved constraining the flutter speed within the flight envelope of the aircraft. Again, after 35 generations of 55 individuals, using the *gamultiob*j algorithm [95], a set of 1491 viable individuals, i.e., those not violating any constraint. (**Figure 87**) - out of a total of 1925 configurations analyzed. The analysis of each plane took an average of 180 seconds, and the total optimization runtime was about 96 hours. The Pareto front consisted of a total of 146 individuals. **Table 21** contains information on some individuals that belong to the Pareto front.

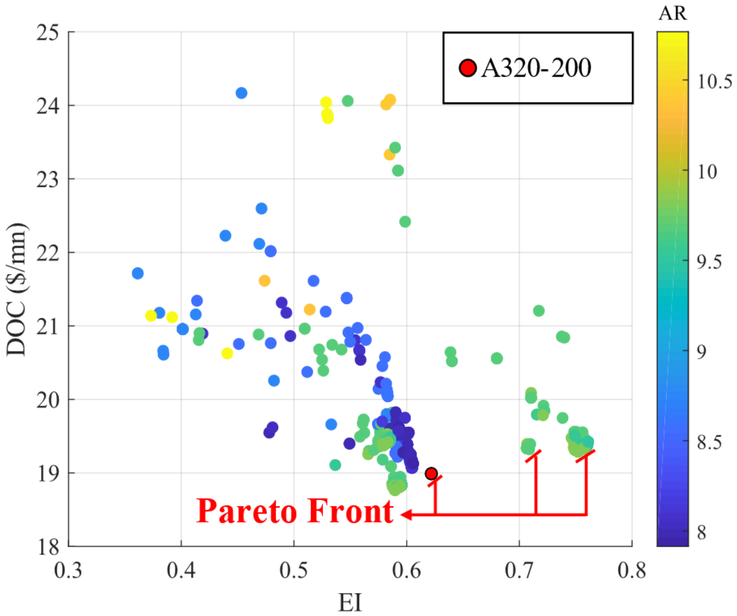

Figure 87: Optimization results with flutter constraint

The number of viable individuals has decreased with the inclusion of this new constraint. In this optimization run, the Pareto front is formed by three small, interspersed regions containing many individuals. This front happened at this time as the algorithm found two viable and distinct solutions which gave good results. Another interesting from the obtained results is the low occurrence of individuals with an aspect ratio higher than 10, which is due to the flutter constraint. In the present optimization, we note that one of the regions of the Pareto front is very close to the A320 plane, indicating results that are more in line with reality.

Table 21: Some design variables of individuals belonging to the Pareto front of the optimization with flutter constraint

ID	S_w [m²]	AR_w	λ_w	L_f [m]	F_{hw}	R_{nm}	SC [ft]	DOC [US$/nm]	EI
1462	177.97	9.49	0.342	39.3	0,90	3409	40,000	19.42	0.761
1107	177.97	9.68	0.258	39.2	0,90	3409	40,000	19.31	0.753
1839	144	8.03	0.256	39.2	0,90	2725	35,000	19.07	0.604
1273	144	7.94	0.258	39.2	0,92	2725	35,000	19.12	0.605
1870	144	9.81	0.258	39.2	0,90	2725	35,000	18.76	0.589

All individuals in the Pareto front for classic airliners share some features:

- MMO of 0.83.
- Wing quarter-chord sweepback angle of 22º.
- Maximum takeoff thrust at sea level of 339 kN.

Table 22 shows some characteristics of the A320-200 aircraft compared to those of optimal individuals with the highest *EI* and the one with the lowest *DOC*. Comparing the characteristics of the A320 with the characteristics of the higher EI aircraft, it is again noticeable that due to the objective of maximizing the *EI*, the algorithm has searched for solutions with larger wing areas to increase the fuel capacity, which leads to an increase in the range. However, comparing the characteristics of the A320 with those of the aircraft with the lowest *DOC*, it was found that at this time these aircraft presented very similar characteristics. This feature occurred because aircraft with high aerodynamic efficiency was no longer feasible by subtracting the flutter speed, thus the other parameters that compose the calculation of *DOC* became more important. As a result, smaller aircraft have become more attractive as they have lower maintenance, crew, and depreciation costs.

Table 22: Selected optimal airplanes compared to the A320-200 airliner

	A320-200	Highest *EI*	Lowest *DOC*
MTOW [kg]	76,653	91,554	82,343
OEW [kg]	43,298	50,424	46,342
Npax	150	160	158
AR_w	9.50	9.49	9.81
Range [nm]	2550	3409	2725
Wing area [m²]	122.4	178.0	144.0
EI	0.622	0.761	0.589
***DOC* [US$/nm]**	18.99	19.43	18.78

According to the figures contained in **Table 22**, range and passenger capacity are directly proportional to *EI*. Therefore, larger aircraft and consequently aircraft with greater range and number of passengers tend to have higher *EI* values. The aircraft found with the highest *EI* (#1462) meets this standard, as it combines the greater range and greatest number of passengers of the Pareto front.

6.7 Impact of aspect ratio on optimal design

The plots shown in **Figure 88** provide a good comparison between the results of the two optimization tasks carried out here. They show the feasible individuals that emerged in the optimization runs and related Pareto front at the same scale.

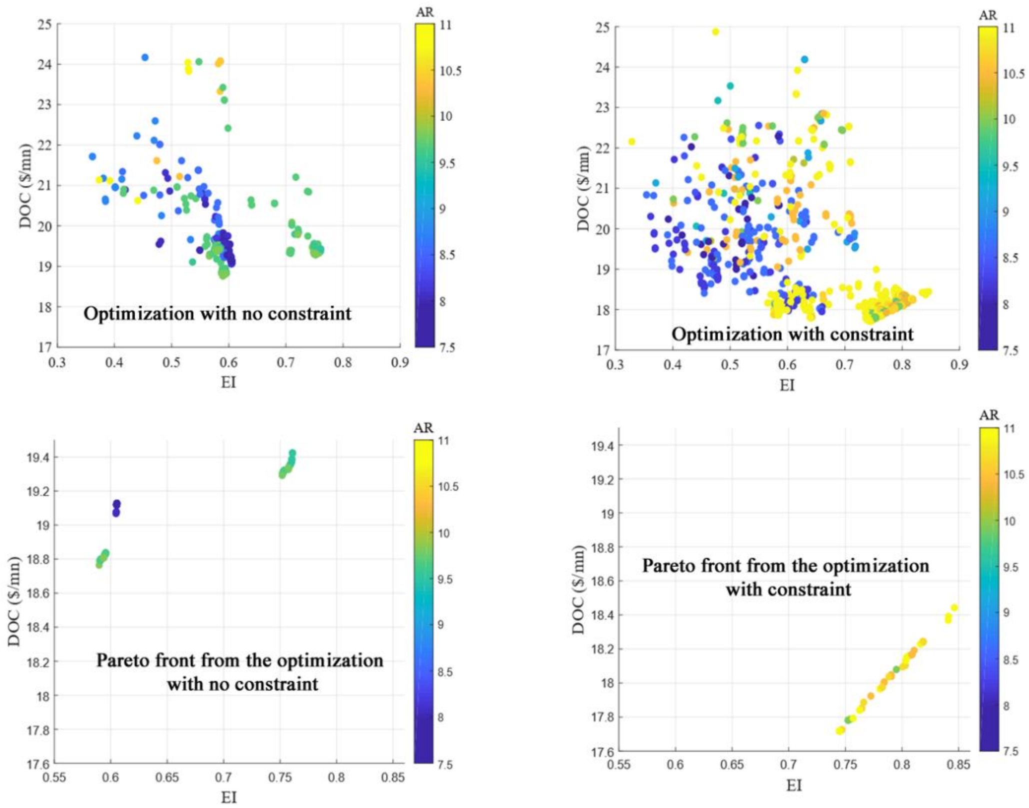

Figure 88: Comparison between the optimization tasks with and no flutter constraint

Comparing the results in **Figure 88 (a)** and **(b),** it is noticeable that optimization with no flutter speed constraint resulted in optimal individuals with an aspect ratio close to 11, in a much higher proportion than in the results obtained from the optimization task where the constraint was incorporated. This feature can be explained as individuals with a higher aspect ratio present lower flutter speed, as can be seen in **Figure 88**, which was penalized when the flutter constraint was added to the optimization procedure. The added constraint equation also led to a change in the position of the Pareto front, which is much more central in **Figure 88 (b)**, showing the significant degradation of the results found. When comparing the Pareto frontiers in **Figure 88 (c)** and **(d)**, it is noticeable that the Pareto frontier from the optimization with no flutter speed constraint is composed of individuals with a high aspect ratio than those from the optimization task where the constraint was imposed.

Table 23 contains the characteristics of the aircraft with the highest *EI* of the two optimizations and **Figure 89** shows a simplified top view of both. The two aircraft have similar solutions because in both cases maximizing the *EI* led the optimizer to look for aircraft with a larger wing area, passenger capacity, and range. However, due to the lower aspect ratio, the flutter-constrained aircraft has poorer aerodynamic performance and therefore a 10% lower *EI* and a 5.25% higher *DOC*. In addition, the poorer aerodynamic performance caused the optimizer to further increase some design variables of the flutter-constrained aircraft, which consequently has a larger wing area, cabin length, and overall traction. Despite the larger wing area, the constrained aircraft has a shorter range due to the degraded aerodynamic performance. Overall traction was increased because more traction was required to meet climb requirements due to increased drag.

Table 23: Comparison of design variables of higher EI aircraft

Aircraft	ID	S_w [m²]	AR_w	λ_w	Λ_w
With no constraint	1855	171.65	10.92	0.263	22
With constraint	1462	177.97	9.49	0.342	22
L_f [m]	**WR**	R_{nm}	**MMO**	**SC [ft]**	**T [kN]**
38.9	0.91	3470	0,83	35,000	303
39.3	0.90	3409	0.93	40,000	339

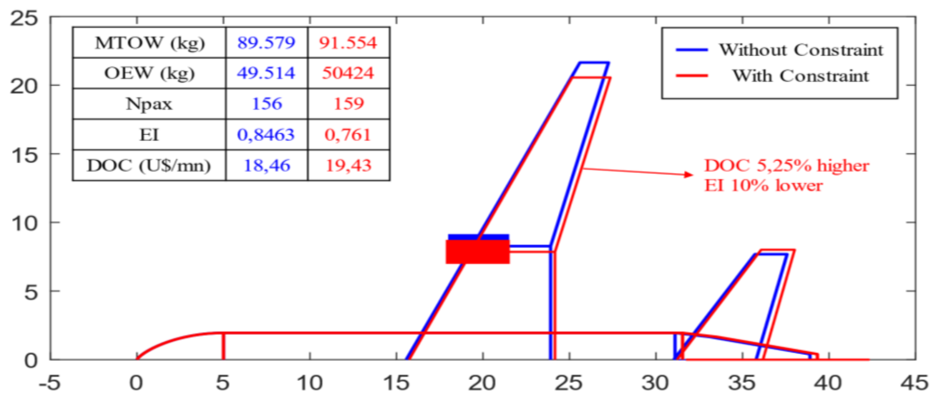

Figure 89: The largest *EI* aircraft with and without restriction

Table 24 contains the design variables of the aircraft with the lowest *DOC* of the two optimizations, and **Figure 90** has their top views. In this case, the two aircraft presented significantly different characteristics, as the aircraft with the smallest DOC showed a longer range and a shorter fuselage length in the unconstrained optimization, while the range was reduced, and the cabin size increased in the constrained optimization. Despite this fact, the restricted aircraft presented poorer aerodynamic performance and consequently a 5.92% higher *DOC* and a 20.9% lower *EI*. This large difference in EI is justified by the different passenger numbers and ranges that place the aircraft in different market niches. Full traction was again increased to meet climb requirements.

Table 24: Comparison of design variables of the optimal aircraft with the lowest *DOC* that resulted from the two optimization tasks

Aircraft	ID	S_w [m²]	AR_w	λ_w	Λ_w
Without constraint	1855	171.65	10.92	0.263	22°
With constraint	1462	177.97	9.49	0.342	22°
L_f [m]	**WR**	R_{nm}	**MMO**	**SC [ft]**	**T [kN]**
38.9	0.91	3470	0.83	35,000	303
39.3	0.90	3409	0.93	40,000	339

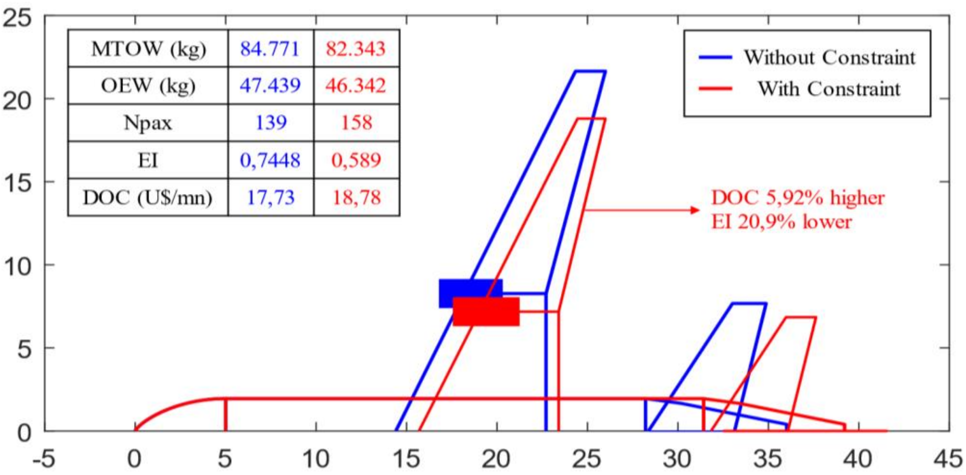

Figure 90: The lowest DOC aircraft with and without restriction

Another important difference between the results is the time that was taken to fulfill the two optimizations. Although the two optimizations used the same computer configuration, the computational cost for the optimization with the flutter constraint was six times higher than that for the optimization without the flutter constraint. This shows that aeroelastic analyzes significantly increase the computational cost, especially considering that the analyzes only consider one case of takeoff weight, while normally this type of analysis considers different weights and Mach numbers.

7 Conclusions

This Chapter intends to discuss the importance of incorporating medium and high-fidelity aeroelastic tools into multi-disciplinary and multi-objective design platforms tailored to handle transport airplanes. In addition, the development of surrogate models for transonic flow representation with acceptable levels of accuracy is also the objective of this Chapter. For a better understanding of these topics alongside the three computational applications contained here, additional Sections are also part of the present Book Chapter, namely an overview of induced drag and new aircraft configurations, as well as the meaning of machine learning and its objectives.

The following topics were discussed in this Book Chapter:

The quest for high aspect-ratio wings has led to new airplane configurations to reduce induced drag. A dual-fuselage configuration was especially analyzed. Some pros and cons related to the adaptation of such configuration for passenger and cargo transport were raised. Structural considerations were also discussed for a strut-braced airliner.

A closely coupled FSI approach was used to investigate the aeroelastic behavior of the KC-135. Detailed structural and aerodynamic characteristics could be captured for this airplane, enabling the verification of main effects that arose from the winglet incorporation, verifying how the flexibility of the structures affects the aerodynamic behavior of the wing and the winglet. Besides the validation of the approach adopted here, corroborated by the excellent agreement with wind tunnel and flight test, an outstanding capacity of prediction of the aeroelastic phenomena is available, both qualitatively and quantitatively. The main utility of modeling these coupled physics is to obtain more accurate metamodels for preliminary studies, calibration of aeroelastic plant models for control purposes, and parametric models to perform multidisciplinary optimization studies. Thus, the objective of utilizing it from the design of morphing winglets is fulfilled.

Full potential flow is a very attractive approach for MDO platforms that are elaborated for aircraft conceptual design. Besides 3D applications, a computer code for the inverse transonic airfoil design was presented and its performance and accuracy are excellent. The design methodology presented at issue proved to be a simple and efficient tool for preliminary wing design, always converging towards unique solutions for each set of reasonable prescribed Cp distribution. After a few design iterations, it is possible to introduce large geometric modifications on the wing airfoil sections, and properly reproduce a suitable pressure distribution.

A surrogate model with ANN to replace a full-potential code in airplane MDO frameworks was presented. A database of approximately 72,000 cases to train and design the ANNs was generated. The size of the database was checked with the learning curves method. It is also important to visualize how the input variables of the database were distributed over the proposed domain, as this had a direct impact on the prediction errors distribution along with the domain of each input variable. Several multi-layer feed-forward ANNs were trained using the scaled Levenberg-Marquardt algorithm. ANN architectures in terms of several neurons were selected based on minimum mean squared error presented by approximately 5000 cases that did not take part in the training/validation/test of the networks. The ANNs dedicated to the three drag components, parasite, induced, and wave, give better predictions when compared with the single-network approach. The parasite drag coefficient presents the toughest patterns for ANN learning. A reduction of 1660 times in computational cost was recorded, with average absolute errors lower than one drag count for all kinds of drag coefficients. According to the results, it is possible to set up ANN to substitute CFD software to reduce the computational cost in a multidisciplinary optimization framework, with acceptable errors for the conceptual design phase.

A study on the influence of aeroelastic analysis on the configuration of transport airplanes obtained by a multi-disciplinary optimization procedure was carried out. For this purpose, two multi-objective optimization tasks were performed, with the main goal of minimizing the direct operational cost and maximizing the efficiency index for a medium-range wide-body aircraft, one without and the other with aeroelastic constraints. An MDO framework was integrated with the NeoCASS package for aeroelastic analysis. Thus, an aeroelastic constraint was implemented in which the maximum operating Mach number of the aircraft was scanned to find a flutter speed and an altitude at which the phenomenon occurs. If this flutter speed and altitude were inside the flight envelope of the aircraft, the individual was considered infeasible. The comparison of the optimization runs performed showed that the inclusion of flutter constraints in the optimization of the aircraft design has limited the wing aspect ratio, leading to poorer aerodynamic performance and, consequently, poorer optimization results. The comparison of aircraft with higher *EI* found in the two optimizations shows a 10% decrease in *EI* and a 5.25% increase in DOC, while for aircraft with lower DOC there was a 20.9% decrease in *EI* and a 5.92% increase in DOC. In the second case, the constraint completely changed the characteristics of the aircraft by reducing the range and increasing the number of passengers. The inclusion of aeroelastic constraints in conceptual design restrains the performance improvement and therefore significantly alters the optimal designs obtained. Moreover, it was found that these trends cannot be generalized for each aircraft project, since the occurrence of the flutter phenomenon is quite characteristic for each aircraft, responding to small changes in wing geometry, engine parameters, or aerodynamic forces. Therefore, the incorporation of a fast and accurate aeroelastic analysis at the beginning of the conceptual design phase is of utmost importance to increase the confidence of the optimizations.

Acknowledgments

Part of the computations used in the present work was carried out with hardware and software purchased with the support of the Brazilian federal agency Financiadora de Estudos e Projetos (FINEP) through the project CAPTAER II.

References

[1] W. F. Ballhaus Jr. and J. L. Steger, "Implicit Approximate Factorization Schemes for the Low-frequency Transonic Equation," NASA, TM X-73082, Washington, D. C., 1975.

[2] M. Niță and D. Scholz, "Estimating the Oswald Factor from Basic Aircraft Geometrical Parameters," in *German Aerospace Congress 2012*, Berlin, 2012.

[3] R. Bisplinghoff, H. Ashley and R. Halfma, Aeroelasticity, Cambridge, MA: Addison-Wesley, 1955.

[4] E. Dowell, J. Edwards and T. Strgana, "Nonlinear aeroelasticity.," *Journal of Aircraft,* p. 857–874, 2003.

[5] A. J. Eaton, C. Howcroft, E. Coetzee, S. Neild, M. Lowenberg and J. Cooper, "Numerical Continuation of Limit Cycle Oscillations and Bifurcations in High-Aspect-Ratio Wings," *Aerospace,* vol. 5, July 2018.

[6] B. Stanford and P. Beran, "Direct flutter and limit cycle computations of highly flexible wings for efficient analysis and optimization," *Journal of Fluids and Structures,* vol. 36, pp. 111-123, August 2012.

[7] Wikipedia, The Free Encyclopedia, "Boeing 787 Dreamliner," Wikipedia, 2018. [Online]. Available: https://en.wikipedia.org/wiki/Boeing_787_Dreamliner. [Accessed 2018].

[8] Wikipedia, The Free Encyclopedia, "Airbus A350 XWB," Wikipedia, 2018. [Online]. Available: Airbus A350 XWB. [Accessed 2018].

[9] F. George, "Flying The A350: Airbus's Most Technologically Advanced Airliner," Aviation Week, 2015.

[10] Embraer, "Embraer 195 Airport Planning Manual," Embraer, São José dos Campos, 2015.

[11] Embraer, "E-Jets E2 Airport Planning Manual," Embraer, São José dos Campos, 2018.

[12] GE Aviation, "CF34-10E - GE Aviation," October 2018. [Online]. Available: https://www.geaviation.com/bga/engines/cf34-engine. [Accessed October 2018].

[13] Wikipedia, the Free Encyclopedia, "Embraer E-Jet E2 family," Wikipedia, October 2018. [Online]. Available: https://en.wikipedia.org/wiki/Embraer_E-Jet_E2_family. [Accessed October 2018].

[14] Jane's, "Jane's Aero Engines," IHS Markit, December 2017. [Online]. Available: https://janes.ihs.com/.

[15] J. M. Grasmeyer, P. A. Naghshineh-Pour, B. G. Tetrault, R. T. Haftka, R. K. Kapania, W. H. Mason and J. A. Schetz, "Multidisciplinary Design Optimization," Virginia Polytechnic Institute and State University, Blacksburg, 1998.

[16] P. Dees and M. Stowell, "SAE World Aviation Congress & Exposition," in *737-800 Winglet Integration*, 2001.

[17] J. Fregnani, B. Mattos and J. Hernandes, "Multidisciplinary and Multi-Objective Optimization Considering Aircraft Program Cost and Airline Network," *Journal of Air Transportation,* pp. 27-41, January 2021.

[18] MIT Global Airline Industry Program, "Airline Data Project," 2018. [Online]. Available: http://web.mit.edu/airlinedata/www/Aircraft&Related.html. [Accessed 2018].

[19] F. Gern, A. Naghshineh-Pour, E. Sulaeman, R. Kapania and R. Haftka, "Flexible Wing Model for Structural Sizing and Multidisciplinary Design Optimization of a Strut-Braced Wing," in *41st AIAA Structures, Structural Dynamics and Materials Meeting*, Atlanta, 2000.

[20] M. Bhatia, R. K. Kapania, M. v. Hoek and R. T. Haftka, "Structural Design of a Truss Braced Wing: Potential and Challenges," in *Proceedings of the 50th AIAA/ASME/ASCE/AHS/ASC Structures, Structural Dynamics, and Materials Conference*, Palm Springs, CA, 2009.

[21] B. Grossman, R. Kapania, W. Mason and J. Schetz, "Multidisciplinary Design Investigation of Truss-braced Wing Aircraft:Phase 4," Virginia Polytechnic Institute, NAG-1-2217, Blacksburg, 2000.

[22] T. H. Megson, Aircraft Structures, 3rd ed., Oxford: Butterworth-Heinemann, 1999.

[23] P. L. Videiro, "Otimização Aeroestrutural na Fase de Projeto de Aeronave," Instituto Tecnológico de Aeronáutica, Trabalho de Graduação, São José dos Campos, 2012.

[24] E. Torenbeek, Synthesis of Subsonic Airplane Design, Delft: Delft University Press, 1986.

[25] É. Roux, "Modèle de Masse de Voilure,," 2006. [Online]. Available: http://elodieroux.com/ReportFiles/ModelesVoilureVersionPublique.pdf. [Accessed February 2022].

[26] G. Guruswamy and C. Byun, "Fluid-structure Interaction using Navier-Stokes Flow Equations Coupled with Shell Finite Element Structures," in *23rd AIAA Fluid Dynamics, Plasmadynamics, and Lasers Conference*, Orlando, 1993.

[27] V. Harrand, J. Lucker, J. Siegel, V. Parthasarathy, G. Vijayan and P. Dionne, "Application of a multidisciplinary computing environment (MDICE) for loosely coupled fluid–structural analysis," in *7th AIAA/USAF/NASA/ISSMO Symposium on Multidisciplinary Analysis and Optimization*, St. Louis, 1998.

[28] M. Sadeghi, S. Yang, F. Liu and H. Tsai, "Parallel computation of wing flutter with a coupled Navier–Stokes/CSD method," in *41st AIAA Aerospace Sciences Meeting and Exhibit*, Reno, 2003.

[29] R. Bird, W. Stewart and .. Lightfoot, Transport Phenomena, New York: Wiley&Sons, 2007.

[30] H. Versteeg and W. Malalasekra, An introduction to computational fluid dynamics, New Delhi: Pearson India, 2010.

[31] Ansys, Inc., "Ansys Fluent User Guide," Ansys, Inc., 2015.

[32] P. L. Roe, "Approximate Riemann solvers, parameter vectors and difference schemes," *Journal of Computational Physics*, pp. 357-372, 1981.

[33] M. S. Liou and C. J. Steffen Jr., "A new flux splitting scheme," *Journal of Computational Physics*, pp. 23-39, 1993.

[34] P. Hartwitch and . S. Agrawal, "Method for perturbing multiblock patched grids in aeroelastic and design optimization applications," in *13th AIAA Computational Fluid Dynamics Conference*, Snowmass Village, 1997.

[35] M. R. Barber and D. Selegan, "KC-135 Winglet Program Review," NASA CP-2211, Edwards, California, 1982.

[36] B. Almojuela, "The Development of Boeing's 367-80 or charging Into the Jet Age Armed with Only a Slide Rule and Spline," in *Pacific Northwest AIAA Technical Symposium*, Seattle, 2009.

[37] M. C.-Y. Niu, Airframe Structural Design: Practical Design Information and Data on Aircraft Structures, 2nd ed., Adaso/Adastra Engineering Center, 2011, p. 600.

[38] M. D. Sensmeier and J. A. Samaresh, "A Study of Vehicle Structural Layouts in Post-WWII Aircraft," in *45th AIAA/ASME/ASCE/AHS/ASC Structures, Structural Dynamics & Materials Conference*, Palm Springs, 2004.

[39] A. T. Loyd, Boeing 707 & AWACS, in detail and scale., Shrewsbury: Airlift Publishing, 1987.

[40] A. L. Bolsunovsky, N. P. Buzoverya, O. V. Karas and S. I. Skomorokhov, "An Experience in Aerodynamic Design of Transport Aircraft," in *28th International Congress of Aeronautical Sciences*, Brisbane, 2012.

[41] E. N. Tinoco, "CFD codes and applications at Boeing," *Sadhana*, pp. 141-163, 1991.

[42] T. L. Holst, "Transonic Flow Computations Using Nonlinear Potential Methods," *Progress in Aerospace Sciences*, pp. 1-61, 2000.

[43] C. Fletcher, Computational Techniques for Fluid Dynamics 2: Specific Techniques for Different Flow Categories, vol. 2, Springer, 2003.

[44] H. Goetz and D. Nixon, "Nonisentropic Potential Formulation for Transonic Flows," *AIAA Journal*, vol. 22, pp. 770-776, June 1984.

[45] B. S. Mattos, "Numericher Entwurf von transonischen Flügeln und Trageflügelprofilen unter Anwendung des AF2-Algorithmus zur Lösung de vollständigeb Potentialgleichung," Institut für Aerodynamik und Gasdynamik der Universität Stuttgart, Sttutgart, 1995.

[46] B. Mohammadi, "Fluid dynamics computation with NSC2KE: a user-guide: release 1.0," INRIA, Rocquencourt, 1994.

[47] B. Mattos and S. Wagner, "Numerical design of transonic wings in curvilinear coordinates," in *12th AIAA Applied Aerodynamics Conference*, Colorado Springs, 1994.

[48] ANSYS, Inc., "Ansys Fluent Theory Guide Release 15," 2013. [Online]. Available: http://www.pmt.usp.br/ACADEMIC/martoran/NotasModelosGrad/ANSYS%20Fluent%20Theory%20Guide%2015.pdf. [Accessed 2017].

[49] B. S. Mattos, J. A. Fregnani and P. C. Magalhães, Conceptual Design of Green Transport Airplanes, Sharjah, UAE: Bentham Books, 2018.

[50] B. S. Mattos, P. J. Komatsu and J. T. Tomita, "Optimal wingtip device design for transport airplane," *Aircraft Engineering and Aerospace Technology*, vol. 90, pp. 743-763, 2018.

[51] Wikipedia, The Free Encyclopedia, "List of Algorithms," Wikipedia, The Free Encyclopedia, February 2022. [Online]. Available: https://en.wikipedia.org/wiki/List_of_algorithms#Statistics. [Accessed February 2022].

[52] D. Kireev, F. Ros, P. Bernard, J. Chrétien and N. Rozhkova, "Non-supervised Neural Networks: A New Classification Tool to Process Large Databases," in *Computer-Assisted Lead Finding and Optimization: Current Tools for Medicinal Chemistry*, Wiley Online Library, Zurich, 1997, pp. 253-264.

[53] K. Frenken and A. Nuvolari, "Entropy Statistics as a Framework to Analyse Technological Evolution," in *Applied Evolutionary Economics and Complex Systems,*, J. F. &. W. Hölzl, Ed., Edward Elgar Publishing, 2004.

[54] R. Lipmann, "An Introduction to Computing with Neural Nets," *IEEE ASSP Magazine*, vol. 4, pp. 4-22, 1987.

[55] W. S. McCulloch and W. Pitts, "A Logical Calculus of the Ideas Immanent in Nervous Activity," *The Bulletin of Mathematical Biophysics*, vol. 5, pp. 115-133, 1043.

[56] F. Rosenblatt, "he Perceptron: A Probabilistic Model for Information Storage and Organization in the Brain," *Psychological Review*, pp. 386-408, 1958.

[57] M. Minsky and P. Seymour, "Perceptrons," MIT Press, Cambridge, 1969.

[58] J. B. Pollack, "No Harm Intended: A Review of the Book entitled Perceptrons: An Introduction to Computational Geometry," *Journal of Mathematical Psychology*, pp. 358-356, 1989.

[59] D. E. Rumelhart, G. E. Hinton and R. J. Willians, "Learning Representations by Back-propagating Errors," *Cognitive Modeling*, vol. 1, 2002.

[60] T. Kohonen, "An Introduction to Neural Computing," *Neural Network*, vol. 1, pp. 3-16, 1988.

[61] Mathworks, "feedforwardnet," Mathworks, 2019. [Online]. Available: https://www.mathworks.com/help/deeplearning/ref/feedforwardnet.html. [Accessed May 2020].

[62] K. Maladkar, "6 Types of Artificial Neural Networks Currently Being Used in Machine Learning," 2018. [Online]. Available: https://analyticsindiamag.com/6-types-of-artificial-neural-networks-currently-being-used-in-todays-technology/. [Accessed May 2019].

[63] Mathworks, Inc., "Convolutional Neural Network," Mahtworks, Inc., 2020. [Online]. Available: https://www.mathworks.com/solutions/deep-learning/convolutional-neural-network.html. [Accessed 2020].

[64] Mathworks, Inc., "Perceptron," Mathworks, Inc., February 2022. [Online]. Available: https://www.mathworks.com/help/deeplearning/ref/perceptron.html. [Accessed February 2022].

[65] P. Potočnik, "Neural Network Course - Laboratory of Synergetics, Faculty of Mechanical Engineering, University of Ljubljana," 2022. [Online]. Available: https://web.fs.uni-lj.si/lasin/en/pedagoski-proces/nevronske-mreze/. [Accessed February 2022].

[66] Mathworks, Inc., "newrb - Radial Basis Function," Mathworks, Inc., February 2022. [Online]. Available: https://www.mathworks.com/help/deeplearning/ref/newrb.html?searchHighlight=newrb&s_tid=srchtitle_newrb_1. [Accessed February 2022].

[67] FlightAware, "Flight JFK to Narita," Flight Aware, May 2020. [Online]. Available: https://pt.flightaware.com/. [Accessed May 2020].

[68] Flight Aware, "Flight GRU-FRA," Flight Aware, May 2020. [Online]. Available: https://pt.flightaware.com/. [Accessed May 2020].

[69] A. R. Cruz, M. C. Murça, B. S. Mattos and J. T. Fregnani, "Identification of Actual Mission Profiles and their Impact on Integrated Aircraft-Network Optimization," in *AIAA Aviation Forum*, Virtual Event, 2021.

[70] Wikipedia, The Free Encyclopedia, "DBSCAN," Wikipedia, The Free Encyclopedia, 2022. [Online]. Available: https://en.wikipedia.org/wiki/DBSCAN. [Accessed 2022].

[71] J. Sun, S. Ellerbroek and J. M. Hoekstra, "Flight Extraction and Phase Identification for Large Automatic Dependent Surveillance–Broadcast Datasets," *Journal of Aerospace Information Systems,* pp. 566-572, October 2017.

[72] L. A. Zadeh, "Fuzzy Sets," *Information and Control,* pp. 338-353, June 1965.

[73] E. Sun and J. Hoekstra, "Modeling aircraft performance parameters with," in *12th USA/Europe Air Traffic Management Research and Development*, Seattle, 2017.

[74] J. Sun, J. Ellerbroek and J. Hoekstra, "Aircraft initial mass estimation using Bayesian inference method," *Transportation Research Part C: Emerging Technologies,* pp. 59-73, May 2018.

[75] O. M. Silva, " Modelo de desempenho bada e estimativa de massa de aeronave com aplicação em tráfego aéreo," Instituto Tecnológico de Aeronáutica, Undergraduate Thesis, São José dos Campos, 2019.

[76] Eurocontrol, "User Manual for the Base of Aircraft Data (BADA) Revision 3.7," March 2009. [Online]. Available: https://www.eurocontrol.int/sites/default/files/library/003_BADA_3_7_User_manual.pdf. [Accessed February 2022].

[77] K. Gurney, "Neural networks for perceptual processing:from simulation tools to theories," *Philosophical Transactions of the Royal Society B,* pp. 339-353, 8 January 2007.

[78] S. J. Russel and P. Norvig, Artificial Intelligence, A Modern Approach, New Jersey: Prentice-Hall, 2010.

[79] K. Hornick, M. Stinchcombe and H. White, "Multilayer Feedforward Networks are Universal Approximators," in *Neural Networks,* Pergamon Press, 1989, pp. 359-366.

[80] Mathworks, "fitnet," Mathworks, 2020. [Online]. Available: https://www.mathworks.com/help/deeplearning/ref/fitnet.html. [Accessed 2019].

[81] T. P. Vogl, J. K. Mangis, A. K. Rigler, W. T. Zink and D. L. Alkon, "Accelerating the convergence of the backpropagation method," *Biological Cybernetics,* vol. 59, p. 257–263, 1988.

[82] D. Marquardt, "An Algorithm for Least-Squares Estimation of Nonlinear Parameters," *SIAM Journal on Applied Mathematics,* p. 431–441, June 1963.

[83] M. T. Hagan and M. Menhaj, "Training feed-forward networks with the Marquardt algorithm," *IEEE Transactions on Neural Networks,* vol. 5, p. 989–993, 1999.

[84] Mathworks, Inc., "trainlm," Mathworks, Inc., 2020. [Online]. Available: https://www.mathworks.com/help/deeplearning/ref/trainlm.html. [Accessed 2020].

[85] P. V. Camarotti, " Estudo de drivers de mercado, metodologia e desenvolvimento de ferramenta semi-automática para elaboração de projeções de mercado de aviação de linha," ITA, Undergraduate Thesis, São José dos Campos, 2014.

[86] IEA, "Oil Information: Overview, IEA," 2020. [Online]. Available: https://www.iea.org/reports/oil-information-overview. [Accessed 2020].

[87] EIA - U. S. Energy Administration Information, "Petroleum & Other Liquids Weekly Stocks," 2020. [Online]. Available: https://www.eia.gov/dnav/pet/hist/LeafHandler.ashx?n=PET&s=WCESTUS1&f=W. [Accessed 2020].

[88] EIA - U.S. Energy Information Administration, "Crude Oil Production, OPEC Total, Annual," 2020. [Online]. Available: https://www.eia.gov/opendata/qb.php?sdid=STEO.COPR_OPEC.A. [Accessed 2020].

[89] EIA - U.S. Energy Information Administration, "Non-OPEC + OPEC non-Crude Production, Annual," 2020. [Online]. Available: https://www.eia.gov/opendata/qb.php?sdid=STEO.PAPR_NONOPEC_I_OPECNC.A. [Accessed 2020].

[90] Macrotrends, "WTI Crude Oil Prices," 2020. [Online]. Available: https://www.macrotrends.net/2516/wti-crude-oil-prices-all-years. [Accessed 2020].

[91] L. Jenkinson, P. Simpkin and D. Rhodes, "Civil Jet Aircraft design - Boeing Aircraft," Butterworth-Heinemann, 2001. [Online]. Available: https://booksite.elsevier.com/9780340741528/appendices/data-a/table-3/table.htm. [Accessed June 2021].

[92] M. Gumes e L. D. Andrade Pereira, “Utilização de Redes Neurais para Estimação de Coeficienets Aerodinâmicos e Derivadas de Estabilidade,” Undegraduation thesis, Instituto tecnológico de Aeronáutica,, São José dos Campos, 2019.

[93] B. Singh, "A Medium-Fidelity Method for Rapid Maximum Lift Estimation," Delft University, Delft, 2017.

[94] S. Gudmundsson, "Maximum Lift Coefficient," Elsevier, 2018. [Online]. Available: https://www.sciencedirect.com/topics/engineering/maximum-lift-coefficient. [Accessed September 1029].

[95] Mathworks, Inc., "gamultiobj," Mathworks, Inc, 2018. [Online]. Available: https://www.mathworks.com/help/gads/gamultiobj.html. [Accessed August 2019].

[96] M. Drela, "XFOIL - Subsonic Airfoil Development System," October 2018. [Online]. Available: http://web.mit.edu/drela/Public/web/xfoil/. [Accessed October 2018].

[97] N. Secco and B. Mattos, "Artificial neural networks to predict aerodynamic coefficients of transport airplanes," *Aircraft Engineering and Aerospace Technology,* pp. 211-230, March 2017.

[98] M. Niţă and D. Scholz, "Estimating the Oswald Factor from Basic Aircraft Geometrical Parameters," in *German Aerospace Congress 2012*, Berlin, 2012.

[99] C. Panda and Venkatasubramani, "Aeroelasticity- In General and Flutter Phenomenon," in *Second International Conference on Emerging Trends in Engineering and Technology, ICETET-09,* Nagpur, Maharashtra, 2009.

[100] P. Dees and M. Stowell, "737–800 Winglet Integration," in *World Aviation Congress & Exposition*, Seattle, 2001.

[101] M. Bradley and K. Droney, "Ultra Green Aircraft research: Phase I Final Report," National Aeronautics and Space Administration, NASA CR2011-216847, Huntington Beach, CA, 2011.

[102] W. Zhinqiang and C. Cesnik, "Geometrically Nonlinear Aeroelastic Scaling for Very," in *54th AIAA/ASME/ASCE/AHS/ASC Structures, Structural Dynamics, and Materials Conference* , Boston, Massachusetts, 2013.

[103] M. Kehoe, "A Historical Overview of Flight Flutter Testing," NASA, Dryden Flight Research Center, 1985.

[104] B. Baldwin, "The Efficiency Of Wing Technology On Crossover Narrowbody Jets," Aviation Week Network, 21 October 2021. [Online]. Available: https://aviationweek.com/special-topics/crossover-narrowbody-jets/efficiency-wing-technology-crossover-narrowbody-jets. [Accessed October 2021].

[105] M. Opgenoord, M. Drela and K. Willcox, "Influence of Transonic Flutter on the Conceptual Design of Next-generation Transport Aircraft," in *AIAA/ASCE/AHS/ASC Structures, Structural Dynamics, and Materials Conference*, Kissimmee, 2018.

[106] E. Jonsson, C. Riso, C. Lupp, C. Cesnik, J. Martins and B. Epureanu, "Flutter and Post-flutter Constraints in Aircraft Design Optimization," *Progress in Aerospace Sciences,* vol. 109, May 2019.

[107] M. Berci and F. Torrigiani, "Multifidelity Sensitivity Study of Subsonic Wing Flutter for Hybrid Approaches in Aircraft Multidisciplinary Design and Optimisation," *Aerospace,* vol. 7, November 2020.

[108] L. Cavagna, S. Ricci and L. Travaglini, "Aeroelastic Analysis and Optimization at Conceptual Design Level Using NeoCASS Suite," in *52nd AIAA/ASME/ASCE/AHS/ASC Structures, Structural Dynamics and Materials Conference*, Denver, 2011.

[109] J. A. Fregnani, B. Mattos and J. A. Hernandes, "Multidisciplinary and Multi-Objective Optimization Considering Aircraft Program Cost and Airline Network," *Journal of Air Transportation,* pp. 21-41, January 2021.

[110] V. Loureiro and B. S. Mattos, "Powerplant as Design Variable for Multi-disciplinary Design Optimization of Transport Airplane," in *27th AIA Applied Aerodynamics Conference*, San Antonio, 2009.

[111] D. A. Muraro and B. S. Mattos, "Estimation of Noise of Installed Turbofan Engines," in *3th DCTA-DLR Workshop on Data Analysis and Flight Control*, São José dos Campos, 2009.

[112] A. Bosquê, B. Mattos and R. Girardi, "Entropy Statistics Applied to Airplane Evolution," in *11th Brazilian Congress of Thermal Sciences and Engineering -- ENCIT 2006*, Curitiba, 2006.

[113] A. Rios, J. Fregnani, B. Mattos and M. Condé, "Identification of the Actual Mission Profiles and Their Impact on the Integrated Aircraft and Airline Network Optimization," 2021.

[114] MathWorks, "Genetic Algorithm," MathWorks, December 2017. [Online]. Available: https://www.mathworks.com/discovery/genetic-algorithm.html. [Accessed December 2017].

[115] R. C. Quintero, "TECHNO-ECONOMIC AND ENVIRONMENTAL Techno-Economic and Environment Risk Assessment of Innovative Propulsion Systems for Short-Range Civil Aircraft," Cranfield, 2009.

[116] J. A. Fregnani, B. S. Mattos and J. A. Hernandes, "Airline Network-Airplane Integrated Optimization Considering Manufacturer's Program Cost," in *ICAS 2020*, Shangai, 2021.

[117] G. W. van Bondergraven, "Commercial Aircraft DOC Methods," in *AIAA/AHS/ASEE Aircraft Design Systems and Operations Conference*, Dayton, 1990.

[118] Air Transport Association of America, "Standard Method of Estimating Comparative Operating Direct Costs of Turbine Powered Transport Airplanes," Air Transport Association of America, Washington, D. C., 1967.

[119] "Jet Fuel Price Monitor," IATA, May 2021. [Online]. Available: https://www.iata.org/en/publications/economics/fuel-monitor/. [Accessed May 2021].

[120] P. Montarnal, "Presto-Cabin A Preliminary Sizing TRool for Passenger Aircraft Cabins," Hamburg University of Applied Sciences, Hamburg, 2010.

[121] Wikipedia, The Free Encyclopedia, "Rolls-Royce RB211," Wikipedia, The Free Encyclopedia, 2021. [Online]. Available: https://en.wikipedia.org/wiki/Rolls-Royce_RB211. [Accessed May 2021].

[122] European Union Aviation Safety Agency, "Type-Certificate Data Sheet for Rolls&Royce for RB211-535 Series Engine," EASA, Cologne, 2020.

[123] Boeing Commercial Airplanes, "Boeing Resources," 2021. [Online]. Available: https://www.boeing.com/resources/boeingdotcom/company/about_bca/startup/pdf/historical/757_passenger.pdf. [Accessed May 2021].

[124] Boeing Commercial Airplanes, "Boeing 757 Airplane Characteristics for Airport Planning," Boeing, Seattle, 2002.

[125] Boeing Commercial, "777-200/300 Airplane Characteristics for Airport Planning," Boeing Co., Seattle, 1998.

[126] J. G. Barmby, H. J. Cunningham and I. E. Garrick, "Study of Effects cited on," NACA, Washington, 1951.